Title

Evolution of z~2 Galaxies on Resolved Scales Using CANDELS/3D-HST Imaging and Emission Line Spectroscopy From the MOSDEF Survey

Author

Fetherolf, Tara

Publication Date

2020

UNIVERSITY OF CALIFORNIA
RIVERSIDE

Evolution of $z \sim 2$ Galaxies on Resolved Scales Using CANDELS/3D-HST Imaging and Emission Line Spectroscopy From the MOSDEF Survey

A Dissertation submitted in partial satisfaction
of the requirements for the degree of

Doctor of Philosophy

in

Physics

by

Tara D. Fetherolf

September 2020

Dissertation Committee:

Dr. Naveen A. Reddy, Chairperson
Dr. George D. Becker
Dr. Brian Siana
Dr. Bahram Mobasher

The Dissertation of Tara D. Fetherolf is approved:

Committee Chairperson

University of California, Riverside

Acknowledgments

First, I would like to thank my husband, family, and friends who have been understanding and supportive throughout my journey to achieve this important milestone. Completing this work would not have been possible without the guidance and support of my research advisor, Naveen Reddy. I appreciate that I have been able to be part of the MOSDEF team and thank my collaborators for their contributions that have made this work possible and their valuable feedback. Thank you to all of the astronomy faculty at UCR—especially my committee members: George Becker, Brian Siana, and Bahram Mobasher—and all of the astronomy graduate students for building an amazing and supportive community. Finally, I would like to thank Stephen Kane and everyone in the Planet Research Laboratory group for supporting my additional interest in exoplanet research, which I will continue to pursue during my postdoc.

I acknowledge financial support from UCR through the Chancellor's Distinguished Fellowship, Graduate Research Mentorship Program Fellowship, and Dissertation Year Program Fellowship. The MOSDEF team acknowledges support from an NSF AAG collaborative grant (AST-1312780, 1312547, 1312764, and 1313171) and grant AR-13907 from the Space Telescope Science Institute.

The observations for this work utilized the following facilities: the ACS and WFC3 imaging cameras on the *Hubble Space Telescope* (*HST*), the MOSFIRE multi-object spectrograph on the Keck I telescope at the W. M. Keck Observatory, and IRAC imaging from *Spitzer*. To complete the analyses in this work, I acknowledge the following open source Python packages: Astropy (Astropy Collaboration et al. 2013, 2018), Matplotlib (Hunter

2007), NumPy (Oliphant 2007), SciPy (Oliphant 2007), specline (Shivaei et al. 2018), and adaptive Voronoi binning code (Cappellari & Copin 2003).

This work is based on observations taken by the CANDELS Multi-Cycle Treasury Program and the 3D-HST Treasury Program (GO 12177 and 12328) with the NASA/ESA *HST*, which is operated by the Association of Universities for Research in Astronomy, Inc., under NASA contract NAS5-26555. Some of the data presented herein were obtained at the W. M. Keck Observatory, which is operated as a scientific partnership among the California Institute of Technology, the University of California, and the National Aeronautics and Space Administration. The Observatory was made possible by the generous financial support of the W. M. Keck Foundation. The MOSDEF team and I recognize and acknowledge the very significant cultural role and reverence that the summit of Maunakea has always had within the indigenous Hawaiian community. We are most fortunate to have the opportunity to conduct observations from this mountain.

This dissertation contains drafts of articles that have been accepted (Chapter 2), submitted (Chapter 3), or will be submitted (Chapter 4) for publication by Oxford University Press in the Monthly Notices of the Royal Astronomical Society written by me and my collaborators on the MOSDEF team: Tara Fetherolf, Naveen A. Reddy, Alice E. Shapley, Mariska Kriek, Brian Siana, Alison L. Coil, Bahram Mobasher, William R. Freeman, Ryan L. Sanders, Sedona H. Price, Irene Shivaei, Mojegan Azadi, Francesca M. Fornasini, Laura de Groot, Gene C.K. Leung, and Tom O. Zick.

ABSTRACT OF THE DISSERTATION

Evolution of $z \sim 2$ Galaxies on Resolved Scales Using CANDELS/3D-HST Imaging and Emission Line Spectroscopy From the MOSDEF Survey

by

Tara D. Fetherolf

Doctor of Philosophy, Graduate Program in Physics
University of California, Riverside, September 2020
Dr. Naveen A. Reddy, Chairperson

Studying the resolved structure of high-redshift galaxies can give insight into the evolution of galaxy properties. The resolved distribution of stars and the interstellar dust obscuring their light can be probed using stellar population maps, which are derived from resolved images of galaxies. I use emission line spectroscopy from the MOSFIRE Deep Evolution Field (MOSDEF) survey combined with CANDELS/3D-HST high-resolution imaging to create resolved stellar population and reddening maps for ∼300 star-forming MOSDEF galaxies at $z \sim 2$. In the construction of my maps, I incorporate a more precise methodology that negates systematic biases towards dustier measurements compared to previous methodologies.

The focus of my dissertation is to understand how star formation may influence complex geometries of dust within galaxies. Uniform coverage of dust in front of the stars has typically been assumed, but some studies have revealed that instead a two-component dust model is more appropriate with higher obscuration caused by dust towards star-forming regions. To avoid assumptions made when correcting for spectroscopic slit-loss,

I directly compare the MOSDEF spectroscopic measurements to the photometric measurements within the area encompassed by the spectroscopic slit placement. My results indicate that the relative optical-to-ultraviolet star-formation rate ratio is higher in the centers of large galaxies compared to their outskirts, which may imply that highly star-forming galaxies have patchier dust distributions.

Previously, resolved galaxy structure has been quantified based on their light distributions from the resolved imaging. I devise a new and more general metric, called "patchiness," that is sensitive to any deviations from the average and use it to directly probe the distribution of physical properties in galaxies. This patchiness metric is used alongside two previously established measures in order to interpret the complex geometries of the dust and stars within galaxies. My results reveal how the dustiness within galaxies changes as galaxies grow, transitioning from mostly uniform coverage to the two-component model with regions of higher obscuration. Overall, my dissertation work addresses how star-forming galaxies evolve on both resolved and unresolved scales, particularly at high redshifts when star-formation activity was at its highest.

Contents

List of Figures

Chapter 1

Introduction

One of the major goals of cosmology is to understand how galaxies assemble their stellar mass over cosmic time. Measuring the rate that stars are forming is one of the best measures of galaxy growth. Based on the star-formation rate (SFR) density versus cosmic time (see Figure 1.1), galaxies were very active and building their stellar mass very quickly at redshift $z \sim 2$ (see Madau & Dickinson 2014). Therefore, studying galaxies at cosmic noon is a critical step in understanding their evolution. Active galaxies produce a lot of dust, which complicates extracting their intrinsic SFRs. Starlight that is obscured by dust will get scattered and absorbed by the dust grains, then reemitted in the infrared. Figure 1.2 shows how a dust-free spectral energy distribution (SED) of a stellar population (blue curve) changes when the obscuring effects of dust are included (red curve).

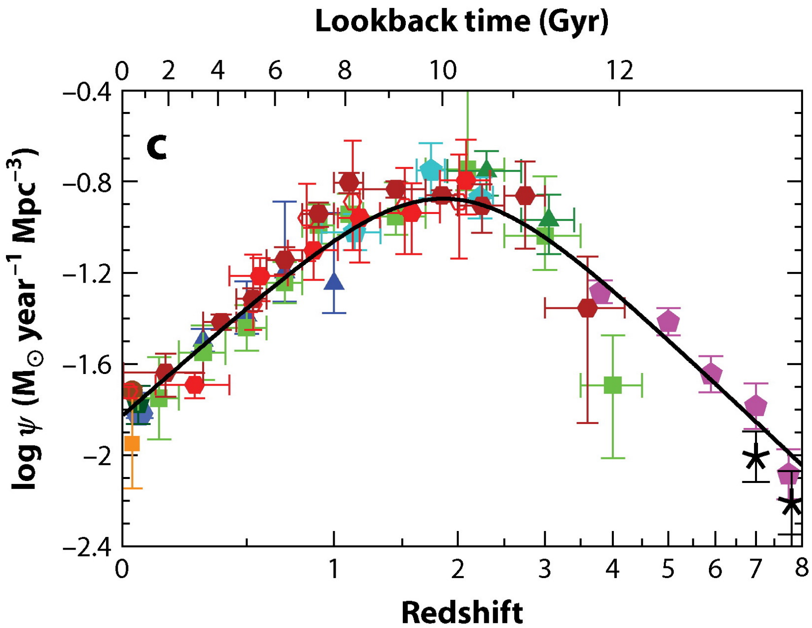

Figure 1.1: The SFR density versus cosmic time from Madau & Dickinson (2014). SFRs are measured from both the far UV and infrared. Each color and shape of the points represents a different study (see Table 1 in Madau & Dickinson 2014).

1.1 The Influence of Dust

A method that is used to correct for the effects of dust is to measure the observed slope of the SED in the ultraviolet (UV, 1250–2500 Å; Calzetti et al. 1994; Meurer et al. 1999) and then make an assumption about how much the light is attenuated as a function of wavelength (e.g., Cardelli et al. 1989; Fitzpatrick & Massa 1990; Calzetti et al. 2000; Gordon et al. 2003; Reddy et al. 2015; Shivaei et al. 2020). However, Figure 1.3 shows how the degree that the UV slope changes not only depends on the amount of dust, but also the distribution of dust. Dust that is in front of the stars will have a greater influence on the UV slope compared to if the same amount of dust were well-mixed with the stars. An alternative, but more direct dust correction method is to measure the ratio of nebular recombination lines

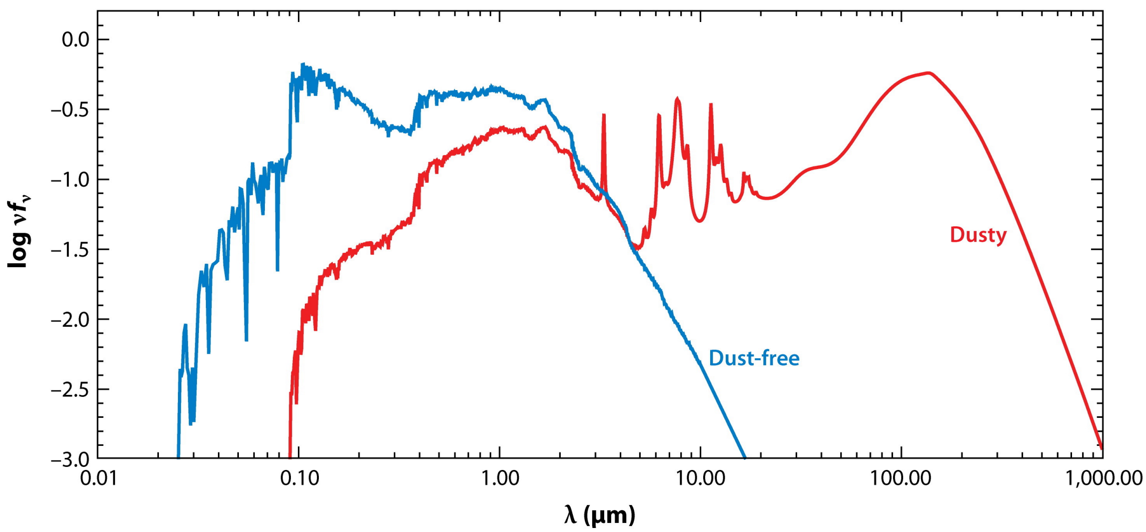

Figure 1.2: Example SED of a stellar population synthesis model from Conroy (2013). The blue curve shows the SED of the composite stellar population before the contribution of dust has been included. The red curve shows how the same composite stellar population SED changes when the effects of dust are incorporated.

compared to the intrinsic ratio expected from typical interstellar medium (ISM) conditions (Osterbrock 1989), known as the Balmer decrement (Hα/Hβ). This method is sensitive to the highest mass stars, which are likely to die before their birth cloud disperses.

Some studies have found that these two measures of dust attenuation are approximately equal or differ by a constant factor in high-redshift galaxies (e.g., Meurer et al. 1999; Calzetti et al. 2000; Kashino et al. 2013; Price et al. 2014; Tacchella et al. 2018), such that the dust distribution could be simply approximated by a mostly uniform or even clumpy foreground screen (Calzetti et al. 1994). However, several authors have alternatively argued that dust opacities are higher towards the most massive stars that have recently formed such that nebular dust attenuation is higher than that of the stellar continuum and the amount of extra attenuation varies with SFR (Yoshikawa et al. 2010; Kreckel et al. 2013;

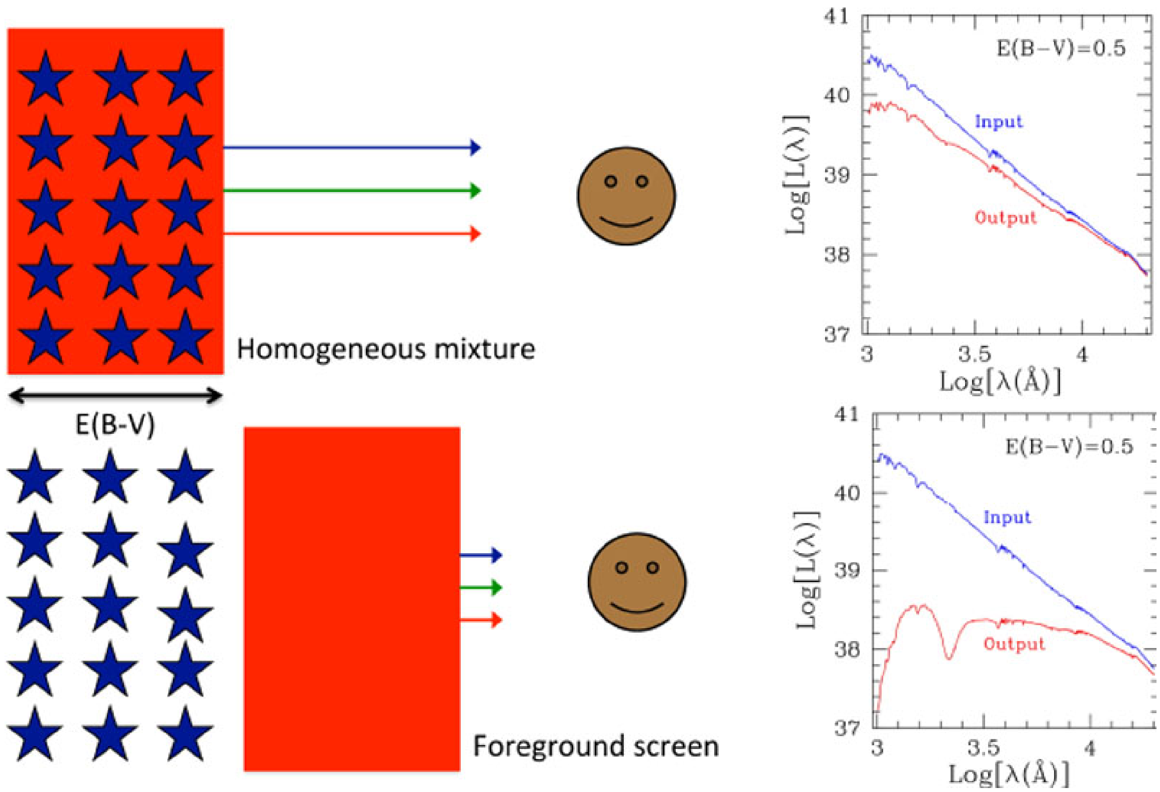

Figure 1.3: A demonstration of how changing the dust geometry relative to the stars influences the shape of the observed SED from Calzetti (2013). Illustrations for the distribution of the stars (blue stars) and dust (red regions) are shown on the left. The intrinsic and dust-attenuated SEDs are represented by the blue and red curves on the right, respectively. *Top:* When the dust (red region) is well-mixed with the stars (blue stars), there is little effect on the observed SED. *Bottom:* If the same amount of dust is instead entirely in front of the stars, then there is a greater effect on the shape of the observed SED.

Reddy et al. 2015), specific SFR (Wild et al. 2011; Price et al. 2014; Boquien et al. 2015; Reddy et al. 2015; Hemmati et al. 2015), SFR surface density (Boquien et al. 2015), and metallicity (Shivaei et al. 2020).

1.2 Resolved Structure of High-redshift Galaxies

The work presented in the chapters that follow address the following questions regarding the resolved structure and evolution of high-redshift galaxies.

1. How does the geometry of stars and dust affect globally measured physical properties of galaxies?

2. What causes nebular dust attenuation to be higher than that of the stellar continuum and how does this relate to potential differences between Hα and UV SFR indicators?

3. How does the geometry of stars and dust change as galaxies evolve?

4. How efficiently does dust mix throughout the ISM?

These questions are not easily addressed using observations from the ground due to the atmosphere blocking regions of the electromagnetic spectrum, emitting thermal radiation, and blurring resolved structures of galaxies by turbulent motions at high altitudes. Observations of high-redshift galaxies are also subject to the effects of cosmological dimming (see Barden et al. 2008) and high-redshift galaxies are at an earlier stage in their evolution such that they are physically smaller in size (e.g., Toft et al. 2007; Trujillo et al. 2007; van der Wel et al. 2014; Scott et al. 2017; van de Sande et al. 2018). While the effects of galaxy growth and redshift cannot be avoided, the effects of the atmosphere can be negated by putting a telescope in space.

High-redshift galaxies do not have classical "Hubble Sequence" structures such as disks, bulges, or bars (Hubble 1926; de Vaucouleurs 1959). Instead, most high-redshift galaxies appear irregular in shape (e.g., Griffiths et al. 1994; Dickinson 2000; van den Bergh 2002; Papovich et al. 2005; Shapley 2011; Conselice 2014) such that their structures are typically quantified through their radial profiles (e.g., Nelson et al. 2013, 2016; Hemmati et al. 2015; Tacchella et al. 2018), the properties of clump-like structures (e.g., Guo et al.

2012, 2015, 2018; Wuyts et al. 2012, 2013; Hemmati et al. 2015), or numerically using morphology metrics (e.g., CAS, Gini, M20, ICD; Conselice 2003; Abraham et al. 2003; Lotz et al. 2004; Papovich et al. 2005). Previous resolved studies of $z \sim 2$ galaxies either lacked spectroscopic redshifts (only photometric redshifts were available) that are necessary for removing degeneracies in the SED fitting or they did not have sufficiently large sample sizes that are representative of the population of galaxies being studied (Wuyts et al. 2012; Guo et al. 2012, 2015, 2018; Tadaki et al. 2014; Boada et al. 2015; Jung et al. 2017; Tacchella et al. 2018).

1.3 Dissertation Outline

The work presented in this dissertation avoids the effects of the atmosphere and obtains spectroscopic redshifts for a large sample of high-redshift galaxies by pairing high-resolution imaging from the *Hubble Space Telescope* (*HST*) with emission line spectroscopy from the MOSFIRE multi-object spectrograph (McLean et al. 2010, 2012) on the Keck I telescope. The Cosmic Assembly Near-infrared Deep Extragalactic Legacy Survey (CANDELS; Grogin et al. 2011; Koekemoer et al. 2011) obtained *HST* imaging in the optical to near-infrared in 8 broadband filters covering 5 well-studied extragalactic fields at a $0\farcs06\,\mathrm{pixel}^{-1}$ resolution, which corresponds to $\sim 0.5\,\mathrm{kpc\,pixel}^{-1}$ at $z \sim 2$. The CANDELS imaging has also been complemented by spatially resolved emission line maps from the 3D-HST survey (Brammer et al. 2012; Momcheva et al. 2016) and a photometric catalog containing ancillary data from other ground- and space-based observations covering the same extragalactic fields (Skelton et al. 2014). The MOSFIRE Deep Evolution Field (MOSDEF; Kriek et al.

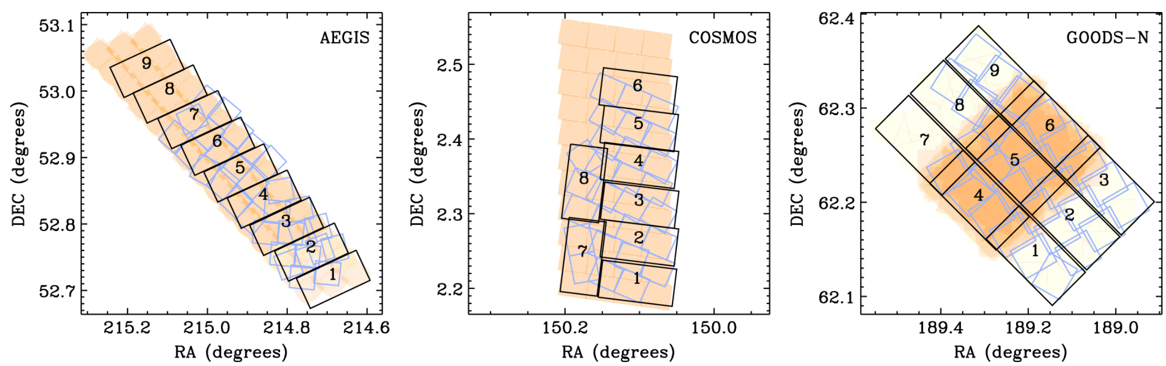

Figure 1.4: Orientations of the overlapping observations from CANDELS, 3D-HST, and MOSDEF for 3 of the extragalactic fields from Kriek et al. (2015). The orange shaded regions represent the CANDLES resolved imaging, the 3D-HST grism masks are highlighted by the light blue boxes, and the MOSFIRE multi-object spectrograph masks are numbered in the black rectangles.

2015) survey further adds to the legacy of CANDELS by observing ∼1500 star-forming galaxies and AGN at $1.4 \leq z \leq 3.8$ in the same regions of the sky (see Figure 1.4). This work primarily utilizes the spectroscopic redshifts for the resolved SED fitting and the Hα and Hβ emission line measurements to measure the nebular dust attenuation towards sites of recent star-formation and the SFR that is sensitive to these regions. Targets for the MOSDEF survey were selected in three redshift bins ($z \sim 1.5$, $z \sim 2.3$, and $z \sim 3.4$) in order to optimally observe several emission lines in the atmospheric transmission windows. Data from the $z \sim 3.4$ bin are not used in this dissertation because Hα is not typically detected and galaxies are harder to resolve with sufficient S/N in the CANDELS imaging at these redshifts.

This dissertation is split into three main segments and organized as follows. Chapter 2 broadly focuses on the methodology for creating resolved stellar population and robust reddening maps, which includes an improved binning technique that reduces systematic biases observed in the reddening derived from resolved SED fitting compared to previous methods. The effects of potential aperture biases on different probes of dust reddening and SFRs are investigated in Chapter 3. A new morphology metric, called "patchiness," is defined in Chapter 4 and used to quantify the resolved dust reddening maps and infer the structural evolution of the dust distribution in the ISM of star-forming galaxies at $z \sim 2$. Finally, the main conclusions of the dissertation and potential future work are summarized in Chapter 5.

Chapter 2

Paper I: An Improved Voronoi Binning Technique on Spatially Resolved Stellar Populations at $z \sim 2$[1]

Abstract We use a sample of 350 star-forming galaxies at $1.25 < z < 2.66$ from the MOSFIRE Deep Evolution Field survey to demonstrate an improved Voronoi binning technique that we use to study the properties of resolved stellar populations in $z \sim 2$ galaxies. Stellar population and dust maps are constructed from the high-resolution CANDELS/3D-HST

[1]This chapter contains a draft of an article that has been accepted for publication by Oxford University Press in the Monthly Notices of the Royal Astronomical Society written by Tara Fetherolf, Naveen A. Reddy, Alice E. Shapley, Mariska Kriek, Brian Siana, Alison L. Coil, Bahram Mobasher, William R. Freeman, Ryan L. Sanders, Sedona H. Price, Irene Shivaei, Mojegan Azadi, Laura de Groot, Gene C.K. Leung, and Tom O. Zick due for publication in 2020.

multi-band imaging. Rather than constructing the layout of resolved elements (i.e., Voronoi bins) from the S/N distribution of the H_{160}-band alone, we introduce a modified Voronoi binning method that additionally incorporates the S/N distribution of several resolved filters. The SED-derived resolved $E(B-V)_{\rm stars}$, stellar population ages, SFRs, and stellar masses that are inferred from the Voronoi bins constructed from multiple filters are generally consistent with the properties inferred from the integrated photometry within the uncertainties, with the exception of the inferred $E(B-V)_{\rm stars}$ from our $z \sim 1.5$ sample due to their UV slopes being unconstrained by the resolved photometry. The results from our multi-filter Voronoi binning technique are compared to those derived from a "traditional" single-filter Voronoi binning approach. We find that single-filter binning produces inferred $E(B-V)_{\rm stars}$ that are systematically redder by 0.02 mag on average, but could differ by up to 0.20 mag, and could be attributed to poorly constrained resolved photometry covering the UV slope. Overall, we advocate that our methodology produces more reliable SED-derived parameters due to the best-fit resolved SEDs being better constrained at all resolved wavelengths—particularly those covering the UV slope.

2.1 Introduction

Quantifying the distributions of stars, gas, and dust is an important step in understanding the formation and evolution of galaxies. For example, the locations of massive stars and their rates of formation can help address the assembly history of galaxies (e.g., Wuyts et al. 2012; Hemmati et al. 2014; Boada et al. 2015), the rate and efficiency with which gas is converted into stars (e.g., Lang et al. 2014; Jung et al. 2017; Tacchella et al.

2018), and a galaxy's merger history (e.g., Conselice 2003; Lotz et al. 2004, 2008; Cibinel et al. 2015). Studying the structure of galaxies at $z \sim 2$ is particularly relevant as cosmic star formation reaches its peak at this epoch, and galaxies were rapidly assembling their stellar mass (see Madau & Dickinson 2014).

Galactic structure can either be assessed qualitatively by eye (e.g., Hubble's Tuning Fork; Hubble 1926) or quantitatively using parametric (e.g., Sérsic profile; Sérsic 1963) and non-parametric (e.g., CAS, Gini, M_{20}; Conselice 2003; Abraham et al. 2003; Lotz et al. 2004) metrics that measure the distribution of light. However, morphological classification schemes can potentially break down at higher redshifts. Compared to typical local galaxies, high-redshift galaxies are at an earlier stage in their evolution and appear clumpier and irregular in shape (e.g., Griffiths et al. 1994; Dickinson 2000; Papovich et al. 2005; Shapley 2011; Conselice 2014). Furthermore, since galaxies at $z \sim 2$ are in the process of building the bulk of their stellar mass (Madau & Dickinson 2014), they are typically physically smaller in size due to their lower stellar masses (e.g., Toft et al. 2007; Trujillo et al. 2007; van der Wel et al. 2014; Scott et al. 2017; van de Sande et al. 2018) compared to their low-redshift counterparts. Observationally, these distant galaxies are also subject to the effects of cosmological dimming (see Barden et al. 2008), and the highest spatial resolution achievable with space-based facilities like the *Hubble Space Telescope* (*HST*) cover physically larger regions (few-kpc per resolution element) compared to that of lower redshift galaxies that are observed with the same instruments (sub-kpc per resolution element). Consequently, careful analyses are required when quantifying the morphology of galaxies (i.e., the distribution of stars, gas, and dust within galaxies) across a range of redshifts in an effort to infer how the structure of galaxies changes with cosmic time.

Several studies have explored resolved stellar populations in $z \gtrsim 2$ galaxies by fitting the observed pixel-to-pixel spectral energy distribution (SED) with stellar population synthesis models (Guo et al. 2012, 2015, 2018; Boada et al. 2015; Jung et al. 2017; Tacchella et al. 2018). While the highest resolution (for a given pixel scale) is obtained by fitting for the resolved SEDs within individual pixels, the signal-to-noise (S/N) within individual pixels may be too low such that the derived resolved stellar population properties may be unreliable. Furthermore, the signal may be correlated between adjacent pixels given that the spatial resolution of the instrument (i.e., the point-spread function, or PSF) is larger than the size of the individual pixels. To compensate for these effects, several studies have implemented an adaptive Voronoi binning technique (Cappellari & Copin 2003) that groups pixels based on their S/N distribution such that low S/N pixels are grouped together into larger bins (e.g., Wuyts et al. 2012, 2013, 2014; Genzel et al. 2013; Tadaki et al. 2014; Lang et al. 2014; Chan et al. 2016). Typically, Voronoi bins are constructed using the S/N in a single filter, namely the H_{160} band. However, for redder galaxies, such construction can lead to Voronoi bins with low S/N in bluer bands, resulting in poor constrains on the resolved stellar populations. If the S/N is not sufficiently high in at least 5 resolved filters (see Torrey et al. 2015), then the resulting best-fit SEDs may not produce reliable stellar population inferred quantities for these bins.

In this work, we introduce an improved Voronoi binning method that groups pixels based on reaching a desired S/N threshold in multiple resolved filters. Our method improves the reliability of the derived stellar population parameters—albeit by sacrificing some spatial resolution—compared to the traditional single-filter approach for constructing Voronoi bins. In this paper, we apply our methodology to a sample of 350 star-forming galaxies drawn from the MOSFIRE Deep Evolution Field survey (MOSDEF; Kriek et al. 2015). The MOSDEF survey obtained rest-frame optical spectra for ∼1500 star-forming galaxies and AGNs at $1.4 \lesssim z \lesssim 3.8$ that were drawn from the Cosmic Assembly Near-IR Deep Extragalactic Legacy Survey (CANDELS; Grogin et al. 2011; Koekemoer et al. 2011) and overlap with observations from the 3D-HST survey (Brammer et al. 2012; Skelton et al. 2014). Our study of the resolved stellar populations in high-redshift galaxies improves upon previous work. Previous resolved studies of $z \gtrsim 2$ galaxies either lacked accurate spectroscopic redshifts necessary to mitigate degeneracies in SED-fitting (typically only photometric redshifts were used) or had samples with fewer than 100 galaxies (Wuyts et al. 2012; Guo et al. 2012, 2015, 2018; Tadaki et al. 2014; Boada et al. 2015; Jung et al. 2017; Tacchella et al. 2018). The statistically large sample of galaxies with robust spectroscopic redshifts and emission line measurements in the MOSDEF dataset, on the other hand, enables an unprecedented view into the resolved stellar populations of $z \sim 2$ galaxies. In this paper, we focus on the methodology of our Voronoi binning technique and demonstrate its utility. Detailed analysis of the resolved stellar population parameters obtained based on the new methodology will be presented in a follow-up paper.

The data, sample selection, and integrated stellar population synthesis modeling is presented in Section 2.2. In Section 2.3, our modified multi-filter Voronoi binning technique for building stellar population and reddening maps is outlined. The resolved SEDs and SED-derived properties are compared to unresolved global quantities derived from the 3D-HST photometry in Section 2.4 and our modified multi-filter Voronoi binning method is compared to the traditional single-filter Voronoi binning technique. Finally, the key points are summarized and we provide recommendations for resolved SED fitting analyses in Section 2.5.

All line wavelength measurements are given in vacuum and magnitudes are expressed in the AB system (Oke & Gunn 1983) throughout this paper. A cosmology with $H_0 = 70\,\mathrm{km\,s^{-1}\,Mpc^{-1}}$, $\Omega_\Lambda = 0.7$, and $\Omega_m = 0.3$ is assumed.

2.2 Data, Sample Selection, and Integrated SED-derived Properties

In this section, we present our observations, sample selection, and stellar population parameters inferred from fitting unresolved (integrated, or global) photometry. In Section 2.2.1, we discuss the high-resolution, multi-wavelength CANDELS/3D-HST photometry from which we construct the resolved stellar population and reddening maps. The MOSDEF survey is described in Section 2.2.2, including the spectroscopic redshift measurements. The sample drawn from the parent MOSDEF survey is discussed in Section 2.2.3. Finally, in Section 2.2.4, we list the assumptions used to obtain global and resolved stellar population parameters.

2.2.1 CANDELS/3D-HST Photometry

We use multi-wavelength broadband photometry from 0.3 to 8.0 μm in the five CANDELS (Grogin et al. 2011; Koekemoer et al. 2011) extragalactic fields: AEGIS, COSMOS, GOODS-N, GOODS-S, and UDS. CANDELS *HST* imaging covers $\sim$900 arcmin^2 and is 90% complete at $H_{160} \sim 25$ mag. We make use of the publicly-available[2] imaging and photometric catalogs that were processed and compiled by the 3D-HST grism survey team (Brammer et al. 2012; Skelton et al. 2014; Momcheva et al. 2016). The *HST* images were drizzled to a $0\farcs06$ pixel^{-1} scale and PSF-convolved to the same $0\farcs18$ spatial resolution as the H_{160} data.

2.2.2 MOSDEF Spectroscopy

Targets for the MOSDEF survey were selected from the five CANDELS extragalactic fields using the 3D-HST photometric and spectroscopic catalogs in three redshift bins ($1.37 < z < 1.70$, $2.09 < z < 2.61$, and $2.95 < z < 3.80$) such that the following strong rest-frame optical emission lines fall in near-IR windows of atmospheric transmission: [OII]λ3727, 3730, Hβ, [OIII]$\lambda\lambda$4960, 5008, Hα, [NII]$\lambda\lambda$6550, 6585, and [SII]λ6718, 6733. The targets were selected to an H_{160}-band limit of 24.0, 24.5, and 25.0 mag for the $z = 1.37-1.70$, $2.09-2.61$, and $2.95-3.80$ redshift bins (hereafter referred to as the $z \sim 1.5$, $z \sim 2.3$, and $z \sim 3$ samples), respectively, corresponding to a stellar mass limit of $\sim 10^9$ M$_\odot$ for all three redshift bins. The galaxy identifications used throughout this paper refer to the 3D-HST v4 photometric catalog.

[2] https://3dhst.research.yale.edu/

The 4.5 year MOSDEF survey obtained rest-frame optical spectra for ∼1500 star-forming and AGN galaxies using the MOSFIRE multi-object spectrograph (McLean et al. 2010, 2012) in the Y, J, H, and K bands ($R = 3400$, 3000, 3650, and 3600 using $0\farcs7$ slit widths) on the 10 m Keck I telescope. Every slit mask also included at least one slit star, which is used for the absolute flux calibration and corrections for slit loss. Line fluxes are measured by fitting a linear function to the continuum and a Gaussian function to each emission line. For the [OII]$\lambda\lambda3727, 3730$ doublet and Hα+[NII]$\lambda\lambda6550, 6585$ lines, a double and triple Gaussian is fit the the lines, respectively. The stellar population model that best fits the observed 3D-HST photometry (Section 2.2.4) is used to correct Hα and Hβ line fluxes for underlying Balmer absorption. Flux errors are obtained from the 68th-percentile width of the distribution of line fluxes that have been remeasured from the 1D spectra that have been perturbed by their error spectra 1000 times. Finally, the spectroscopic redshift is measured from the observed wavelength of the highest signal-to-noise (S/N) emission line, which is typically Hα or [OIII]$\lambda5008$. Refer to Kriek et al. (2015) and Reddy et al. (2015) for additional details on the MOSDEF survey, including the observing strategy, data reduction, and line flux measurements.

In this study, the redshift of each galaxy (and its resolved components) is fixed to the measured MOSDEF spectroscopic redshift in order to constrain the stellar population parameters derived from the SED fitting.

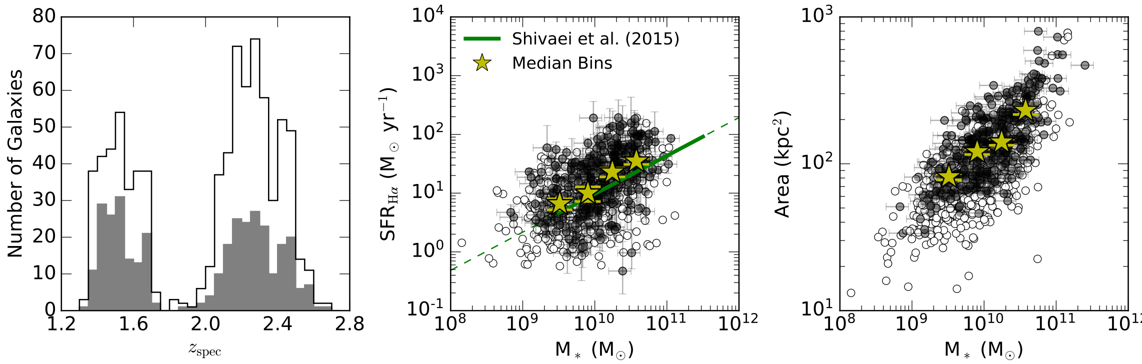

Figure 2.1: *Left:* Spectroscopic redshift distribution of galaxies in our sample covering two redshift bins: $1.24 < z < 1.74$ and $1.84 < z < 2.66$. The white histogram shows the initial sample distribution (830 galaxies). The gray histogram denotes our primary sample (350 galaxies) that results after S/N restrictions are applied in the Voronoi binning procedure (see Section 2.3.2). *Middle:* Hα SFR versus stellar mass, i.e. the star-forming main sequence. Hα emission is corrected for dust using the Balmer decrement and assuming the Cardelli et al. (1989) extinction curve. All Hα SFRs are calculated assuming a Chabrier (2003) IMF and 20% Solar metallicity (see Section 2.2.4). The solid green line (extended by the dashed line for visual clarity) is the best linear fit to the SFR–M_* relation based on the first two years of data from the MOSDEF survey (Shivaei et al. 2015b). The empty and filled circles show the galaxies in the initial (830) and final samples (350), respectively. The yellow stars are the medians of the individual points of the 350 galaxies in our sample, equally divided into four bins of stellar mass. *Right:* The size–M_* relation for our initial and selected samples, with the same symbol coloring as the middle panel. The area is measured from the detected 3D-HST segmentation map region for each galaxy. Our final sample selection is marginally biased against compact, low-mass galaxies due to the S/N requirements imposed by the Voronoi binning procedure (see Section 2.3.2).

2.2.3 Sample Selection

Our sample is derived from the MOSDEF parent sample in the $z \sim 1.5$ and $z \sim 2.3$ redshift bins. First, only galaxies with robust spectroscopic redshifts that have been measured using at least two emission features with a S/N > 2 are selected. AGNs are removed based on their identification through their X-ray luminosities, optical emission lines ($\log([\rm NII]/H\alpha) > -0.3$), and/or mid-IR luminosities (Coil et al. 2015; Azadi et al. 2017, 2018; Leung et al. 2019). This initial sample contains 830 star-forming galaxies at

$1.24 < z < 2.66$, including 74 galaxies that were serendipitously detected outside of the targeted MOSDEF redshift bins. Additional constraints to the S/N and resolution of the photometry are applied when performing adaptive Voronoi binning (see Section 2.3.2), which brings our sample to 350 star-forming galaxies at redshifts $1.25 < z < 2.66$.

The spectroscopic redshift distribution, SFR–M_* relation, and size–M_* relation are shown in Figure 2.1 for the galaxies in our initial (white histogram; empty circles) and final (gray histogram; filled circles) samples. Also shown is the median SFR, size, and stellar mass of our sample divided into four equally sized bins (yellow stars). The SFR bins are on average 0.16 dex above the main sequence relation defined in Shivaei et al. (2015b), which is within the intrinsic scatter of the relation. Our final selected sample is marginally biased against low-mass and low-SFR galaxies, primarily due to the tendency of such galaxies to be compact and/or faint. It is difficult to spatially resolve compact galaxies into several components and faint galaxies do not have sufficient S/N for measuring reliable spatially resolved fluxes across several filters. Therefore, these factors cause low-mass and low-SFR galaxies to be excluded from our sample during the Voronoi binning procedure (see Section 2.3.2).

2.2.4 Spatially-Unresolved SED Fitting

The stellar populations are modeled on both resolved (see Section 2.3.4) and unresolved scales for galaxies in our sample to obtain SED-derived $E(B-V)_{\rm stars}$, stellar population ages, SFRs, and stellar masses. Here we describe the SED fits to the integrated galaxy light, as measured from the 3D-HST photometric catalogs. A χ^2 minimization technique is used to select the Bruzual & Charlot (2003) stellar population model that best fits the observed photometry (see Reddy et al. 2012). First, the photometry is corrected for the strongest emission lines measured in the MOSDEF spectroscopy, including Hα, Hβ, [OIII]$\lambda\lambda 4960, 5008$, and the [OII]$\lambda 3728$ doublet. In the SED modeling, we assume a Chabrier (2003) initial mass function (IMF), constant star-formation histories (SFHs), and allow the ages to range between 50 Myr and the age of the Universe at the redshift of each galaxy.[3] Reddening in the range $0.0 \leq E(B-V)_{\rm stars} \leq 0.4$ is considered while assuming an SMC extinction curve (Fitzpatrick & Massa 1990; Gordon et al. 2003) and sub-solar metallicity ($0.2\,Z_{\odot}$).[4]

Typical SED parameter errors are derived using a subset of 50 randomly selected galaxies from our sample that span the SED fitting parameter space in $E(B-V)_{\rm stars}$, stellar population age, SFR, and stellar mass in both redshift bins. Only 50 galaxies are selected for the error analysis in the interest of limiting computation time, but the range of SED parameters probed by these 50 galaxies is similar to that of the larger sample. The measured fluxes are perturbed 100 times by their flux errors and refit. The width of the parameter space of the 68 (of 100) models with the lowest χ^2 relative to the observed photometry are assumed to represent the errors in the SED parameters. The typical SED parameter error is then estimated as the average of the errors from all galaxies in the subsample. The typical random SED parameter errors derived from the SEDs fit to the perturbed 3D-HST

[3] Reddy et al. (2012) found that both exponentially rising and constant SFHs best reproduce SFRs for $z \sim 2$ galaxies when stellar population ages are limited to being older than the typical dynamical timescale (50 Myr). Stellar population ages that are derived using constant SFHs are typically $\sim$30% younger than those assumed with exponentially rising SFHs (Reddy et al. 2012).

[4] Recent studies have found that SMC-like or steeper attenuation curves paired with sub-Solar metallicities are more appropriate for young, high-redshift galaxies (Reddy et al. 2018a). The Calzetti et al. (2000) attenuation curve paired with Solar metallicities may be more appropriate for massive galaxies, but primarily affects the absolute mass measurements and not their relative order (Reddy et al. 2018a) and, thus, does not significantly change our results.

photometry are as follows: 0.01 in $E(B-V)_{\rm stars}$, 0.20 dex in log stellar population age, 0.05 dex in log SFR, and 0.16 dex in log stellar mass.

2.3 Resolved Stellar Population and Reddening Maps

2.3.1 Resolved Photometry

The resolved stellar population and reddening maps are constructed using *HST*/WFC3 resolved imaging in the F125W, F140W, and F160W filters (hereafter J_{125}, JH_{140}, and H_{160}), and *HST*/ACS resolved imaging in the F435W, F606W, F775W, F814W, and F850LP filters (hereafter B_{435}, V_{606}, i_{775}, I_{814}, and z_{850}). Note that not all of the filters are available for all of the CANDELS fields. The resolved imaging is supplemented with un-resolved *Spitzer*/IRAC photometry at 3.6 μm, 4.5 μm, 5.8 μm, and 8.0 μm, which has been corrected for contamination by neighboring sources using models of the *HST* images that have been PSF-smoothed to the lower resolution IRAC photometry. Pixels associated with the 3D-HST photometry are identified using the Source Extractor (Bertin & Arnouts 1996) segmentation maps provided by the 3D-HST grism survey (Skelton et al. 2014), which are based on a noise-equalized combination of J_{125}+JH_{140}+H_{160}.

RMS error (noise) maps are additionally required to measure flux uncertainties and the pixel-to-pixel S/N, which are obtained using the provided 3D-HST weight maps. While the science images have been spatially smoothed to the resolution of the H_{160} filter by the 3D-HST team, the weight maps are based on the un-convolved imaging. Using the un-convolved and convolved science images, the weights are converted to spatially matched measurement errors as follows. First the weight maps are converted to noise maps using

$N_{\rm orig} = 1/\sqrt{w_{\rm orig}}$, where $w_{\rm orig}$ is the provided weight and $N_{\rm orig}$ is the noise. Then the spatially matched measurement errors are calculated in each pixel by

$$N_{\rm conv} = \left| \frac{S_{\rm conv}}{S_{\rm orig}/N_{\rm orig}} \right|, \tag{2.1}$$

where $S_{\rm orig}$ and $N_{\rm orig}$ are the signal and noise of the original science images and $S_{\rm conv}$ and $N_{\rm conv}$ are the signal and noise of the convolved images. By definition, Equation 2.1 conserves the S/N on a pixel-to-pixel level between the original and convolved images. Total flux errors measured from the convolved noise maps are typically ∼70% larger than the 3D-HST photometric catalog flux errors, but the larger errors do not significantly affect our results.

2.3.2 Adaptive Voronoi Binning

Construction of the resolved stellar population and reddening maps begins with isolating individual galaxies in our sample. Sub-images that are 80×80 pixels in size ($4''.8 \times 4''.8$, or approximately 40×40 kpc at $z \sim 2$) are cut for each galaxy from the CANDELS/3D-HST imaging and its respective spatially matched noise map. The 3D-HST segmentation map is then used to mask any pixels not associated with the galaxy. The median of the pixels that are unassociated with any detected sources is used to apply a local background subtraction to each pixel of the sub-image, although the correction is negligible since the CANDELS images are already background subtracted.

To study resolved stellar populations of galaxies, SED fitting can be performed either on a pixel-by-pixel basis, or on larger "resolved" elements (e.g., Voronoi bins) formed by grouping together adjacent pixels. We argue that the latter procedure is necessary for a proper interpretation of the resolved stellar populations for the following reasons. Generally only the central regions of each galaxy have sufficient S/N for reliable SED fitting on a pixel-by-pixel basis. Moreover, the signal is correlated between neighboring individual pixels due to the spatial resolution indicated by the *HST* PSF and data resampling when constructing the images. Several studies have used the two-dimensional adaptive Voronoi binning technique developed by Cappellari & Copin (2003) to study resolved stellar populations in galaxies (e.g., Wuyts et al. 2012, 2013, 2014; Genzel et al. 2013; Tadaki et al. 2014; Lang et al. 2014; Chan et al. 2016). The Cappellari & Copin (2003) algorithm adaptively bins pixels based on the S/N distribution such that each Voronoi bin has at least the specified target S/N while maintaining a "roundness" threshold. With the exception of Chan et al. (2016), these studies applied Voronoi binning to their samples by requiring a S/N = 10 per Voronoi bin in the H_{160} filter. While this approach boosts the S/N for H_{160} in every resolved element, bluer filters may have lower S/N per pixel depending on the colors of the galaxy. For this reason, Chan et al. (2016) instead applied the same S/N = 10 threshold to the z_{850} filter. We alternatively include the contribution of light from spatially segregated regions that are brighter at shorter wavelengths (e.g., blue star-forming regions compared to red bulge-like features) in each spatially resolved element by modifying the Cappellari & Copin (2003) algorithm (version 3.0.4) to construct the Voronoi bins based on the S/N distribution of multiple filters. Each filter is evaluated and is only used for Voronoi binning if the total S/N in that filter,

$$\left(\frac{S}{N}\right)_{\rm total} = \frac{\sum_{i=1}^{n_{\rm pix}} S_i}{\sqrt{\sum_{i=1}^{n_{\rm pix}} N_i^2}}, \quad (2.2)$$

measured across all pixels associated with the galaxy is more than the user-designated target S/N, where $n_{\rm pix}$ is the number of pixels identified in the segmentation map. We use a target S/N = 5, which is acceptably lower than previous studies due to our multi-filter requirement, but necessary to obtain robust constraints on the stellar population parameters.

The modifications applied to the Cappellari & Copin (2003) algorithm add constraints only while building the Voronoi bins. Unmodified processes include the pixel selection while building candidate bins, the "roundness" threshold of a candidate bin, or the assignment of unsuccessfully binned pixels after the bins have been created. We refer the reader to Cappellari & Copin (2003) for further details on their adaptive Voronoi binning technique. Here we describe how Voronoi bins are constructed given our modifications (refer to Figure 2.2 for a visual outline). The layout of the Voronoi bins is based on the S/N distribution of a primary filter (H_{160} is used, similar to other studies), although the S/N distribution in all applicable filters is considered. A candidate bin begins with the unbinned pixel that has the highest S/N in the primary filter, then neighboring pixels are added to the bin until the specified target S/N is reached in all applicable filters. The modified algorithm also includes designating an optional minimum Voronoi bin size. The smallest Voroni bins are constrained to contain at least 3 pixels (in contrast with typical Voronoi binning schemes that allow single pixels to be Voronoi bins) such that they match the *HST* PSF resolution of 0.″18, translating to the smallest resolution elements having an area of $\sim$0.75 kpc^2. If this binning procedure fails (for example, the entire galaxy has been grouped into a single bin), the process is repeated using one less filter—specifically the filter with the lowest $(S/N)_{\rm total}$ as calculated in Equation 2.2 (note that the primary filter is always

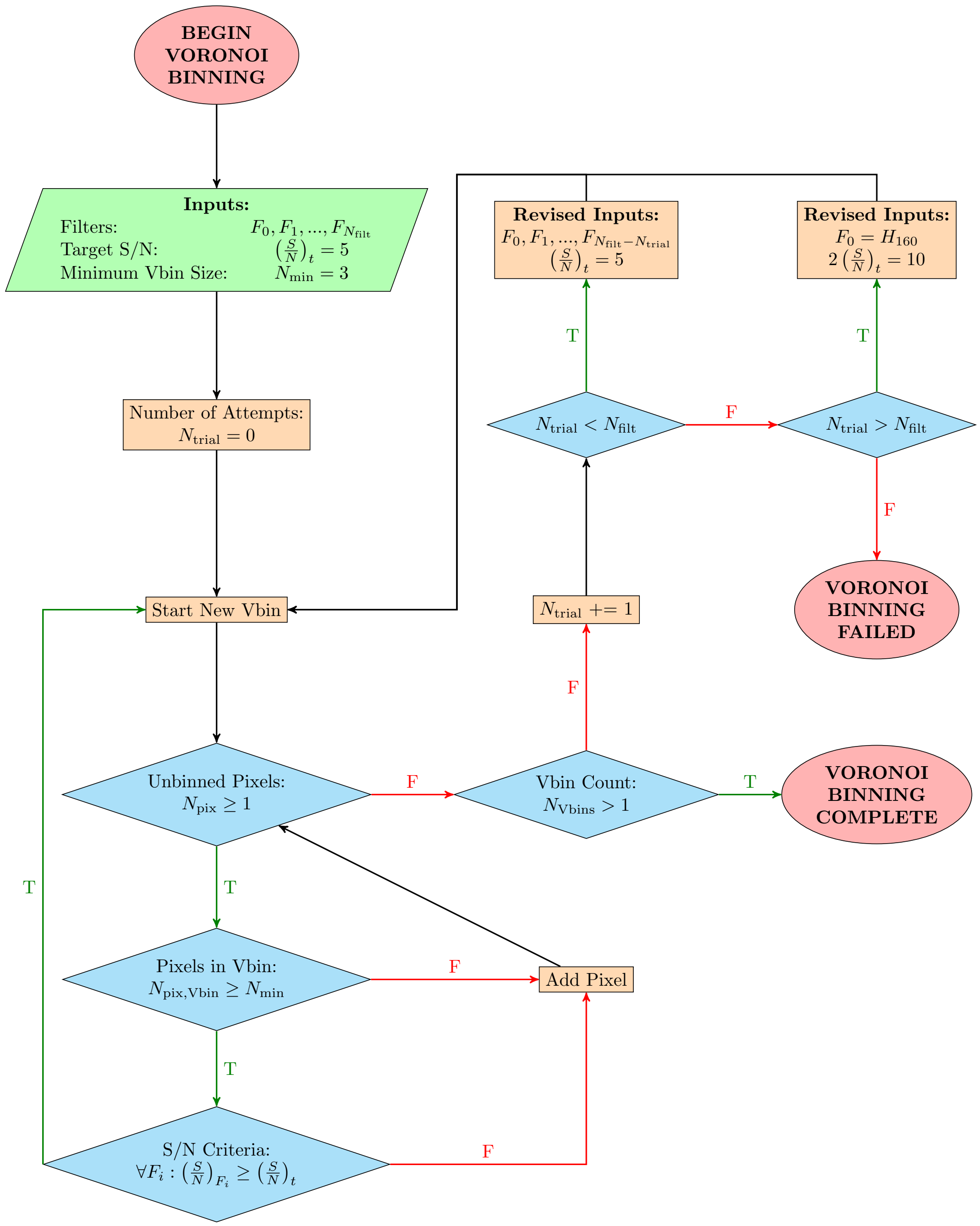

Figure 2.2: Flowchart highlighting the modifications we applied to the Cappellari & Copin (2003) adaptive Voronoi binning algorithm. For this study, the primary filter is $F_0 = H_{160}$, the target signal-to-noise is $(S/N)_t = 5$, and the minimum number of pixels per Voronoi bin is $N_{\rm min} = 3$. $N_{\rm filt}$ is the number of additional filters used in addition to the primary filter, $N_{\rm trial}$ is the number of times adaptive Voronoi binning has been attempted, $N_{\rm pix}$ is the number of unbinned pixels remaining, $N_{\rm pix,Vbin}$ is the number of pixels within the Voroni bin being constructed, and $N_{\rm Vbins}$ is the total number of Voronoi bins after all pixels have been assigned into a Voronoi bin.

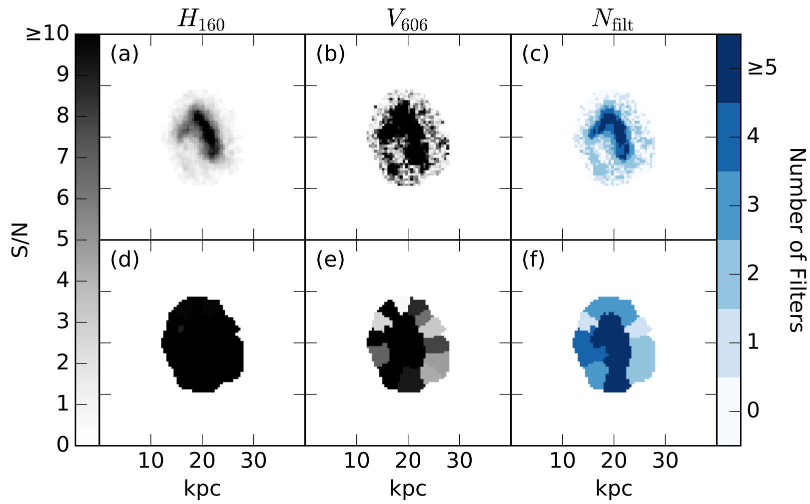

Figure 2.3: The S/N maps before and after applying adaptive Voronoi binning for one of the galaxies in our sample, UDS 21834 ($z = 1.67$). Only the 911 pixels and 41 bins identified by the segmentation map are shown. *Top row*: the pixel-to-pixel S/N distribution in (a) H_{160} and (b) V_{606}. Panel (c) shows for each pixel the number of filters (N_{filt}) that have a S/N $\geq$ 5. *Bottom row*: the Voronoi bin S/N distribution in the (d) H_{160} and (e) V_{606} filters. Panel (f) shows for each Voronoi bin the number of filters that have a S/N $\geq$ 5. The Voronoi bins within the darkest blue region match our criteria of a S/N $\geq$ 5 in $\geq$5 filters, which throughout the text will be referred to simply as the "Voronoi bins." All other lighter blue regions make up the "outskirt" component and will be referred to as such throughout the text.

required). Upon each failed binning attempt, this procedure will repeat iteratively until only the primary filter remains. If all other filters have been rejected, the revised adaptive Voronoi binning algorithm is applied to the primary filter (H_{160}) alone using a S/N that is twice that of the original target S/N (S/N = 10, matching the requirements used by previous studies). However, for this study we require that the bins be defined by multiple filters that span the Balmer and 4000 Å breaks in order to more robustly quantify ages and stellar masses on a bin-by-bin basis. Therefore, any galaxies that failed to be adaptively binned using at least two filters (H_{160} and one additional filter) are removed from our sample.

As an example, Figure 2.3 shows how the S/N distribution for one of the galaxies in our sample (UDS 21834, $z = 1.67$) varies between the H_{160} and V_{606} filters on the pixel-to-pixel level in panels (a) and (b) and across the Voronoi bins in panels (d) and (e). Panel (f) in Figure 2.3 shows the number of filters that have a S/N ≥ 5 in each Voronoi bin. For comparison, panel (c) shows the number of filters that have a S/N ≥ 5 on the pixel-to-pixel level. Torrey et al. (2015) found that applying a simplified set of SED fitting assumptions (i.e., dust-free, restricted ages, and limited metallicities) to a sample of simulated galaxies observed in 5 filters reproduced stellar masses within a factor of two of the known simulated mass. Therefore, reliable best-fit SEDs are expected to be produced from the regions where a S/N ≥ 5 is reached in at least 5 filters, as is represented by the darkest blue color in panels (c) and (f) of Figure 2.3. By comparing the areas covered by the darkest blue color in panels (c) and (f), it can be seen that a larger region of the galaxy can be used for reliable SED fitting when adaptive Voronoi binning is applied with a multi-filter requirement. For this reason, we only consider Voronoi bins that have a S/N ≥ 5 in a minimum of 5 filters for the primary SED fitting. Throughout the text, we refer to the bins with a S/N ≥ 5 in at least 5 filters as the "Voronoi bins." We also ensure that the high S/N filters cover both sides of the Balmer and 4000 Å break region, which further constrains the stellar population age estimates. Bins that are not above the target S/N contain the "remaining" signal and tend to be in the outskirts of the galaxy (light blue bins shown in panel (f) of Figure 2.3). The bins that have less than 5 filters with S/N ≥ 5 are referred to as "outskirt" components of the galaxy. Collectively, the high S/N Voronoi bins combined with the outskirt bins cover exactly the same area defined by the 3D-HST segmentation map. In Section 2.4, the integrated SED and its respective parameters derived from the conservatively selected Voronoi bins are compared to those derived from additionally including the outskirt components. Outskirt bins are only included in our analyses where specifically noted as their SED-derived properties are more uncertain due to the lower S/N in these bins.

Galaxies that have less than 5 Voronoi bins (outskirt bins do not contribute) remaining are removed from our sample, as they are considered unresolved. Galaxies in our sample have 5–151 Voronoi bins (∼16 bins on average), as is shown by the histogram in Figure 2.4. On average, an individual Voronoi bin contains ∼18 pixels (∼4.5 kpc^2) and the median bin size is 6 pixels (1.5 kpc^2). Overall the Voronoi binning procedure reduces the sample size from the 830 star-forming galaxies discussed in Section 2.2.3 to 350 galaxies. As can be seen in Figure 2.1, the Voronoi binning requirements marginally biases our sample against low-mass, low-SFR, and compact galaxies.

2.3.3 Flux Measurements

The counts in the convolved science images and noise maps are converted to flux density, and the AB magnitude and magnitude error are calculated within each Voronoi bin. The minimum magnitude error is set to 0.05 mag, in order to prevent any single photometric point from skewing the SED fit.

To better constrain the stellar masses estimated from the SED fitting, *Spitzer*/IRAC unresolved photometry (normalized to the segmentation map area) is paired with the resolved photometry. We choose to simply normalize the IRAC photometry by the H_{160} flux in each resolved element, rather than adjusting the best-fit resolved SEDs to match the in-

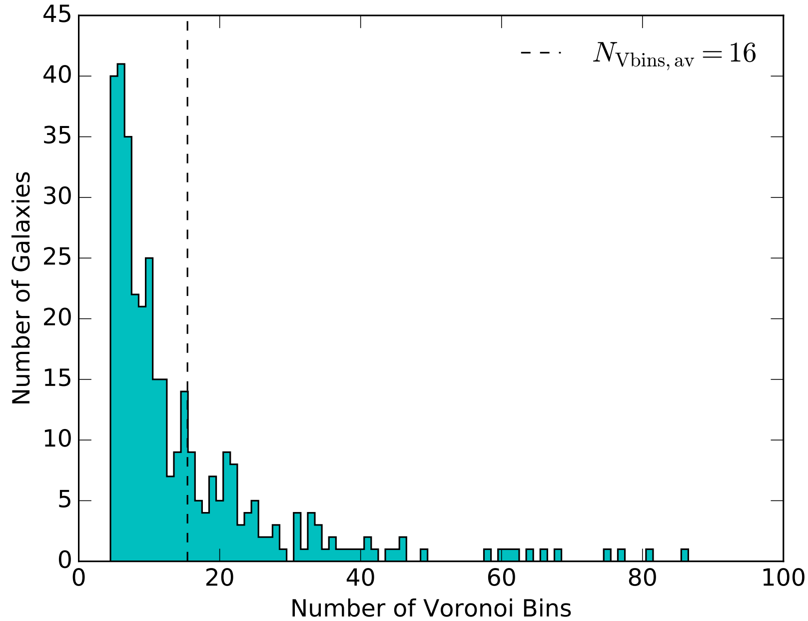

Figure 2.4: Distribution of the number of Voronoi bins within each galaxy in our sample. To be included in our sample, galaxies must have at least 5 Voronoi bins. The black dashed vertical line shows the average number of Voronoi bins per galaxy, $N = 16$. The median Voronoi bin size is 6 pixels and the minimum Voronoi bin size is set to 3 pixels.

tegrated 3D-HST SED as suggested by Wuyts et al. (2012). The IRAC flux in each resolved element, $F_{\rm IRAC,Vbin}$, is estimated by normalizing the total IRAC flux by the H_{160} bin flux. The normalized IRAC flux per Voronoi bin is defined as

$$F_{\rm IRAC,Vbin} = F_{\rm IRAC,tot} \frac{H_{\rm 160,Vbin}}{H_{\rm 160,tot}}, \tag{2.3}$$

where $H_{\rm 160,tot}$ and $F_{\rm IRAC,tot}$ are the 3D-HST H_{160} and IRAC broadband fluxes, and $H_{\rm 160,Vbin}$ is the H_{160} flux measured within the resolved element (Voronoi bin, in our case). In Appendix A, we show that the differences in the best-fit SEDs and SED-derived parameters are typically insignificant when using the more computationally-expensive methodology described by Wuyts et al. (2012). However, the Wuyts et al. (2012) method may be more appropriate when key SED features are not properly constrained by the resolved photometry (e.g., UV slope, Balmer/4000 Å breaks; also see Section 2.4.2).

Using the normalization defined by Equation 2.3 forces the H_{160}–IRAC colors to be constant across the entire galaxy, thus constraining the strength of the Balmer and 4000 Å breaks for the highest redshift galaxies in our sample ($z \gtrsim 2.5$). As the Balmer/4000 Å break is sensitive to stellar population age and attenuation (e.g., Worthey 1994; Shapley et al. 2001), we must be wary of how fixing the H_{160}–IRAC color affects the derived age and reddening maps. In Appendix B, we investigate how variations in the H_{160}–IRAC colors influence the distribution of stellar population ages and reddening inferred through the SED fitting. In general, we find that the redder Voronoi bins remain red (higher $E(B-V)_{\rm stars}$) and the bluer Voronoi bins remain blue (lower $E(B-V)_{\rm stars}$) when their H_{160}–IRAC colors are perturbed, indicating that our constraint on the H_{160}–IRAC colors (i.e., Equation 2.3) does not unduly influence the results concerning the distribution of stellar population ages and attenuation within galaxies.

2.3.4 Resolved SED Fitting

The same model assumptions that were outlined in Section 2.2.4 are also used for the resolved SED fitting. For each galaxy in our sample, two representations of the integrated properties are obtained by fitting a single SED to (a) the multi-wavelength 3D-HST broadband photometry (Skelton et al. 2014, see Section 2.2.4) and (b) the total sum of the flux within all of the valid Voronoi bins (including the total 3D-HST IRAC fluxes). Resolved SED modeling is performed on all of the individual Voronoi bins and outskirt

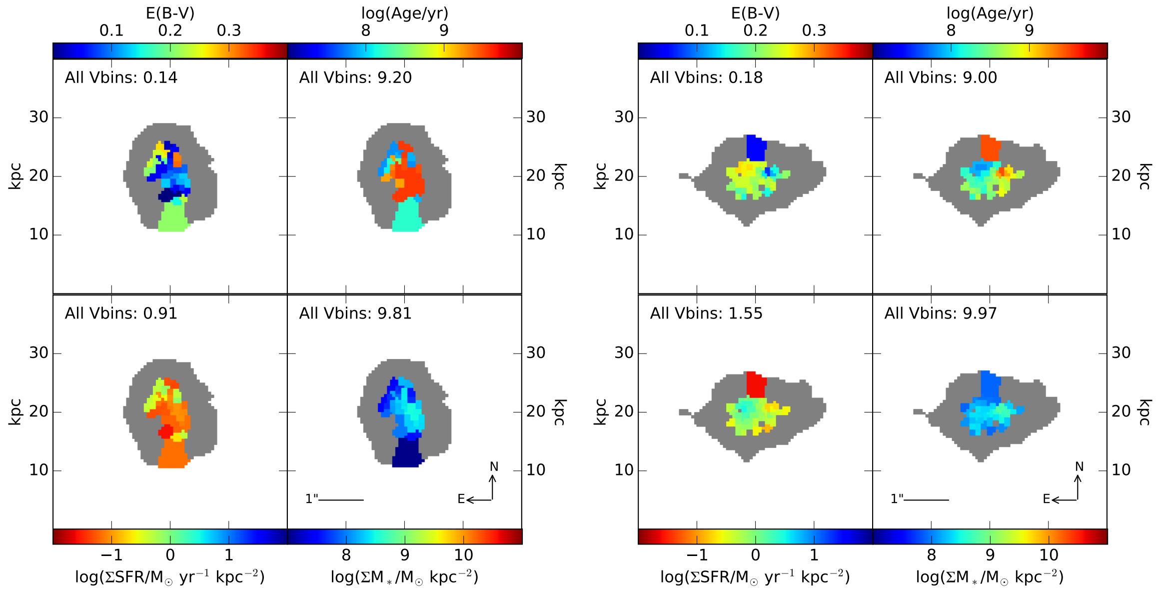

Figure 2.5: Stellar population and reddening maps from resolved SED fitting for UDS 21834 ($z = 1.67$, *left panels*) and COSMOS 3666 ($z = 2.09$, *right panels*), showing the distribution of $E(B-V)_{\rm stars}$ (*top left*), stellar population age (*top right*), SFR (*bottom left*), and stellar mass (*bottom right*). These galaxies both have 41 Voronoi bins with the bins containing an average of 8 and 6 pixels ($\sim$2 kpc^2 and $\sim$1.5 kpc^2), respectively. The gray regions indicate the outskirt component consisting of regions that are included in the segmentation map, but do not fulfill the Voronoi bin criteria (S/N $\geq$ 5 in at least 5 filters) discussed in Section 2.3.2. The listed number in each panel shows the average $E(B-V)_{\rm stars}$ or stellar population age weighted by the Voronoi bin areas or the summed SFR or stellar mass from all of the Voronoi bins.

components. In Section 2.4 we compare the resolved and integrated SED fitting results and demonstrate how using only the high S/N Voronoi bins does not significantly affect the results from the SED fitting (see Section 2.3.2). Figure 2.5 shows the resolved stellar population and reddening maps for UDS 21834 ($z = 1.67$) and COSMOS 3666 ($z = 2.09$) as examples. The average $E(B-V)_{\rm stars}$, average stellar population age, summed SFR, and summed stellar mass derived from the Voronoi bins is listed in the top left corner of each panel in Figure 2.5.

Typical resolved SED parameter errors are derived using the same subset of 50 galaxies as was used to obtain the integrated SED parameter errors (see Section 2.2.4). Only 50 galaxies are selected for the error analysis in the interest of limiting computation time, but the range of SED parameters probed by these 50 galaxies is similar to that of the larger sample. The measured fluxes in each Voronoi bin are perturbed 100 times by their flux errors and refit. The width of the distribution of parameters for the 68 (of 100) models with the lowest χ^2 relative to the observed photometry are assumed to represent the errors in those parameters for each individual Voronoi bin. Within a single galaxy, the SED parameter errors of the individual Voronoi bins are averaged together, resulting in a typical Voronoi bin error within the individual galaxy. Finally, the typical Voronoi bin SED parameter error is estimated as the average of the typical Voronoi bin errors from all 50 galaxies in the subsample. The typical SED parameter errors derived from the SEDs fit to the perturbed Voronoi bin fluxes are as follows: 0.03 in $E(B-V)_{\rm stars}$, 0.21 dex in log stellar population age, 0.16 dex in log SFR, and 0.10 dex in log stellar mass.

2.4 Resolved vs. Integrated Properties

In comparing the resolved and integrated stellar population parameters, we must be aware of the different apertures over which the measurements are made, and the slightly different methodology used to fit the SEDs. Specifically, the integrated 3D-HST flux measurements are based on the flux within $0\farcs7$ apertures and are corrected for the contribution from the strongest emission lines that were detected in the MOSFIRE spectra, including [OII]$\lambda3727, 3730$, Hβ, [OIII]$\lambda\lambda4960, 5008$, and Hα (Reddy et al. 2015). The resolved Voronoi bin fluxes, on the other hand, are measured directly from the sum of the flux detected by the pixels in the resolved imaging and are not corrected for the contribution of the emission lines detected by MOSDEF. Additionally, the integrated 3D-HST photometry covers a larger dynamic range in wavelength than the range covered by the filters that are available for resolved photometry due to the ancillary ground-based data that is available. While the *Spitzer*/IRAC photometry is included to increase wavelength coverage of the resolved photometry, we assume that the H_{160}–IRAC colors are fixed across all resolved elements using Equation 2.3. Despite these inherent differences between the integrated and resolved photometry, the $V_{606} - H_{160}$ colors measured from the integrated 3D-HST fluxes and the sum of the flux from all Voronoi bins and outskirt components agree within the measured scatter of 0.3 mag.

The biases that may arise from differences between the resolved and unresolved photometry are explored by directly comparing the associated best-fit SEDs (Section 2.4.1) and SED-derived parameters (Section 2.4.2). In Section 2.4.3, we show how our modified multi-filter Voronoi binning technique can improve upon that using the H_{160} filter alone by comparing the best-fit SEDs and SED-derived parameters from the two techniques. Finally, the implications of our findings on resolved stellar population studies is discussed in Section 2.4.4.

2.4.1 Comparing Best-fit SEDs

The unresolved and summed resolved SEDs for eight galaxies in our sample that span the SED fitting parameter space (low/high $E(B-V)_{\rm stars}$, stellar population age, SFR,

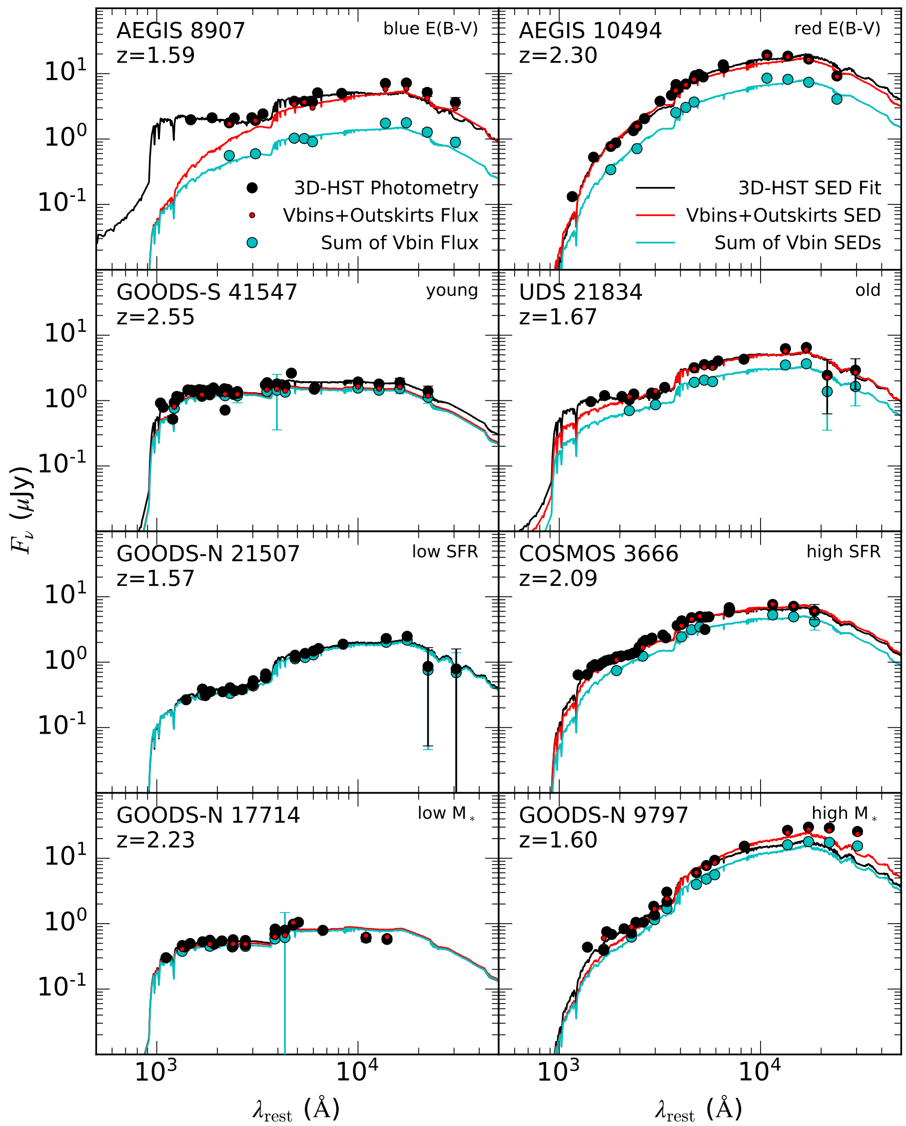

Figure 2.6: Best-fit SEDs for eight example galaxies spanning the SED fitting parameter space. From top to bottom, each row respectively shows example galaxies with low (*left*) and high (*right*) $E(B-V)_{\rm stars}$, stellar population ages, SFRs, and stellar masses. The black points are the fluxes from the 3D-HST photometric catalog (Skelton et al. 2014) corrected for the brightest MOSDEF emission lines and the black curves are their respective best-fit SEDs. The light blue points are the total integrated fluxes within the Voronoi bins (Voronoi bins with S/N ≥ 5 in at least 5 different filters). The light blue curves represent the sum of the SEDs that are best fit to the individual Voronoi bins. The red points indicate the total flux obtained when summing the Voronoi bin and outskirt bin fluxes, which naturally lie close to the values obtained from the 3D-HST photometry. The red curves show the SED fits to the red points. Photometric errors are typically smaller than the size of the points. Note that not all galaxies have outskirt components, such as GOODS-N 21507.

and stellar mass) are shown in Figure 2.6. The summed best-fit SEDs derived from the resolved Voronoi bin photometry (light blue points and curves) are compared to the SEDs derived from the unresolved photometry (black points and curves). The 3D-HST photometry (black points) has extended wavelength coverage and includes more light than the valid Voronoi bins (light blue points)—typically 0.85 mag brighter. The summed Voronoi bin SEDs do not include "outskirt" components, which are defined as low S/N regions in Section 2.3.2. Therefore, Figure 2.6 additionally shows the SEDs that result from adding the outskirt component SEDs to the summed Voronoi bin SEDs (red points and curves). The total flux from the sum of the Voronoi bins and outskirt components is nearly equivalent to the measured flux from the unresolved 3D-HST photometry for filters with resolved imaging (red and black points). Similarly, the summed resolved SEDs that include outskirt components are nearly identical to the unresolved SEDs obtained from the 3D-HST photometry (red and black curves).[5] Note that not all galaxies, such as GOODS-N 21507, have an outskirt component as all of the regions have sufficient S/N to be included as Voronoi bins.

From Figure 2.6, we conclude that the *shapes* of the SEDs are generally well-preserved between the resolved and integrated results (with the exception of galaxies similar to AEGIS 8907, which are further discussed in Section 2.4.2). The primary difference between the resolved and integrated SEDs is the *normalization*, which is attributed to the fact that the Voronoi bins contain less light than the broadband measurements. This causes the Voronoi bins to exhibit systematically lower stellar masses and SFRs compared to the

[5] As stated at the beginning of Section 2.4, small differences between the total flux and the 3D-HST photometry are expected, but generally agree within the uncertainties.

3D-HST photometry (as expected), but on average the offset is less than the uncertainties in the SED-derived stellar masses and SFRs.

2.4.2 Comparison of SED-derived Parameters

The shapes of the resolved SEDs are generally consistent with the unresolved SEDs presented (Figure 2.6), but several galaxies exhibit summed resolved SEDs that are systematically offset from the integrated SED. The $E(B-V)_{\rm stars}$ and stellar population age derived from the SED that is best-fit to the integrated 3D-HST photometry is compared to the average $E(B-V)_{\rm stars}$ and stellar population age derived from the Voronoi bins weighted by the area of each Voronoi bin.[6] The stellar masses and SFRs derived from the SED fit to the integrated photometry is compared to the sum of the stellar mass and SFR within all of the Voronoi bins. While the SED normalization differences caused by different area coverage between the Voronoi bins and integrated photometry do cause systematically lower stellar masses and SFRs, we find that on average all SED-derived parameters inferred from the resolved SEDs are within one standard deviation of those derived from the integrated 3D-HST photometry.

A notable exception is that the resolved SEDs of the $z \sim 1.5$ galaxies are on average redder and younger than indicated by the broadband SED fits, as is showcased by AEGIS 8907 in Figure 2.6. The AEGIS 8907 photometry demonstrates that this discrepancy

[6]Noisy outskirt bins that do not satisfy a S/N ≥ 5 in at least 5 filters are generally not included in the analysis unless specified (see Section 2.3.2). Therefore, the area-weighted average $E(B-V)_{\rm stars}$ and stellar population age of the Voronoi bins for an individual galaxy is not biased towards large outskirt bins with poorly constrained photometry. Furthermore, alternatively weighting individual Voronoi bins by either the H_{160} flux or log stellar mass results in average $E(B-V)_{\rm stars}$ and stellar population ages that are within 1σ of the area-weighted average $E(B-V)_{\rm stars}$ and stellar population ages, such that the results presented here do not change with this alternate treatment.

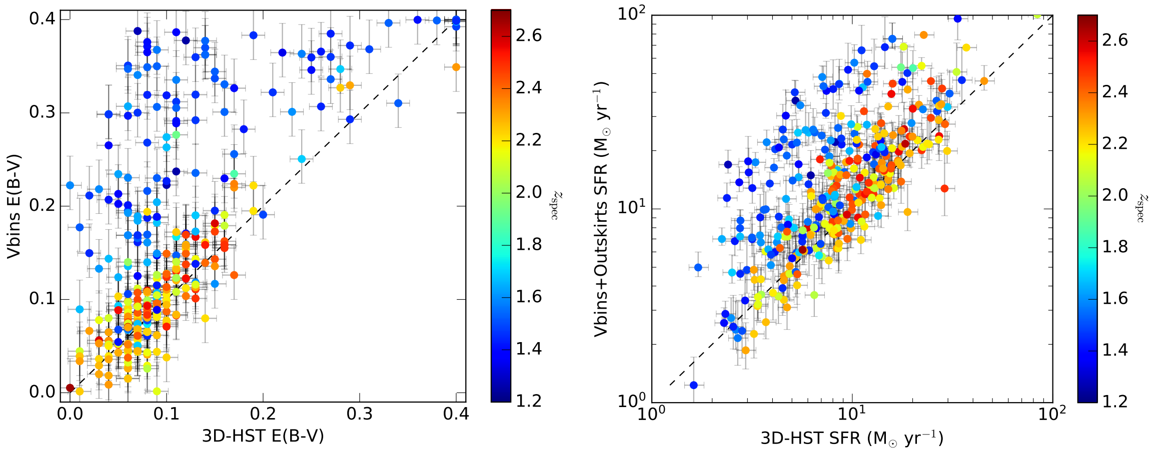

Figure 2.7: *Left:* The average Voronoi bin $E(B-V)_{\rm stars}$ weighted by the area of the Voronoi bins versus the $E(B-V)_{\rm stars}$ derived from the 3D-HST photometry. *Right:* The total SFR of the Voronoi plus outskirt bins versus the SFR derived from the 3D-HST photometry. The points are color-coded by their spectroscopic redshift. The dashed black line indicates where the $E(B-V)_{\rm stars}$ or SFR derived from the Voronoi bins equals those inferred from the 3D-HST photometry. Only the galaxies in the $z \sim 1.5$ sample exhibit $E(B-V)_{\rm stars}$ or SFRs that deviate significantly from those derived from the 3D-HST photometry due to the lack of resolved imaging covering the UV slope (e.g., AEGIS 8907 in Figure 2.6).

is caused by the lack of resolved imaging covering the rest-frame UV for our $z \sim 1.5$ sample. The number of filters that cover the UV slope depends on the field, where all of the $z \sim 1.5$ galaxies in AEGIS, COSMOS, or UDS have only one *HST* filter available that covers the UV slope (1250–2500 Å). We find that the best-fit SEDs prefer redder and younger solutions when the UV slope is unconstrained. Only above redshifts $z \gtrsim 2.1$ do AEGIS, COSMOS, and UDS galaxies have at least two filters covering the UV slope. The left panel of Figure 2.7 demonstrates how the resolved SED fitting of the $z \sim 1.5$ sample produces redder inferred $E(B-V)_{\rm stars}$ compared to those from the unresolved broadband SED fits, while the preference for redder $E(B-V)_{\rm stars}$ completely disappears for the $z \sim 2.3$ sample. Similarly, the right panel of Figure 2.7 shows how the redder $E(B-V)_{\rm stars}$ and younger stellar ages in the $z \sim 1.5$ sample causes the derived SFRs from the Voronoi plus outskirt

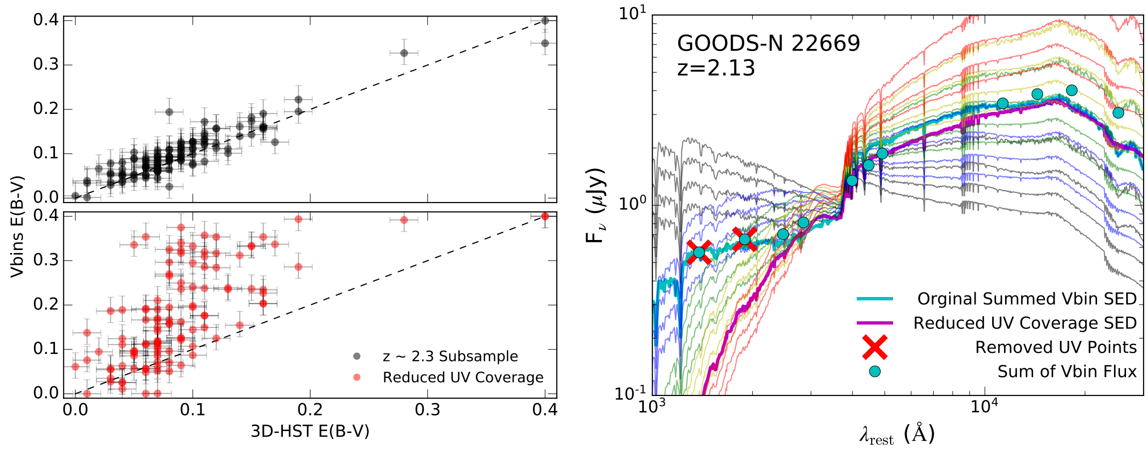

Figure 2.8: *Left:* The average Voronoi bin $E(B-V)_{\rm stars}$ weighted by the area of the Voronoi bins versus the $E(B-V)_{\rm stars}$ derived from the 3D-HST photometry for the $z\sim2.3$ galaxies. The black points show the original $E(B-V)_{\rm stars}$ of the $z\sim2.3$ galaxies (*top*). The red points show how removing the two bluest filters from the $z\sim2.3$ galaxies reproduces the relative reddening observed in the $z\sim1.5$ sample (*bottom*). *Right:* The sum of the model SEDs that best fit the resolved Voronoi bins for GOODS-N 22669 ($z=2.13$). The thick light blue curve shows the summed SED that includes all of the data from the resolved imaging (blue points). The thick purple curve shows the summed SED where the data from the two bluest filters were not included in the SED fitting (red crosses). The faded curves in black, blue, green, yellow, and red represent SED models with $E(B-V)_{\rm stars}$ equal to 0.0, 0.1, 0.2, 0.3, and 0.4, respectively. Several curves of the same color are shown to demonstrate how the SED model shape varies with different stellar population ages when $E(B-V)_{\rm stars}$ is held constant.

bins[7] to be overestimated compared to SFRs inferred from the 3D-HST photometry. The discrepancy between the inferred $E(B-V)_{\rm stars}$ derived from the unresolved and resolved photometry in the $z\sim1.5$ sample occurs at all $E(B-V)_{\rm stars}$ values that are probed by the SED model grid ($0.0\leq E(B-V)_{\rm stars}\leq0.4$) and does not correlate with stellar mass, such that the measured differences in $E(B-V)_{\rm stars}$ are not likely associated with our choice in dust attenuation curve (see footnote 4). However, there may be intrinsic differences in the stellar populations between the two redshift samples.

[7]SFRs inferred from the Voronoi bins alone are lower than those inferred from the 3D-HST photometry because they cover a smaller region of the imaging. Therefore, comparing the SFRs derived from the Voronoi plus outskirt bins is more appropriate for the right panel of Figure 2.7.

In order to further investigate whether the redder inferred $E(B-V)_{\rm stars}$ are caused by the lack of UV slope coverage or differences between the intrinsic stellar populations in the two redshift bins, we select 111 galaxies from our $z \sim 2.3$ sample that have observations in at least 7 resolved *HST* filters. The two bluest filters observed are removed such that only one remaining filter covers the UV slope, with at least 5 resolved filters remaining for the SED fitting. As can be seen in the right panel of Figure 2.7, when the resolved SED fitting (see Section 2.3.4) is repeated we find that the average $E(B-V)_{\rm stars}$ inferred across all Voronoi bins is redder than that inferred when there are additional filters covering the UV slope. Therefore, we conclude that the inferred $E(B-V)_{\rm stars}$ values for the $z \sim 1.5$ sample are overestimated due to there being fewer than 2 filters covering the UV slope. Figure 2.8 shows how the sum of the resolved SEDs changes (thick light blue curve compared to the thick purple curve) when the 2 bluest filters covering the UV slope are removed (red crosses) for GOODS-N 22669 ($z = 2.13$). For context, a subset of the SED models are also shown, where each color represents a step in $E(B-V)_{\rm stars}$ for a range of stellar population ages (i.e., the black, blue, green, yellow, and red SEDs represent SED models with $0 \leq E(B-V)_{\rm stars} \leq 0.4$ in steps of 0.1 mag, respectively). There are three significant features that can be seen in Figure 2.8: 1) when the UV photometry is included, the shape of the best-fit SED is primarily constrained by the rest-frame UV photometry (light blue curve); 2) when the UV photometry is not included, the shape of the best-fit SED is primarily constrained by the rest-frame optical photometry (purple curve); and 3) the SED fits generally under-predict the IRAC photometry. The IRAC photometry may be brighter than what can be fit with the model SEDs in the rest-frame near-IR due to the higher sensitivity and larger aperture over which these measurements are made. Systematically brighter IRAC fluxes and the known discrepancy between stellar population age and extinction in the SED models at optical wavelengths (e.g., Worthey 1994; Shapley et al. 2001) may together explain why there is a bias towards redder best-fit SEDs when the UV slope is unconstrained (such as AEGIS 8907).

The lack of UV slope coverage in the resolved Voronoi bin fitting for the $z \sim 1.5$ sample may complicate inferences of the intrinsic variation in the reddening distribution for these galaxies. However, rather than observing a flat reddening distribution in the $z \sim 1.5$ galaxies, structure is observed in the $E(B-V)_{\rm stars}$ maps (e.g., see Figure 2.5 for UDS 21834 at $z = 1.67$) due to the reddening and ages being constrained in part by the strength of the Balmer/4000 Å breaks in the SED fitting. Finally, we note that the SED-derived SFRs and stellar masses are constrained by the overall normalization of the SED, and they are minimally affected by the lack of observations covering the UV slope.

2.4.3 Traditional Voronoi Binning

In constructing the Voronoi bins in Section 2.3.2, we enforce more stringent requirements (minimum 3 pixels and S/N $\geq$ 5 in 5 filters) than the "traditional" Voronoi binning procedure (S/N $\geq$ 10 in H_{160}) performed in previous studies (Wuyts et al. 2012, 2013, 2014; Genzel et al. 2013; Tadaki et al. 2014; Lang et al. 2014). In this section, the results from our multi-filter Voronoi binning technique is directly compared to the traditional Voronoi binning approach using the same subset of 50 galaxies that were used to determine the typical SED errors (see Section 2.2.4 and Section 2.3.4). Only 50 galaxies are selected for this analysis in the interest of limiting computation time, but the range of SED parameters

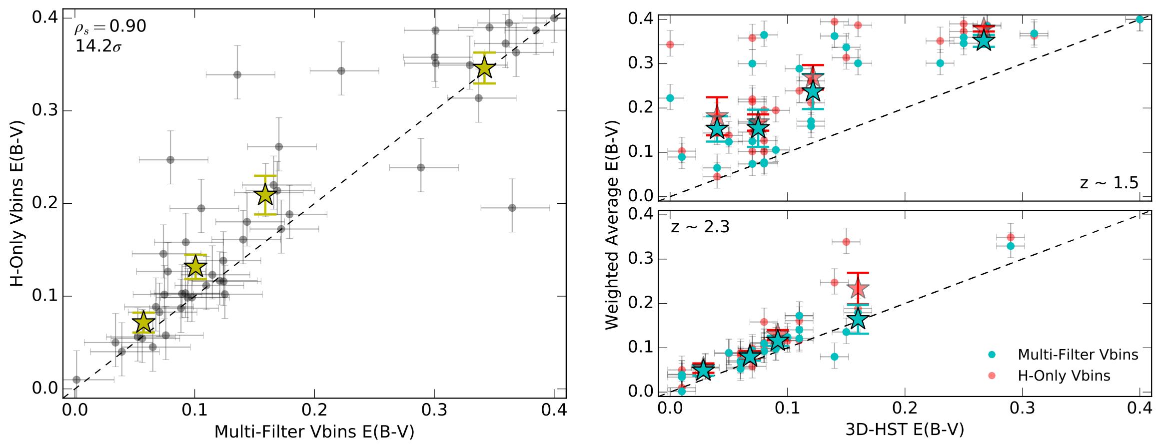

Figure 2.9: *Left:* The average $E(B-V)_{\rm stars}$ weighted by the area of the Voronoi bins derived from the "traditional" Voronoi bins derived from the H_{160} S/N distribution exclusively versus the Voronoi bin distribution derived from several filters (see Section 2.3.2). The Spearman rank correlation coefficient and its significance are listed in the top left corner. *Right:* The average $E(B-V)_{\rm stars}$ weighted by the area of the Voronoi bins derived from both Voronoi binning schemes compared to the $E(B-V)_{\rm stars}$ inferred from the 3D-HST photometry for both redshift samples. The red points represent the "traditional" Voronoi binning technique and the light blue points represent our multi-filter Voronoi binning technique. The red and light blue stars are the averages from individual points equally divided into four bins of $E(B-V)_{\rm stars}$ in the x-axis. The black dashed lines indicate where the $E(B-V)_{\rm stars}$ derived from all sources are equal.

probed by these 50 galaxies is similar to that of the larger sample. The traditional Voronoi bins are constructed using the original Cappellari & Copin (2003) algorithm (version 3.0.4), which exclusively requires each Voronoi bin to attain a S/N $\geq$ 10 in the H_{160} filter alone. Traditional Voronoi bin construction failed for one galaxy, resulting in a final subsample of 49 galaxies for this exercise.

The left panel of Figure 2.9 shows that the average $E(B-V)_{\rm stars}$ inferred across the traditional Voronoi bins determined by the H_{160}-band alone is typically redder (higher) compared to the average $E(B-V)_{\rm stars}$ inferred from the multi-filter determined Voronoi bins. For context, the average $E(B-V)_{\rm stars}$ derived from both Voronoi binning procedures are also compared to the $E(B-V)_{\rm stars}$ derived from the unresolved 3D-HST photometry in the right panel of Figure 2.9. We find that the average $E(B-V)_{\rm stars}$ inferred from the traditional H_{160}-only Voronoi bins (red points and stars) are on average 0.02 mag redder (higher) than our multi-filter approach (light blue points and stars) in both redshift bins, but deviate as much as 0.20 mag. Meanwhile, the $E(B-V)_{\rm stars}$ from our multi-filter approach are 0.10 and 0.02 mag redder (higher) than the 3D-HST globally derived $E(B-V)_{\rm stars}$ (black dashed line) for our $z\sim1.5$ and $z\sim2.3$ samples, respectively. For the $z\sim1.5$ sample, the likely explanation as to why both resolved methods exhibit redder (higher) $E(B-V)_{\rm stars}$ compared those derived from the unresolved 3D-HST photometry is that the UV slope is unconstrained by the available resolved data, as explained in Section 2.4.2. Meanwhile, the differences between the $E(B-V)_{\rm stars}$ derived from our multi-filter technique and the unresolved 3D-HST photometry are on average smaller than the differences in the $E(B-V)_{\rm stars}$ derived from the traditional Voronoi binning technique and the unresolved 3D-HST photometry. This is due to the larger Voronoi bin sizes inherent to our technique that are consequently less resolved compared to Voronoi bins that are defined by a single filter.

The differences observed between the $E(B-V)_{\rm stars}$ inferred from the H_{160} derived Voronoi bins and the multi-filter derived Voronoi bins could also be explained by the high S/N requirement for bluer filters in the multi-filter technique, in that it will force blue regions of the galaxy to be included with intrinsically red regions. Forcing additional blue light to be included with intrinsically red regions would cause the multi-filter Voronoi bins to typically exhibit systematically shallower UV slopes compared to traditionally defined Voronoi bins—particularly those covering the reddest regions of the galaxy. Therefore, in

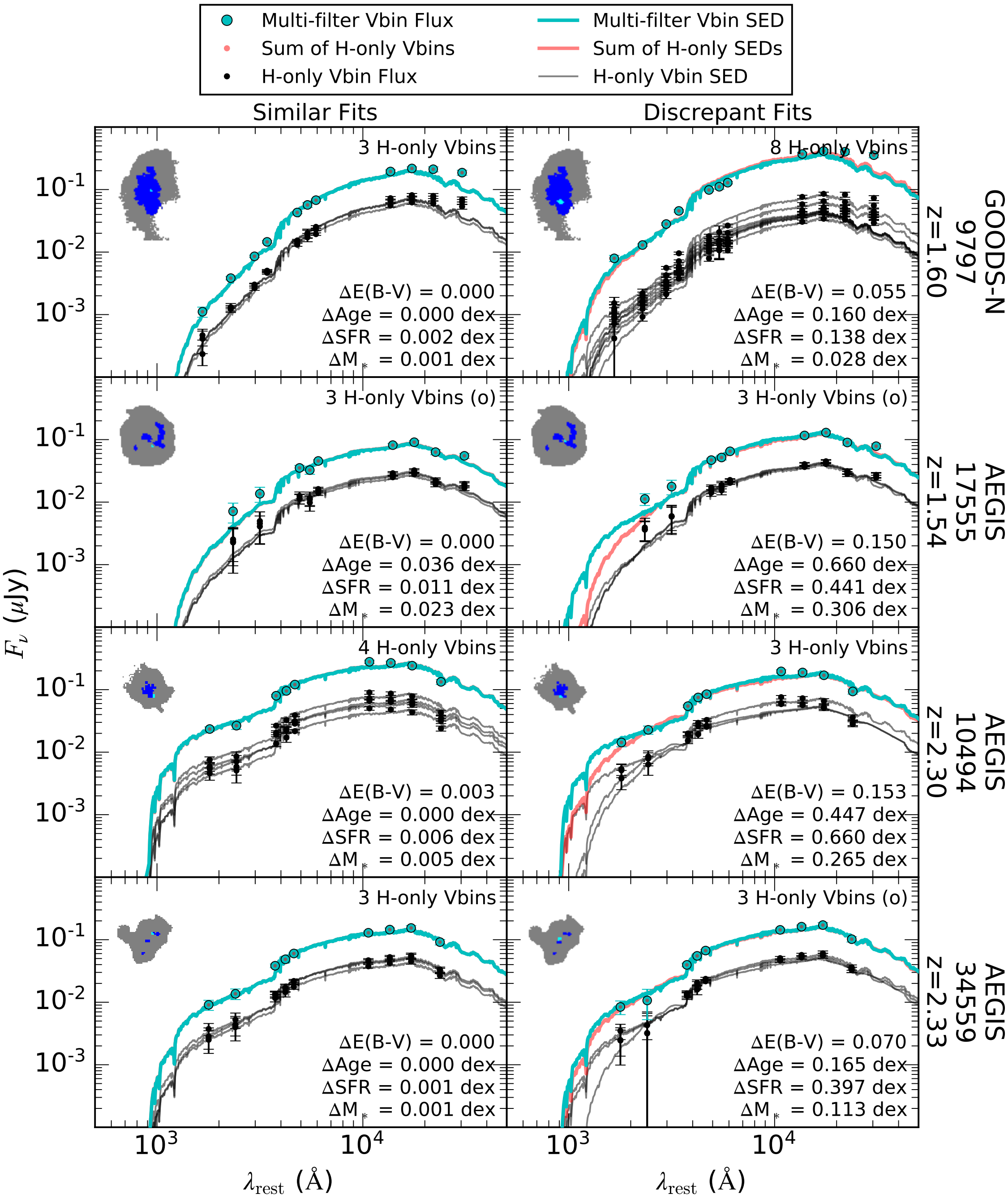
Multi-filter Vbin Flux
Sum of H-only Vbins
H-only Vbin Flux
Multi-filter Vbin SED
Sum of H-only SEDs
H-only Vbin SED
Similar Fits
Discrepant Fits
3 H-only Vbins
ΔE(B-V) = 0.000
ΔAge = 0.000 dex
ΔSFR = 0.002 dex
ΔM* = 0.001 dex
8 H-only Vbins
ΔE(B-V) = 0.055
ΔAge = 0.160 dex
ΔSFR = 0.138 dex
ΔM* = 0.028 dex
GOODS-N 9797 z=1.60
3 H-only Vbins (o)
ΔE(B-V) = 0.000
ΔAge = 0.036 dex
ΔSFR = 0.011 dex
ΔM* = 0.023 dex
3 H-only Vbins (o)
ΔE(B-V) = 0.150
ΔAge = 0.660 dex
ΔSFR = 0.441 dex
ΔM* = 0.306 dex
AEGIS 17555 z=1.54
4 H-only Vbins
ΔE(B-V) = 0.003
ΔAge = 0.000 dex
ΔSFR = 0.006 dex
ΔM* = 0.005 dex
3 H-only Vbins
ΔE(B-V) = 0.153
ΔAge = 0.447 dex
ΔSFR = 0.660 dex
ΔM* = 0.265 dex
AEGIS 10494 z=2.30
3 H-only Vbins
ΔE(B-V) = 0.000
ΔAge = 0.000 dex
ΔSFR = 0.001 dex
ΔM* = 0.001 dex
3 H-only Vbins (o)
ΔE(B-V) = 0.070
ΔAge = 0.165 dex
ΔSFR = 0.397 dex
ΔM* = 0.113 dex
AEGIS 34559 z=2.33
F_ν (μJy)
10^{-1}
10^{-2}
10^{-3}
10^3
10^4
$\lambda_{\rm rest}$ (Å)

Figure 2.10: Examples of the best-fit SEDs from the Voronoi bins built from the H_{160} filter alone compared to best-fit SED of the single Voronoi bin constructed from our multi-filter procedure (Section 2.3.2) that covers the same physical area as the H_{160}-only Voronoi bins. The black points represent the fluxes within the H_{160}-only Voronoi bins, which add up to the fluxes from a single, larger Voronoi bin built using our new criteria (light blue/red points). The errors for the light blue/red points are typically smaller than the size of the points. The gray curves are the SEDs that are best fit to the H_{160}-only Voronoi bin fluxes. The red curves represent the sum of the gray curves and are generally hidden behind the light blue curves that represent the SEDs that are best fit to the individual Voronoi bin constructed from our multi-filter procedure. The number of H_{160}-only Voronoi bins is listed in the top right corner of each panel and an (o) is shown if the matched multi-filter Voronoi bin is considered an outskirt component. The values in the bottom right corner of each panel show the differences in $E(B-V)_{\rm stars}$, stellar population age, SFR, and stellar mass inferred from the integrated H_{160}-only Voronoi bin SEDs versus the individual Voronoi bin from our multi-filter procedure. The image in the top left corner of each panel shows for each galaxy: the segmentation map area in gray, the area where the Voronoi bins have a $S/N \geq 5$ in at least 5 filters in dark blue, and the individual Voronoi bin that is represented by the curves in light blue. The two columns show examples where the summed SEDs (light blue and red curves) are similar (*left column*) or discrepant (*right column*) compared to each other.

Figure 2.10, the resolved SEDs that cover the same spatial areas from the two methodologies are directly compared such that they have the same total fluxes (light blue and red points). Individual Voronoi bins built from the multi-filter procedure (Section 2.3.2) are typically larger than traditionally constructed Voronoi bins based only on the H_{160} filter. Specifically, Figure 2.10 shows examples of the resolved SEDs from the traditional Voronoi bins (black points and gray curves) that entirely make up an individual Voronoi bin from the multi-filter procedure (light blue points and curves). As can be seen, there are examples where the shape of the summed SEDs derived from the traditionally defined H_{160}-only Voronoi bins (light blue curves) either matches (left column) or deviates (right column) from the shape of the SEDs derived from the multi-filter Voronoi bins covering the same region (red curves). Based on the matching UV slopes from the examples shown in the left column of Figure 2.10 and the fact that the discrepant SED examples in the right column have been compared over the same resolved regions where all filters contain the same total flux, we conclude that bluer light being forced into the multi-filter Voronoi bins does not serve as an adequate explanation to the observed systematic difference between the $E(B-V)_{\rm stars}$ inferred from the two methodologies in Figure 2.9. However, Figure 2.10 also shows that the best-fit SEDs from the multi-filter technique are typically more tightly constrained by the higher S/N photometry than the SEDs fit to the smaller Voronoi bins constructed from the H_{160} filter alone. The inclusion of any resolved components with low S/N at short wavelengths appears to cause the summed best-fit SEDs to exhibit steeper UV slopes that result in redder (higher) $E(B-V)_{\rm stars}$ for galaxies in both the $z \sim 1.5$ and $z \sim 2.3$ samples (right column of Figure 2.10). Furthermore, since the discrepancy between the UV slopes of the two Voronoi binning methods is observed in both of our redshift bins, it is important to note that the redder inferred $E(B-V)_{\rm stars}$ from the summed traditional SEDs is independent from the redder $E(B-V)_{\rm stars}$ that are caused by the lack of resolved UV slope coverage in the $z \sim 1.5$ sample (see Section 2.4.2). Overall, the preference towards redder SEDs tends to occur when the UV slope is generally poorly constrained (in this case by large photometric errors or, as discussed in Section 2.4.2, limited data).

Based on the results presented here, we find that traditionally defined Voronoi bins result in resolved SEDs that are *systematically redder* (higher $E(B-V)_{\rm stars}$) than multi-filter defined Voronoi bins. This systematic effect is due to the lower S/N in bluer filters when constructing Voronoi bins based only on the distribution of H_{160}-band light. By extension, we expect SED fitting across individual pixels to exhibit redder (higher) $E(B-V)_{\rm stars}$ as well. In order to best constrain the shape of the SEDs that are fit to resolved photometry, we recommend using a binning procedure that enforces high S/N across both blue and red resolved filters—especially covering the UV slope and Balmer/4000 Å breaks. Additionally, caution should be taken when including regions that have low S/N overall (i.e., "outskirt" components) in resolved studies.

2.4.4 Discussion

The structure of high-redshift galaxies can give insight into the evolution of galaxies on resolved scales (see Conselice 2014). In particular, the SFR of a galaxy is an important measure of how galaxies build their stellar mass. However, the intrinsic SFR of a galaxy must be inferred by correcting for the obscuring effects of dust. The scattering and attenuation of starlight by dust depends on the amount and distribution of dust (e.g., Draine & Lee 1984;

Fitzpatrick & Massa 1986; Calzetti et al. 1994, 2000), which is typically accounted for by assuming an attenuation curve. Obtaining accurate dust reddening on resolved scales may inform the assumptions made when fitting unresolved photometry, such as the slope and shape of the dust attenuation curve (Reddy et al. 2018a; Shivaei et al. 2020). While stellar masses are generally quite robust to methodology, we have shown throughout this paper that the inferred resolved reddening can be difficult to constrain due to a combination of the age-extinction-metallicity degeneracy (Worthey 1994; Shapley et al. 2001; see Appendix B), unconstrained UV slopes (see Section 2.4.2), and generally low S/N resolved rest-frame UV photometry (see Section 2.4.3). In such cases, Voronoi bins constructed based on multiple filters may be desirable in order to obtain more robust resolved stellar population parameters and, in particular, robust reddening maps.

In Appendix B, we discussed how constraining the Balmer/4000 Å breaks is important for breaking the age-extinction degeneracy (Worthey 1994; Shapley et al. 2001), particularly for galaxies at $z > 2.5$ where the Balmer/4000 Å breaks shift into the H_{160} filter. Through our choice of normalizing the unresolved IRAC photometry by the resolved H_{160} flux, we made the assumption that the resolved H_{160}–IRAC colors are constant across all bins in each galaxy. We showed that constraining the H_{160}–IRAC colors does not significantly influence the distribution of stellar population ages and reddening within galaxies. While only 15 galaxies in our sample are at $z > 2.5$, constraining the Balmer/4000 Å breaks by assuming a constant H_{160}–IRAC color distribution may be a viable solution for resolved studies at higher redshifts.

Throughout this paper, we showed that if the UV slope is not well-constrained by the resolved photometry, such as at lower redshifts ($z < 2.1$; see Section 2.4.2) or by low S/N regions (see Section 2.4.3), then the derived resolved stellar populations properties may be biased towards SEDs with redder (higher) $E(B-V)_{\rm stars}$. If the inferred $E(B-V)_{\rm stars}$ is overestimated, then observed SFRs may consequently be overcorrected for dust attenuation, which would result in the inferred intrinsic SFRs also being overestimated (see Figure 2.7). This observational reddening bias most significantly affects our $z \sim 1.5$ sample, where only one resolved filter covers the UV slope (see Section 2.4.2), but more generally this systematic bias has a greater influence on intrinsically blue galaxies (young, dust-free stellar populations) opposed to intrinsically red galaxies (old, dusty stellar populations). A Wuyts et al. (2012) methodology can be implemented to adjust the resolved SEDs to better reproduce the integrated SED shape in cases where it is not possible to obtain at least two resolved filters covering the UV slope (1250–2500 Å), but at the cost of increased uncertainty in the specific distribution of the resolved stellar population properties (see Appendix A). For galaxies where the resolved UV slope is not well-constrained due to low S/N, we introduced a technique in Section 2.3.2 that increases the S/N across all resolved filters to produce more reliable SEDs that are fit to the resolved photometry at the cost of a marginally decreased resolution compared to previous methods (see Section 2.4.3). Our multi-filter Voronoi binning technique increases the number of resolved elements that can confidently recover resolved stellar population parameters through SED fitting, particularly for galaxies with low surface brightness or extended diffuse light.

Based on the analyses presented throughout this paper, we provide a list of recommendations for confidently deriving resolved stellar population properties. 1) If possible, ensure that at least two photometric observations span key rest-frame SED features, particularly the UV slope and Balmer/4000 Å breaks. 2) Incorporate a binning technique that either includes information about the S/N distribution of both red and blue filters or otherwise ensures that at least 5 filters are significantly detected—especially shorter wavelength filters that are typically lower S/N. 3) Generally be wary of biases that may exist between resolved properties that are inferred from well- (e.g., full wavelength coverage, S/N $\geq$ 5 in 5 filters) versus poorly-constrained (e.g., unconstrained SED features, "outskirt" components) SEDs.

2.5 Summary

In this paper, we presented an improved Voronoi binning technique for studying resolved stellar populations at high redshifts, which overall aims to increase the confidence in the best-fit SEDs and stellar population properties that are derived from the resolved photometry. The layout of the resolved components for performing resolved SED fitting was determined from the S/N distribution of multiple filters in the high-resolution CANDELS/3D-HST imaging for a sample of 350 star-forming galaxies drawn from the MOSDEF survey at spectroscopic redshifts $1.25 < z < 2.66$. The stellar population and dust maps were constructed based on our new multi-filter Voronoi binning technique and their integrated stellar population properties were compared to those derived from the unresolved broadband imaging and those derived from a "traditional" Voronoi binning approach that used the H_{160} filter alone to determine Voronoi bins. Our main conclusions are summarized as follows.

- In Section 2.3.2, we described a modified Voronoi binning technique (see Figure 2.2) that accounts for the S/N distribution of multiple resolved filters opposed to the H_{160} filter alone. In order for an individual Voronoi bin to be included in our analysis, we required the bin to contain a S/N ≥ 5 in at least 5 resolved filters. Any bins that did not satisfy this criteria were deemed "outskirt" components (see Figure 2.3).

- We found that the shapes of the summed resolved SEDs from our multi-filter binning technique were generally consistent with the SEDs that were fit to the unresolved broadband photometry (see Figure 2.6) in Section 2.4.1. Similarly, in Section 2.4.2 we found that the average $E(B-V)_{\rm stars}$, average stellar population ages, summed SFRs, and summed stellar masses are typically within 1σ of the stellar population properties derived from the unresolved broadband photometry.

- The most significant deviation between the resolved and unresolved SEDs and best-fit stellar population parameters was the shape of the UV slope and the average $E(B-V)_{\rm stars}$ inferred from the resolved reddening maps for galaxies in the $z \sim 1.5$ sample (see Figure 2.7). By removing rest-frame UV photometry from the $z \sim 2.3$ sample and repeating the resolved SED fitting, we determined in Section 2.4.2 that the discrepancy in the $z \sim 1.5$ inferred reddening is most likely caused by the lack of data that is able to constrain the UV slope (1250–2500 Å).

- When comparing our multi-filter Voronoi binning technique (S/N $\geq$ 5 in at least 5 filters) with a "traditional" single-filter approach (S/N $\geq$ 10 in H_{160}) in Section 2.4.3, we found that the single-filter technique results in $E(B-V)_{\rm stars}$ values that are *systematically redder* by 0.02 mag on average than our multi-filter method, but could deviate by as much as 0.20 mag (see Figure 2.9). We also found that our multi-filter technique produces average inferred $E(B-V)_{\rm stars}$ that are closer to those derived from the unresolved broadband photometry compared to the single-filter approach, but we note that this may be expected from the larger (i.e., lower resolution) bins that are inherent to our technique. We also demonstrated through Figure 2.10 that systematically redder UV slopes may result from poorly constrained rest-frame UV photometry, which can occur in the smaller, traditionally defined Voronoi bins. Finally, we note that SED-derived stellar masses remain robust between methodologies when all Voronoi bins are included.

The methodology presented here will be applied to future resolved analyses using the MOSDEF dataset, which will additionally incorporate results from the rest-frame optical emission line measurements. In general, we advocate for a methodology that best constrains the SEDs that are best-fit to the resolved photometry. Well-constrained SEDs can generally be obtained by using high S/N multi-band photometry that covers key features in the rest-frame SED (i.e., UV slope, Balmer/4000 Å breaks). Furthermore, low S/N "outskirt" regions could be excluded from analyses, otherwise biases between well- versus poorly-constrained resolved SEDs must be understood when interpreting the results. Finally, we note that higher confidence in resolved stellar population parameters through the methods presented here comes at the cost of lower resolution. However, these methods will similarly push to higher resolutions when applied to future high-resolution imaging instruments, such as the NIRcam on the upcoming *James Webb Space Telescope*.

Chapter 3

Paper II: The Dependency of Hα-to-UV SFR Ratios on SFR and Size at $z \sim 2$[1]

Abstract We perform an aperture-matched analysis of dust-corrected Hα and UV SFRs using 312 star-forming galaxies from the MOSFIRE Deep Evolution Field (MOSDEF) survey at spectroscopic redshifts $1.36 < z < 2.66$. By combining Hα and Hβ emission line measurements with multi-waveband resolved CANDELS/3D-HST imaging, we directly compare measurements of dust-corrected Hα and UV SFRs that account for the spectroscopic slit area. Previous studies have found that Hα and UV SFRs generally agree for typical

[1]This chapter contains a draft of an article that has been submitted for publication by Oxford University Press in the Monthly Notices of the Royal Astronomical Society written by Tara Fetherolf, Naveen A. Reddy, Alice E. Shapley, Mariska Kriek, Brian Siana, Alison L. Coil, Bahram Mobasher, William R. Freeman, Ryan L. Sanders, Sedona H. Price, Irene Shivaei, Mojegan Azadi, Laura de Groot, Gene C.K. Leung, and Tom O. Zick.

star-forming galaxies, but become increasingly discrepant for galaxies with higher SFRs ($\gtrsim$100 $M_\odot$ yr^{-1}), with Hα-to-UV SFR ratios being larger for these galaxies. Our analysis suggests that this trend persists even after carefully accounting for the apertures over which Hα and UV-based SFRs (and the nebular and stellar continuum reddening) are derived. Furthermore, we find an overall increase in the normalization of the relationship between Hα-to-UV SFR ratios and Hα SFRs when measured across the spectroscopic aperture, suggesting that galaxies that extend beyond the spectroscopic aperture (i.e., galaxies that are large in size) exhibit higher Hα-to-UV SFR ratios in their centers. We also find that the offset from the observed trend between Hα-to-UV SFR ratios and Hα SFRs is correlated with galaxy size. These results may be explained by centrally-peaked Hα emission or nebular reddening where the Hα and UV light profiles do not necessarily match at all radii. These observations are indicative of a patchier distribution of dust in galaxies with high SFRs.

3.1 Introduction

Galaxies were rapidly assembling their stellar mass at $z \sim 2$ when cosmic star-formation activity was at its peak (see Madau & Dickinson 2014). An important measure of how galaxies build their stellar mass is their star-formation rate (SFR). The SFR of galaxies in the local universe has been probed by observations of the ultraviolet (UV) continuum, nebular emission lines (e.g., Hα, Hβ, Brγ), mid- and far-infrared (IR) continuum, radio continuum, X-ray emission, and combinations of these tracers (e.g., Kennicutt 1998; Kennicutt & Evans 2012; Hao et al. 2011). SFR measurements for higher redshift galaxies, however, typically rely on a limited set of tracers. For example, at higher redshifts, the longer-wavelength tracers are of limited use as typical unlensed galaxies are not directly detected at these wavelengths. As such, we must rely on SFR indicators that can be accessed for individual high-redshift galaxies (e.g., UV continuum, Hα, Hβ), which require corrections for the obscuring effects of dust.

Dust obscuration can be directly probed by comparing the measured Balmer decrement (Hα/Hβ) to the intrinsic Balmer decrement expected from typical conditions in the interstellar medium (ISM; Osterbrock 1989). This method is sensitive to the reddening towards the youngest stellar populations that host the most massive stars. An alternative method for estimating dust obscuration is to measure the slope of the UV continuum (Calzetti et al. 1994; Meurer et al. 1999). In general, these two measures for obscuration cannot be used interchangeably. Several studies of high-redshift galaxies have observed higher reddening at a fixed wavelength towards the most massive stars ($E(B-V)_{\rm gas}$) compared to the stellar continuum ($E(B-V)_{\rm stars}$) by a constant factor (e.g., Meurer et al. 1999; Calzetti et al. 2000; Kashino et al. 2013; Price et al. 2014; Tacchella et al. 2018) or as a function of SFR (Yoshikawa et al. 2010; Kreckel et al. 2013; Reddy et al. 2015), specific SFR (Wild et al. 2011; Price et al. 2014; Boquien et al. 2015; Reddy et al. 2015; Hemmati et al. 2015), SFR surface density (Boquien et al. 2015), and metallicity (Shivaei et al. 2020).

Once appropriate dust corrections have been applied, Hα and UV SFRs have been found to generally agree for most star-forming galaxies at high-redshifts (e.g., Erb et al. 2006a; Reddy et al. 2010; Wuyts et al. 2013; Steidel et al. 2014; Reddy et al. 2015; Shivaei et al. 2015a, 2020; Theios et al. 2019; Shivaei et al. 2020). However, some authors have found that SFRs derived from nebular emission are higher systematically than those inferred from the UV continuum in high-redshift galaxies with high SFRs ($\gtrsim$100 $M_\odot$ yr^{-1}; Hao et al. 2011; Reddy et al. 2015; Katsianis et al. 2017). Variations in SFRs derived using different tracers may result from their sensitivity to star formation on different timescales (Reddy et al. 2012; Price et al. 2014), which could provide useful information about the initial mass function (IMF) or star-formation history (SFH) of galaxies (Madau & Dickinson 2014), or could alternatively be caused by incorrect assumptions regarding dust corrections.

A non-uniform distribution of dust and stars has been invoked to explain the observed differences between nebular and stellar continuum reddening (Calzetti et al. 1994; Wild et al. 2011; Price et al. 2014, Reddy et al. 2020, in press), and could also potentially explain the observed variations in Hα- and UV-based SFRs (Boquien et al. 2009, 2015; Hao et al. 2011; Reddy et al. 2015; Katsianis et al. 2017). The young massive stars that dominate the nebular line emission ($\gtrsim$15 $M_\odot$; Kennicutt & Evans 2012) may be enshrouded in their parent birth clouds, while the UV continuum is dominated by stars over a larger range of main sequence lifetimes (10–200 Myr; Kennicutt & Evans 2012). However, some of the less massive O and B stars will survive the disruption and dissipation of their birth clouds (Calzetti et al. 1994; Boquien et al. 2015; Faisst et al. 2017; Narayanan et al. 2018) and will disproportionally add to the UV continuum light compared to the contribution from the majority of the unobscured stars. On the other hand, Reddy et al. (2020, in press) recently suggested that the differences between the nebular emission and UV continuum reddening do not necessarily need to be connected to the dust in the molecular phase of the ISM. Alternatively, the dust that is reddening the nebular emission could additionally originate from the non-ionized or neutral gas phase of the ISM with the youngest OB associations still located in regions of higher dust column density on average.

From a practical standpoint, if geometrical effects within galaxies are at play for explaining variations in the reddening and SFRs, then the assumptions that are used to correct spectroscopic emission line measurements for light falling outside of the slit aperture may be inaccurate (Kewley et al. 2005; Richards et al. 2016; Green et al. 2017). If the spectroscopic emission line measurements are not corrected for slit-loss, then Hα SFRs would be underestimated and UV SFRs would be higher than Hα SFRs. However, total Hα SFRs could also be over or underestimated if inappropriate assumptions are made about the Balmer decrement or Hα light radial profiles, which have been observed to be centrally peaked in $z \sim 2$ galaxies (e.g., Nelson et al. 2013, 2016; Hemmati et al. 2015; Tacchella et al. 2018). Furthermore, the average Balmer decrement measured across the spectroscopic slit may not necessarily be indicative of the globally averaged Balmer decrement, and could contribute to any discrepancies between $E(B-V)_{\rm gas}$ and the globally-measured $E(B-V)_{\rm stars}$. Therefore, it is important to identify the significance of any "aperture" biases when comparing spectroscopic measurements of nebular emission lines with measurements of the UV continuum, the latter of which is typically performed on the whole galaxy.

In this study, we investigate how aperture effects influence the interpretation of SFRs and reddening derived from UV and nebular emission line observations. We pair rest-frame optical spectra from the MOSFIRE Deep Evolution Field survey (MOSDEF; Kriek et al. 2015) with multi-waveband resolved imaging from the Cosmic Assembly Near-infrared Deep Legacy Survey (CANDELS; Grogin et al. 2011; Koekemoer et al. 2011). Targets for the

MOSDEF survey were selected from the five CANDELS extragalactic fields in three redshift bins ($z \sim 1.5$, $z \sim 2.3$, and $z \sim 3$) that also have overlapping grism observations from the 3D-HST survey (Brammer et al. 2012; Skelton et al. 2014). The MOSDEF survey obtained rest-frame optical spectra for ~1500 star-forming and AGN galaxies at $1.4 \lesssim z \lesssim 3.8$. Here we take advantage of the statistically large MOSDEF spectroscopic survey by analyzing a sample of 312 star-forming galaxies with detected Hα and Hβ emission at $z \sim 2$.

Our data and sample selection are presented in Section 3.2. In Section 3.3, we describe our methodology for measuring dust-corrected Hα and UV SFRs directly within the MOSFIRE spectroscopic slit region. We then compare the globally measured dust-corrected SFRs to those measured inside the spectroscopic aperture and discuss our findings in Section 3.4. Finally, our results are summarized in Section 3.5.

Throughout this paper, we assume a cosmology with $H_0 = 70\,\mathrm{km\,s^{-1}\,Mpc^{-1}}$, $\Omega_\Lambda = 0.7$, and $\Omega_m = 0.3$. All line wavelengths are in vacuum and all magnitudes are expressed in the AB system (Oke & Gunn 1983).

3.2 Data and Sample Selection

3.2.1 CANDELS/3D-HST Photometry

CANDELS (Grogin et al. 2011; Koekemoer et al. 2011) observed ~900 arcmin^2 of the sky and achieved 90% completeness at $H_{160} \sim 25$ mag covering five well-studied extragalactic fields: AEGIS, COSMOS, GOODS-N, GOODS-S, and UDS. We use the multi-wavelength *HST*/WFC3 (F125W, F140W, and F160W filters, hereafter J_{125}, JH_{140}, and H_{160}) and *HST*/ACS (F435W, F606W, F775W, F814W, and F850LP filters, hereafter B_{435},

V_{606}, i_{775}, I_{814}, and z_{850}) resolved CANDELS imaging that has been processed by the 3D-HST grism survey team (Brammer et al. 2012; Skelton et al. 2014; Momcheva et al. 2016). The publicly-available[2] processed CANDELS images have been drizzled to a $0\farcs06\,\mathrm{pixel}^{-1}$ scale and PSF-convolved to the spatial resolution of the H_{160} imaging ($0\farcs18$). We also use the broadband photometric catalogs provided by the 3D-HST team, which cover 0.3 to 8.0 μm in the five extragalactic CANDELS fields.

3.2.2 MOSDEF Spectroscopy

Targets were selected for the MOSDEF survey in three redshift bins ($1.37 < z < 1.70$, $2.09 < z < 2.61$, and $2.95 < z < 3.80$) using the 3D-HST photometric and spectroscopic catalogs. In order to reach a stellar mass limit of $\sim 10^9\,\mathrm{M}_\odot$ for all three redshift bins, an H_{160}-band limit of 24.0, 24.5, and 25.0 mag was used for the $z \sim 1.5$, $z \sim 2.3$, and $z \sim 3$ bins, respectively. These redshift bins were selected such that the following strong rest-frame optical emission lines fall in near-IR windows of atmospheric transmission: [OII]$\lambda3727, 3730$, Hβ, [OIII]$\lambda\lambda4960, 5008$, Hα, [NII]$\lambda\lambda6550, 6585$, and [SII]$\lambda6718, 6733$.

Observations for the recently-completed MOSDEF survey were taken over 4.5 years on the 10 m Keck I telescope using the MOSFIRE multi-object spectrograph (McLean et al. 2010, 2012) in the Y, J, H, and K bands ($R = 3400$, 3000, 3650, and 3600 using $0\farcs7$ slit widths). Rest-frame optical spectra were obtained for $\sim$1500 galaxies at $1.4 \lesssim z \lesssim 3.8$. Every slit mask included at least one slit star, which is used, in part, for the absolute flux calibration of the spectra and to correct for slit losses. Given that the typical seeing during the observations is on order the same as the width of the slit at $0\farcs7$, using a point source

[2] https://3dhst.research.yale.edu/

slit star is insufficient to correct the spatially-resolved MOSDEF galaxy targets for light lost outside of the spectroscopic slit. Therefore, to best account for additional slit loss, a secondary correction is applied to the spectrum of each galaxy in each near-IR filter. This correction is based on a 2D rotated elliptical Gaussian that is fit to the 3D-HST H_{160} image of the galaxy that has been convolved to the typical seeing during the observation through the relevant filter (Reddy et al. 2015). See Kriek et al. (2015) for further details on the MOSDEF survey, including the observation strategy and data reduction.

Line Flux Measurements

Line fluxes are measured by fitting a linear function to the continuum and a Gaussian function to each emission line, with double and triple Gaussians fit to the [OII]$\lambda\lambda 3727, 3730$ doublet and Hα+[NII]$\lambda\lambda 6550, 6585$ lines, respectively. Hα and Hβ line fluxes are corrected for underlying Balmer absorption using the stellar population model that best fits the observed 3D-HST broadband photometry (Section 3.3.2). Flux errors are obtained by perturbing the 1D spectra by their error spectra 1000 times, remeasuring the line fluxes, and taking the 68th-percentile width of the distribution. Finally, the observed wavelength of the highest signal-to-noise (S/N) line, which is usually Hα or [OIII]$\lambda 5008$, is used to estimate the spectroscopic redshift. For more details on the emission line flux measurements, see Reddy et al. (2015).

3.2.3 Sample Selection

The sample selection used for our analysis is described as follows. Our sample is derived from the MOSDEF parent sample in the $z \sim 1.5$ and $z \sim 2.3$ redshift bins, where both the Hα and Hβ emission lines are covered by the ground-based spectroscopy. In order to optimally measure Balmer decrements and correct for slit loss, both Hα and Hβ are required to be detected with a S/N ≥ 3. However, we also consider an "initial" sample where Hβ is undetected (S/N < 3), but still covered by the observations, to investigate a possible bias against the dustiest galaxies. AGNs are identified through their X-ray luminosities, optical emission lines ($\log([\text{NII}]/\text{H}\alpha) > -0.3$), and/or mid-IR luminosities (Coil et al. 2015; Azadi et al. 2017, 2018; Leung et al. 2019), then removed from our sample.

With these requirements, our initial and primary samples include 675 and 449 star-forming galaxies, respectively, at $1.24 < z < 2.66$. The primary sample includes 19 galaxies that fall outside of the targeted MOSDEF redshift bins, as these targets were serendipitously detected. When the CANDELS *HST* images are smoothed to the seeing of the MOSFIRE observations (see Section 3.3.1), 25 galaxies are undetected in the segmentation maps based on the smoothed images and are removed from our sample. After modeling the stellar populations globally and within the slit area (see Section 3.3.2), we find that the SED-derived SFRs (i.e., UV SFRs) of 112 galaxies are measured to be higher inside the slit than across the entire galaxy—which is unphysical and primarily caused by key features of the SED being unconstrained (e.g., UV slope, Balmer/4000 Å breaks; see Section 3.3.2). Therefore, we remove these galaxies from our sample as well, resulting in a final sample size of 312 star-forming galaxies at $1.36 < z < 2.66$.

Figure 3.1 shows the spectroscopic redshift distribution and SFR–M_* "star-forming main sequence" relation for the galaxies in our primary sample (312 galaxies; filled gray circles) compared to the initial sample (675 galaxies; empty circles). As a visual aid, our

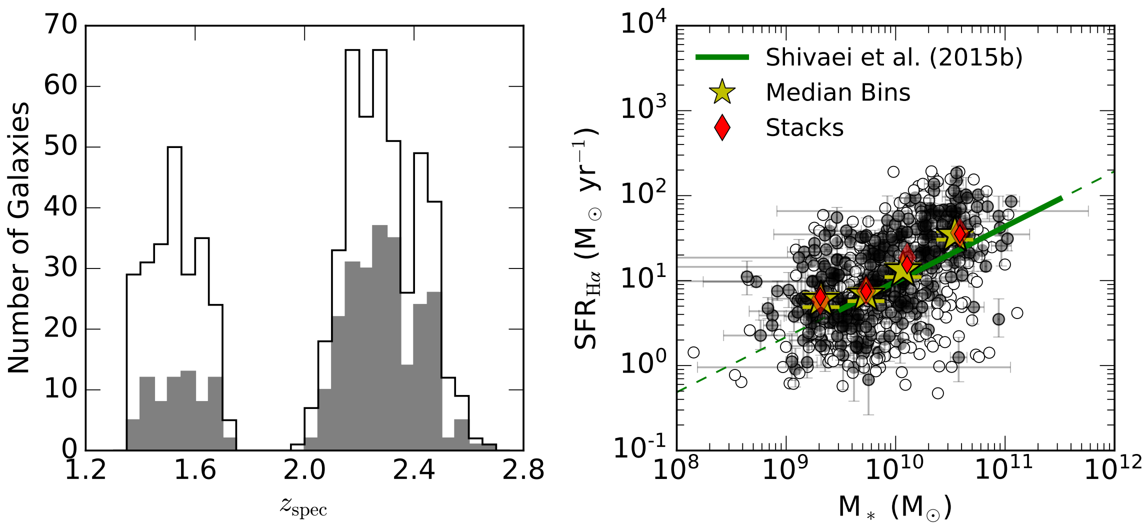

Figure 3.1: *Left:* The distribution of spectroscopic redshifts for our sample covering two redshift bins: $1.24 < z < 1.74$ and $1.99 < z < 2.66$. The spectroscopic redshifts of the initial sample (675 galaxies) are shown by the white histogram. The final sample (312 galaxies), where all galaxies are detected with a $S/N \geq 3$ in Hα and Hβ emission, is denoted by the gray histogram. *Right:* Our sample relative to the star-forming main sequence (i.e., Hα SFR versus stellar mass). Hα emission is corrected for dust reddening by using the Balmer decrement and assuming the Cardelli et al. (1989) extinction curve. A Chabrier (2003) IMF and 20% Solar metallicity is also also assumed when calculating Hα SFRs (see Section 3.3.3). The linear relation that is best-fit to the star-forming main sequence using the first two years of data from the MOSDEF survey (Shivaei et al. 2015b) is shown by the solid green line and is extended with a dashed line for visual clarity. The MOSDEF spectra are stacked in four equal bins of stellar mass for both our initial (large faded red diamonds) and final (small filled red diamonds) samples, respectively, showing that our sample is not biased against the dustiest galaxies where Hβ is not detected. The galaxies in our initial (675) and final (312) samples are shown by the empty and filled circles, respectively. The sample is also divided equally into four bins of stellar mass to show the medians of the individual measurements for the 312 galaxies in our sample (yellow stars).

sample is divided into four equally sized bins and their medians in SFR and stellar mass are shown (yellow stars). We find that the median bins are on average 0.14 dex above the Shivaei et al. (2015b) main sequence relation, which was defined by the star-forming galaxies observed during the first two years of the MOSDEF survey. When Hβ is not detected for MOSDEF targets, it is most often due to contamination from skylines rather than falling below the detection threshold (Reddy et al. 2015; Shivaei et al. 2015b; Sanders et al. 2018). We use `specline`[3] (Shivaei et al. 2018) to construct stacks of the spectra in four bins of stellar mass for the galaxies in our initial (675 galaxies; large faded red diamonds) and our final (312 galaxies; small filled red diamonds) samples. The stacks from both our initial and final samples are within the intrinsic scatter of the Shivaei et al. (2015b) main sequence relation, therefore, we confirm that our sample is not biased against the dustiest galaxies when Hβ non-detections are excluded.

3.3 Methodology and Measurements

In this section, we outline our procedure for calculating dust-corrected SFRs measured from Hα emission and the UV stellar continuum. Hα and Hβ emission measured from slit spectroscopy (and other observed spectroscopic measurements) do not include information about the regions of the galaxy lying outside of the slit area, as is illustrated in Figure 3.2. Relevant to our sample, the slit-loss corrections applied to the MOSDEF spectroscopic observations assume a certain light profile for the galaxy based on a single filter (see Section 3.2.2). This simple light profile may not be sufficiently accurate for large

[3] `https://github.com/IreneShivaei/specline/`

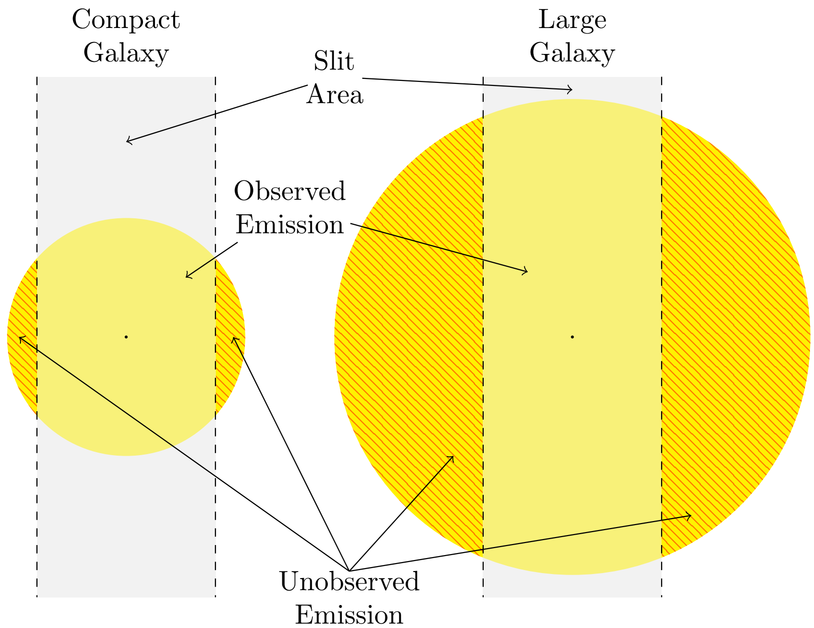

Figure 3.2: Visualization of how the spectroscopic slit covers compact versus large galaxies. The gray region between the dashed vertical lines represents the spectroscopic slit area, which is centered (black dot) on the light distribution of each galaxy (yellow circles) measured from the photometry. Only the emission within the spectroscopic slit area is directly observed, whereas any emission that lies outside of the slit area (red hatched regions) is not directly observed.

galaxies that have a significant fraction of their light falling outside of the slit area or that may have light profiles that vary significantly from band-to-band. Furthermore, the position of the slit is randomly oriented relative to the physical structure of individual galaxies in order to optimize their placement on the mask for multi-object spectroscopy. The UV light, however, is typically measured over a larger area than is covered by the spectroscopic slit, and is determined by the light contained within a circular or isophotal aperture in the imaging. Thus, to make a truly fair comparison between Hα and UV SFRs, we must measure them over the same spatial area, or aperture.

First, we describe the image smoothing and flux measurements that are made over the same spatial resolution and area as the MOSFIRE slit spectroscopy in Section 3.3.1. In Section 3.3.2, we present the SED fitting assumptions and procedure that are used to obtain the both the global and slit-measured stellar population properties, which includes the inferred $E(B-V)_{\rm stars}$. Finally, in Section 3.3.3, we detail our methods for obtaining $E(B-V)_{\rm gas}$, Hα SFRs, and UV SFRs.

3.3.1 Smoothing to the Lowest Resolution

The seeing of the MOSFIRE observations was typically $\sim$0$''$.7, which is a lower spatial resolution than the FWHM of the *HST* PSF (0$''$.18). Therefore, in order to directly compare measurements made from the resolved imaging with the spectroscopic measurements, we first smooth the *HST* images to match the spatial resolution of the MOSFIRE seeing. The `astropy.convolution` python package (Astropy Collaboration et al. 2013, 2018) is used to convolve the *HST* images with a 2D gaussian kernel with FWHM $\sigma_{\rm kernel} = \sqrt{\sigma^2_{\rm MOSFIRE} - \sigma^2_{\rm HST}}$, where $\sigma_{\rm HST}$ is the FWHM of the *HST* PSF equal to 0$''$.18, and $\sigma_{\rm MOSFIRE}$ is the FWHM of the seeing from the MOSFIRE observations. This smoothing procedure is repeated assuming $\sigma_{\rm MOSFIRE}$ is 0$''$.5–0$''$.9 in 0$''$.1 increments, which covers variations in the seeing during the MOSFIRE observations. The smoothed images that are selected for an individual galaxy depends on the average seeing during the respective MOSFIRE observations ($\sigma_{\rm MOSFIRE}$). RMS maps corresponding to the smoothed *HST* images are constructed by scaling the original RMS maps such that the S/N is preserved in each pixel (Fetherolf et al. 2020, Section 2.3.1).

A segmentation map based on the smoothed images is generated following the same input parameters for Source Extractor (Bertin & Arnouts 1996) as Skelton et al. (2014) and using a noise-equalized J_{125}+JH_{140}+H_{160} smoothed image for source detection. We find that the segmentation maps that are based on the smoothed images are approximately equivalent to the original segmentation map processed by the 3D-HST team. However, 25 galaxies from our sample are undetected in the segmentation map of the smoothed images and, thus, are removed from our sample. The smoothed images that assume a $\sigma_{\rm MOSFIRE}$ that best matches the MOSFIRE seeing from the observations of each galaxy are used to measure fluxes and perform SED fitting (see Section 3.3.2).

Pixels that fall inside the slit area are identified using the source centroid, mask position angle, and slit width. The counts from the smoothed images for the pixels inside the slit are summed and converted to AB magnitude and the magnitude error is determined similarly (except summed in quadrature) from the noise maps. In order to avoid any single photometric point from skewing the SED fit, we restrict the minimum magnitude error to 0.05 mag.

To better constrain the shape of the SED at longer wavelengths, we supplement the resolved CANDELS imaging with unresolved *Spitzer*/IRAC photometry at 3.6 μm, 4.5 μm, 5.8 μm, and 8.0 μm available from the 3D-HST broadband photometry catalog (Skelton et al. 2014). The *Spitzer*/IRAC photometry has been corrected for contamination by neighboring sources using models of the *HST* images that have been PSF-smoothed to the lower resolution IRAC photometry and source pixels were identified from the segmentation maps. In order to include the IRAC photometry with the photometric slit measurements for SED fitting, the total IRAC fluxes from the 3D-HST broadband photometric catalog, $F_{\rm IRAC,tot}$, are normalized using the H_{160} flux measured inside the slit area from the smoothed imaging, $H_{\rm 160,slit}$, as follows:

$$F_{\rm IRAC,slit} = F_{\rm IRAC,tot}\frac{H_{\rm 160,slit}}{H_{\rm 160,tot}}, \tag{3.1}$$

where $H_{\rm 160,tot}$ is the total H_{160} flux measured from the 3D-HST broadband photometry and $F_{\rm IRAC,slit}$ is the resultant normalized IRAC flux. For an in-depth discussion of how this procedure affects the derived stellar population properties, see Fetherolf et al. (2020, Appendix B).

3.3.2 SED Fitting

The broadband and slit-measured photometry are modeled, as follows, to obtain SED-derived $E(B-V)_{\rm stars}$, stellar population ages, SFRs, and stellar masses. First, the contribution of the strongest emission lines measured in the MOSDEF spectroscopy (i.e., Hα, Hβ, [OIII]$\lambda\lambda$4960, 5008, and the [OII]λ3728 doublet) is removed from the broadband photometry. A χ^2 minimization technique is used to select the Bruzual & Charlot (2003) stellar population synthesis model that best fits the photometry assuming a Chabrier (2003) IMF, SMC extinction curve (Fitzpatrick & Massa 1990; Gordon et al. 2003), and sub-solar metallicity ($0.2\,Z_\odot$).[4] Reddening is allowed to vary between $0.0 \le E(B-V)_{\rm stars} \le 0.4$. Only constant SFHs and stellar ages between 50 Myr and the age of the Universe at

[4]An SMC-like or steeper extinction curve paired with sub-solar metallicities has been found to be more appropriate for young, high-redshift galaxies compared to the Calzetti et al. (2000) attenuation curve (Reddy et al. 2018a). However, alternatively assuming the Calzetti et al. (2000) attenuation curve and solar metallicities primarily affects the absolute mass measurements and not their relative order (Reddy et al. 2018a). Therefore, the results presented here do not significantly change if we were to alter the assumed extinction curve.

the redshift of each galaxy are considered.[5] Finally, the measured photometric fluxes are perturbed 100 times by their flux errors to obtain the 1σ SED parameter uncertainties based on the 68 lowest χ^2 perturbed models.

We find 112 galaxies that exhibit SED-derived SFRs that are unphysically larger when measured inside the slit area than across the entire galaxy. We consider the SFRs measured inside the slit to be inaccurate in these cases considering that they are based on significantly fewer and less precise photometric measurements. Fetherolf et al. (2020, Chapter 2) showed that if the photometry does not constrain key features of the SED (e.g., UV slope, Balmer/4000 Å break) either by wavelength coverage or sufficient S/N, then the SED-derived parameters may be biased towards redder $E(B-V)_{\rm stars}$ and younger stellar population ages while stellar masses remain robust. Overestimated reddening and underestimated stellar ages (at constant stellar mass and SFH) can, in turn, lead to underestimated SFRs. We find that all 112 galaxies that exhibit overestimated SED-derived SFRs inside the slit exhibit $E(B-V)_{\rm stars}$ and stellar ages that are both redder and younger than the globally averaged $E(B-V)_{\rm stars}$ and stellar ages inferred from the broadband photometry. Comparatively, the average differences between total and slit-measured $E(B-V)_{\rm stars}$ and log stellar ages for the 312 other galaxies in our sample are only 0.03 mag and 0.09 dex, respectively. Furthermore, 98 of the 112 galaxies with overestimated slit-measured SED SFRs have less than two photometric points with a $S/N \geq 1$ covering the UV slope (1250–2500 Å),[6]

[5] The SFRs of $z \sim 2$ galaxies are best reproduced using either exponentially rising or constant SFHs when the stellar population ages are restricted to being older than the typical dynamical timescale (50 Myr; Reddy et al. 2012). Assuming constant SFHs typically produces stellar population ages that are $\sim$30% younger than those derived from exponentially rising SFHs (Reddy et al. 2012).

[6] There is always at least one filter covering the UV slope, but that filter does not necessarily have a $S/N \geq 1$.

thus indicating that this region of the SED is not well-constrained in these galaxies. For these reasons, we decide to remove from our sample the 112 galaxies that do not have robust constrains on the UV slope.

3.3.3 Nebular $E(B-V)_{\mathbf{gas}}$ and SFR Calculations

The nebular reddening, $E(B-V)_{\rm gas}$, is calculated by using the measured Balmer decrement (Hα/Hβ) of each galaxy and assuming the Cardelli et al. (1989) Galactic extinction curve in the following equation:

$$E(B-V)_{\rm gas} = \frac{2.5}{k({\rm H}\beta) - k({\rm H}\alpha)} \log_{10}\left(\frac{{\rm H}\alpha/{\rm H}\beta}{2.86}\right), \tag{3.2}$$

where $k({\rm H}\alpha)$ and $k({\rm H}\beta)$ are extinction coefficients at Hα and Hβ (2.53 and 3.61, respectively, assuming Cardelli et al. 1989 extinction). Equation 3.2 assumes typical ISM conditions, namely Case B recombination, $T = 10000\,{\rm K}$, and $n_e = 10^2\,{\rm cm}^{-3}$, where galaxies with H$\alpha$/H$\beta$ < 2.86 are assumed to have zero dust extinction (Osterbrock 1989). A dust-corrected Hα luminosity is then obtained using $k({\rm H}\alpha)$ from the Cardelli et al. (1989) Galactic extinction curve and the $E(B-V)_{\rm gas}$ derived in Equation 3.2.[7]

In this study, we are interested in directly comparing the SED-derived (i.e., UV) SFRs with spectroscopic dust-corrected Hα SFRs. Typically, Hα luminosities are converted to SFRs using the Kennicutt (1998) relation. However, the Kennicutt (1998) relation assumes solar metallicities, whereas we assume 20% solar metallicities in the SED fitting (see Section 3.3.2). To ensure that the Hα SFRs are consistent with the assumptions used to

[7]Recently, Reddy et al. (2020, in press) derived the first directly measured high-redshift nebular dust attenuation curve using the full MOSDEF sample and found that its shape is similar to the Cardelli et al. (1989) Galactic extinction curve at rest-frame optical wavelengths.

infer the SED-derived SFRs, we obtain an appropriate Hα luminosity-to-SFR conversion for each galaxy directly from the Bruzual & Charlot (2003) SED model templates. For each individual galaxy, the best-fit stellar population age derived from the broadband photometry is used to select the appropriate SED model template. From the template, the rate of ionizing photons is measured by integrating between $90 \leq \lambda \leq 912$ Å. Then, the conversion from luminosity to SFR is derived from the recombination rate of Hα photons. Typical ISM conditions are again assumed for Case B recombination, $T = 10000$ K, and electron densities equal to $10^2\,\mathrm{cm}^{-3}$ (Osterbrock 1989). Deriving Hα SFRs using the SED model templates results in SFRs that are ~24% (~0.11 dex) lower than those derived using the typically assumed Kennicutt (1998) relation. All Hα SFRs throughout this paper, including the Shivaei et al. (2015b) SFR–M_* relation in Figure 3.1, have been corrected to assume the appropriate luminosity-to-SFR conversion derived here. Finally, the $E(B-V)_{\mathrm{gas}}$ and Hα SFRs are obtained directly within the slit area by reversing the slit-loss corrections applied to Hα and Hβ (see Section 3.2.2) and repeating the aforementioned procedure.

In order to have a consistent definition for UV SFRs in comparison to Hα SFRs in Section 3.4, the UV luminosity-to-SFR conversion is also derived separately for each galaxy. The 1600 Å luminosity is measured from the Bruzual & Charlot (2003) SED model template with the same age as determined for the Hα luminosity-to-SFR conversion and a constant SFH. The UV SFRs are then dust-corrected assuming an SMC extinction curve (Fitzpatrick & Massa 1990; Gordon et al. 2003) and the SED-derived $E(B-V)_{\mathrm{stars}}$. UV SFRs that are derived in this way are on average ~3% lower (~0.012 dex) than the SED-derived SFRs.

3.4 Photometric vs. Spectroscopic Properties

The SFR of a galaxy is a fundamental measure for understanding how galaxies assemble their stellar mass. An important question is whether SFRs measured at different wavelengths agree, as discrepancies may give clues about their sensitivity to star formation on different timescales (Reddy et al. 2012; Price et al. 2014), provide useful information about the IMF and SFH of galaxies (Madau & Dickinson 2014), or reveal how dust is distributed amongst various stellar populations (Boquien et al. 2009, 2015; Hao et al. 2011; Reddy et al. 2015; Katsianis et al. 2017). Alternatively, the assumptions made when correcting spectroscopic observations for light lost outside of the slit area may cause spectroscopic SFR measurements to disagree with photometric ones (Kewley et al. 2005; Richards et al. 2016; Green et al. 2017). In this section, we investigate whether the discrepancy between dust-corrected SFRs measured from Hα emission and the UV stellar continuum persists when assumptions about the aperture are minimized by directly deriving reddening and SFRs within the MOSFIRE spectroscopic slit area.

In Section 3.4.1, we compare the relationship between Hα-to-UV SFR ratios versus Hα SFRs measured globally and exclusively within the spectroscopic slit area. We then discuss the implications of our results relative to aperture effects in Section 3.4.2. Finally, we place our findings in the context of previous work in Section 3.4.3.

3.4.1 Global vs. Slit-measured Hα-to-UV SFR Ratios

In Figure 3.3, the relationship between Hα-to-UV SFR ratios and Hα SFRs for the 312 galaxies in our sample is shown in the case when all SFRs are measured or inferred

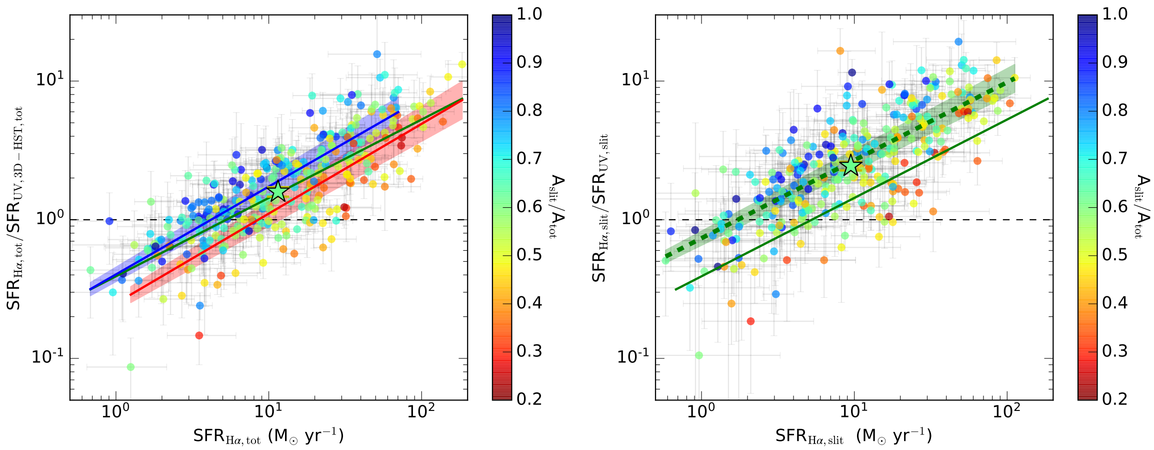

Figure 3.3: *Left:* Total dust-corrected Hα-to-UV SFR ratios versus total dust-corrected Hα SFRs for the 312 galaxies in our sample. The black horizontal dashed line indicates where the Hα SFRs would equal the UV SFRs and the points are colored by the fraction of the galaxy that falls within the slit area (see Figure 3.2). The star symbol shows the median Hα-to-UV SFR ratio, Hα SFR, and fraction of the galaxy within the slit for the full sample. The solid lines show the best-fit relationships for the full sample (green), compact galaxies with slit fractions >0.6 (blue), and large galaxies with slit fractions <0.6 (red). The blue and red shaded regions show the uncertainties in the best-fit relationships of the compact and large galaxies, respectively, thus emphasizing the significance of the offset from the relationship between Hα-to-UV SFR ratios and Hα SFRs being dependent on galaxy size. *Right:* Same as the left panel, except that all of the dust-corrected SFRs (and their respective inferred reddening) are measured exclusively within the spectroscopic slit area. The dashed green line shows the best-fit relationship to the full sample for the slit-measured SFRs and, for reference, the solid green line shows the best-fit relationship to the full sample from the global measurements in the left panel. The green shaded region shows the uncertainty of the slit-measured best-fit relationship for all galaxies, thus emphasizing the significance of the shift in normalization between SFR measurements made exclusively within the slit area (right panel) compared to those made across the entire galaxy (left panel).

over the entire galaxy (left panel) and exclusively within the spectroscopic slit area (right panel). The points are color-coded by the fraction of the galaxy that is covered by the spectroscopic slit. Galaxies where this fraction is close to unity are compact and lie almost entirely within the slit (see Figure 3.2). The median Hα-to-UV SFR ratio, Hα SFR, and fraction of galaxy area covered by the spectroscopic slit for the entire sample is shown by the colored star symbol in each panel. As can be seen by the median Hα-to-UV SFR ratio (star symbols) in Figure 3.3, Hα SFRs are typically higher than UV SFRs (0.22 dex for total and 0.39 dex within the slit). More significantly, Figure 3.3 shows that Hα and UV SFRs tend to generally agree in galaxies with lower Hα SFRs and deviate more significantly as Hα SFR increases, regardless of whether SFRs are measured inside the slit or globally. Additionally, while not shown, Hα and UV SFRs similarly tend to agree at low $E(B-V)_{\rm gas}$, but deviate at high $E(B-V)_{\rm gas}$ to the same significance as is already shown with increasing Hα SFR. The `scipy.odr` package is used to perform orthogonal distance regression linear fits to the relationship between Hα-to-UV SFR ratios and Hα SFRs. The solid and dashed lines in Figure 3.3 show the best-fit linear relationships to the full sample (green), compact galaxies with slit fractions >0.6 (blue), and large galaxies with slit fractions <0.6 (red), where 0.6 is the average slit fraction of all galaxies in our sample. The shaded regions show the 1σ uncertainties for the linear fits of the same color. To show how the relationship changes between the total versus slit measurements, the best-fit relationship to the full sample from the left panel of Figure 3.3 is also shown as a solid green line in the right panel. We find that the slope and scatter between Hα-to-UV SFR ratios and Hα SFRs are approximately the same regardless of how the SFRs are measured (the scatter is 0.22 dex for total and 0.25 dex within the slit).

The primary difference between total (left panel of Figure 3.3) and slit-measured (right panel of Figure 3.3) SFRs is the shift in the normalization of the trend between Hα-to-UV SFR ratios and Hα SFRs (dashed green line in the right panel compared to the solid green line taken from the left panel). Figure 3.4 shows the differences in the positions of the points between the left and right panels of Figure 3.3 (i.e., the slit-measured Hα-to-UV

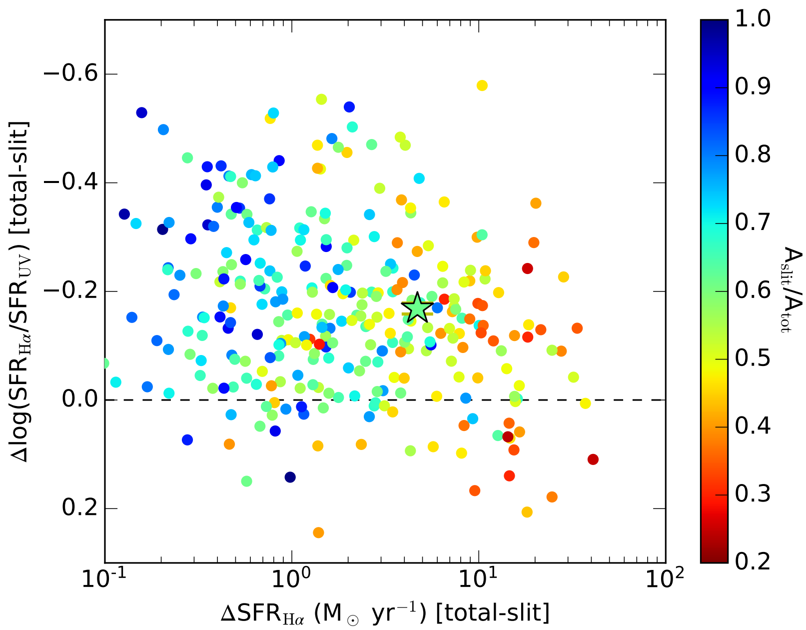

Figure 3.4: The difference between the log of Hα-to-UV SFR ratios measured globally and inside the slit versus the difference between Hα SFRs measured globally and inside the slit. The points are colored by the fraction of the galaxy that is covered by the slit area. The y-axis labels are reversed such that the orientation of the points is relative to the vertical shift in position between the left and right panels of Figure 3.3. The horizontal dashed line shows where the total and slit-measured Hα-to-UV SFR ratios would be equal. The colored star shows the average shift between the points in the left and right panels of Figure 3.3, emphasizing that the galaxies in our sample typically exhibit higher Hα-to-UV SFR ratios when measured exclusively inside the spectroscopic slit area compared to the global average.

SFR ratios and slit-measured Hα SFRs are subtracted from the global measurements). By definition, the Hα and UV light inside the slit area is always lower or equal to those measured across the entire galaxy. If the fraction of Hα and UV light decreased equally between total and slit measurements, then the Hα-to-UV SFR ratio would remain constant. However, Figure 3.4 shows that the Hα-to-UV SFR ratios are on average higher when measured inside the slit compared to those derived using the total SFRs. Therefore, the fraction of Hα light that is "lost" outside of the slit area may not necessarily be proportional to the fraction of UV light that falls outside of the slit area.

The points in Figure 3.3 also show that the offset from the relationship between the Hα-to-UV SFR ratios and Hα SFRs (i.e., the residuals between the points and the best-fit linear relationship) is dependent on the fraction of the galaxy falling within the slit aperture. At a fixed total or slit-measured Hα SFR, large galaxies with a significant fraction of light falling outside of the slit aperture (red points and line in Figure 3.3) exhibit lower Hα-to-UV SFR ratios—and by extension higher total and slit-measured UV SFRs—than compact galaxies (blue points and line in Figure 3.3). Using the Spearman rank correlation test and Figure 3.5, we find that the fractional slit coverage (i.e., size of the galaxy) is significantly correlated with the offset from the relationship between Hα-to-UV SFR ratios and Hα SFRs (green lines in Figure 3.3) at 8σ, regardless of whether all SFRs are measured globally (panel a) or within the slit area (panel b). More specifically, we find that the fractional slit coverage is most significantly correlated with total UV SFRs (13σ, panel c) and slit-measured UV SFRs (12σ, panel d), and slightly less (but still significantly) correlated with total Hα SFRs (8σ, panel e) and slit-measured Hα SFRs (6σ, panel f). Meanwhile, the direct correlation between the fractional slit coverage and the Hα-to-UV SFR ratios is only marginally significant when the SFRs are globally averaged (1σ, panel g) and insignificant when measured within the slit area (0.2σ, panel h). This is because at a constant fractional slit coverage, there is a broad range of measured Hα-to-UV SFRs.

3.4.2 Aperture Effects on Hα-to-UV SFR Ratios

In order to interpret our results from Section 3.4.1, we first need to assess how the geometry between the slit observations and the galaxy orientation influences our results.

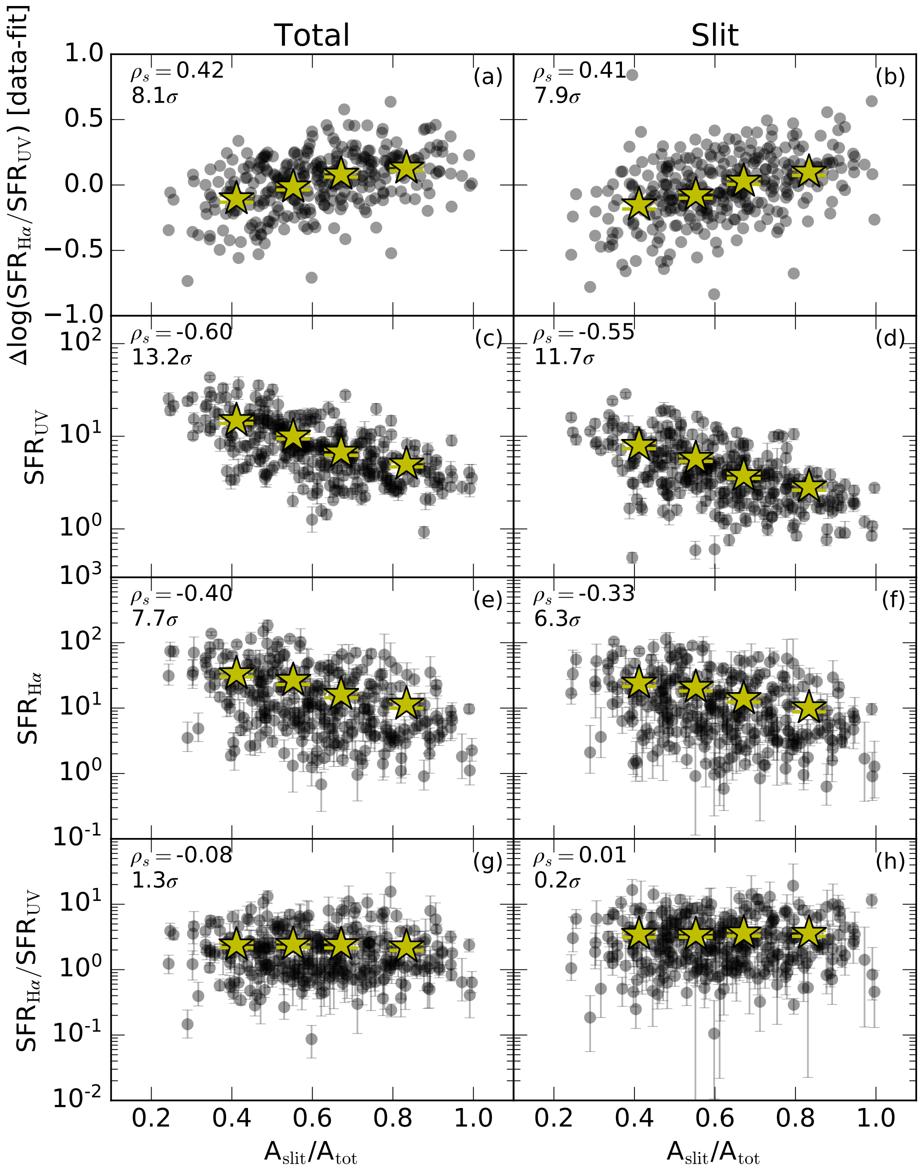

Figure 3.5: Relationships between the fractional slit area (i.e., galaxy size) and the following: the residuals from Figure 3.3 between the Hα-to-UV SFR ratios and best-fit linear relation (green solid and dashed lines in Figure 3.3; panels a and b), UV SFRs (panels c and d), Hα SFRs (panels e and f), and Hα-to-UV SFR ratios (panels g and h). The left and right panel columns show measurements that were made globally and inside the spectroscopic slit area, respectively. The yellow stars are the averages from individual measurements equally divided into four bins of the fractional slit area (A_{slit}/A_{tot}). The Spearman rank correlation coefficient and its significance are listed in the top left corner of each panel.

We consider the fractional slit coverage as a proxy for physical size of the galaxies in our sample since the resolved angular sizes do not change significantly over the redshifts covered by our sample ($1.3 < z < 2.7$). To remind the reader, Figure 3.2 shows the observed and unobserved emission from a compact and large galaxy relative to the spectroscopic slit boundaries. Galaxies that are nearly entirely contained within the slit boundaries (i.e., the compact galaxies) have slit coverage fractions near unity, and thus the spectroscopic measurements of Hα SFRs will be close to those that would be measured globally if such measurements existed.

As can be seen in the right panel of Figure 3.3, the relationship between Hα-to-UV SFR ratios, Hα SFRs, and their sizes (i.e., fraction of each galaxy within the slit area) persists when restricting all quantities to the light that falls inside the slit area and is directly observed. Therefore, the increase in Hα-to-UV SFR ratios with Hα SFRs is not an artifact of the way that Hα is corrected for slit loss. Having said that, in the right panel of Figure 3.3 we also observe a significant shift in the normalization of the relationship between the Hα-to-UV SFR ratios and Hα SFRs when measurements are made directly inside the slit (dashed green line) versus inferred globally (with a slit loss correction for Hα; solid green line). Naturally, the smallest change in normalization occurs for those compact galaxies where a large fraction of the light falls in the slit (blue points), while the largest change in normalization occurs for those galaxies where a smaller fraction of the light falls in the slit (red points). There are three possible scenarios that affect the normalization. 1) If the Hα-to-UV SFR ratio is constant across the entire galaxy, then restricting our measurements only to the light within the slit would result in a lower measured Hα SFRs while the Hα-to-

UV SFR ratios remain constant. This would result in the relationship between Hα-to-UV SFR ratios and Hα SFRs to *simply shift to the left* when only considering the light within the slit. 2) If the Hα-to-UV SFR ratio is lower within the slit versus outside the slit, then restricting our measurements to the slit area would result in lower Hα SFRs and lower Hα-to-UV SFR ratios, thus *shifting their relationship to the left and down.* 3) Lastly, if the Hα-to-UV SFR ratio is higher inside the slit than outside, then restricting our measurements to the light within the slit would result in lower Hα SFRs and higher Hα-to-UV SFR ratios, thus *shifting their relationship to the left and up.*

The relative vertical change in the positions of the points between the left and right panels of Figure 3.3 versus the change between total and slit-measured Hα SFRs (which will always shift to the left) are shown in Figure 3.4. This figure shows that galaxies in general have higher Hα-to-UV SFR ratios inside the slit compared to globally averaged measurements, such that the points shift to the left and up on average when all measurements are made exclusively inside the slit area. Therefore, the shift in normalization between global- and slit-measured SFRs is caused either by the slit-loss corrected total Hα SFRs being underestimated in large galaxies (i.e., assuming that the Hα-to-UV SFR ratio is intrinsically constant) or that Hα-to-UV SFR ratios are intrinsically higher in the centers of large galaxies.

In Figure 3.3, we also find that the deviation from the best-fit relation between Hα-to-UV SFR ratios and Hα SFRs (green lines) is significantly related to the fraction of the galaxy that is directly observed within the spectroscopic slit area. In other words, larger galaxies (i.e., those with a larger fraction of flux falling outside the slit; red points and red line) tend to have higher Hα and UV SFRs (and by extension, higher dust content) and lower Hα-to-UV SFR ratios (relative to the best-fit relation) compared to compact galaxies, such that the contribution from UV light increases more than Hα. While larger galaxies having higher SFRs on average compared to compact galaxies is not particularly surprising (e.g., see Toft et al. 2007; Trujillo et al. 2007; van der Wel et al. 2014; Scott et al. 2017; van de Sande et al. 2018), the relationship between galaxy size and Hα-to-UV SFRs at a constant Hα SFR may be indicative of differences between the Hα and UV light profiles.

3.4.3 Discussion

In Figure 3.3, we found that the relationship between Hα-to-UV SFR ratios and Hα SFRs persists when all reddening and dust-corrected SFRs are made directly inside the spectroscopic slit area. While correcting Hα for light that has been lost outside of the spectroscopic slit area may cause a slight change in the normalization, the general trend between Hα-to-UV SFR ratios and Hα SFRs is not driven by this correction. Reddy et al. (2015) explained their observation of high Hα-to-UV SFRs in galaxies with high Hα SFRs by describing a physical picture where stars of all masses are evenly obscured by low amounts of dust in galaxies with low SFRs, but galaxies that are overall dustier with high SFRs may have patchier dust distributions. Our dust-corrected SFR measurements (both Hα and UV) assume a constant reddening across the entire galaxy, such that if any sightlines are less obscured, particularly towards massive O and B stars that have left their birth clouds, then the average assumed reddening would be overestimated and, in turn, the dust-corrected SFRs would be also be overestimated.

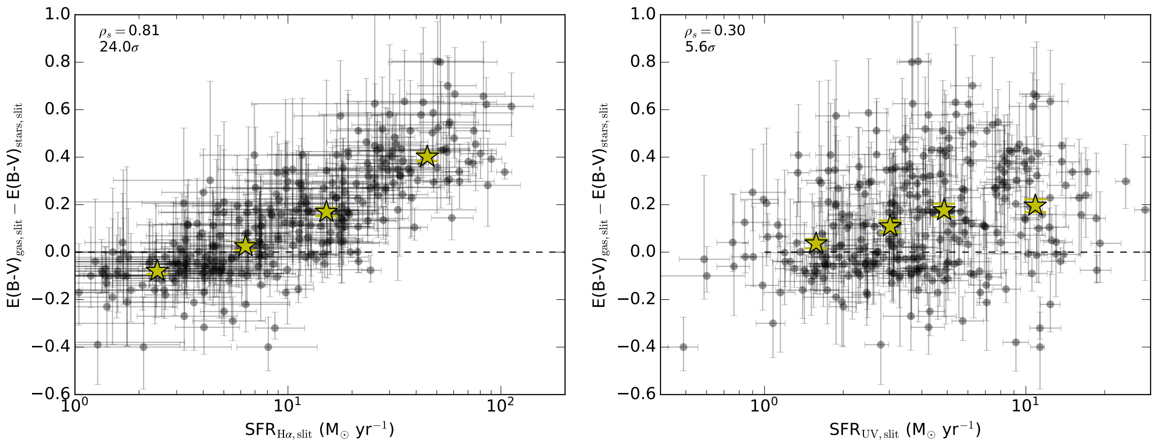

Figure 3.6: Differences between nebular and stellar continuum $E(B-V)$ versus Hα SFRs (*left*) and UV SFRs (*right*), all exclusively measured within the spectroscopic slit area. The yellow stars are the averages from individual measurements equally divided into four bins of Hα SFR. The Spearman rank correlation coefficient and its significance are listed in the top left corner.

Several studies have also found differences between nebular and stellar continuum reddening that vary with SFR (Yoshikawa et al. 2010; Kreckel et al. 2013; Reddy et al. 2015), specific SFR (Wild et al. 2011; Price et al. 2014; Boquien et al. 2015; Reddy et al. 2015; Hemmati et al. 2015), SFR surface density (Boquien et al. 2015), and metallicity (Shivaei et al. 2020), which could similarly be explained by a patchy dust distribution. In Figure 3.6, we show that the observed differences between $E(B-V)_{\rm gas}$ and $E(B-V)_{\rm stars}$ persist in galaxies with higher Hα (left panel; 24σ significance) and UV SFRs (right panel; 6σ significance), even when all measurements are made exclusively within the spectroscopic slit area. The increasing difference between nebular and stellar continuum $E(B-V)$ with Hα SFR may imply that the dust distribution is patchier in galaxies with higher SFRs (that are also inherently dustier; Calzetti et al. 1994; Boquien et al. 2009; Price et al. 2014; Reddy et al. 2015), such that the nebular emission becomes dominated by the most obscured massive stars. However, we should note that $E(B-V)_{\rm gas}$ and $E(B-V)_{\rm stars}$ are used to correct Hα and UV SFRs, respectively, for the effects of dust, and thus the observed trend between $E(B-V)$ difference and SFR may be exagerated. Furthermore, Shivaei et al. (2020) recently found that the relationship between the differences in $E(B-V)$ and SFR (both Hα and UV) for $z \sim 2$ star-forming galaxies in the MOSDEF sample is significantly reduced when the UV light is corrected using a metallicity dependent dust attenuation curve. Therefore, understanding the nature between different reddening and SFR indicators would be best addressed using an independent SFR indicator, such as SFRs measured from the far-IR continuum.

In Figure 3.4, we found that directly measuring all SFRs inside the slit area resulted in lower Hα SFRs (as expected) and higher Hα-to-UV SFR ratios compared to globally averaged measurements. If Hα-to-UV SFR ratios are assumed to be intrinsically constant across the entire galaxy, then this normalization shift in the relationship between Hα-to-UV SFR ratios and Hα SFRs may be attributed to inadequate slit-loss corrections. However, the observed shift in normalization could alternatively be caused by large galaxies having intrinsically high Hα-to-UV SFR ratios in their centers. Centrally peaked Hα and Balmer decrement radial profiles have been observed in galaxies at $1 < z < 3$ using resolved emission line maps (e.g., Nelson et al. 2013; Hemmati et al. 2015; Tacchella et al. 2018) and have even been observed to be more strongly peaked in massive galaxies (Nelson et al. 2016), which are well-known to be larger, dustier, and have higher SFRs than low-mass galaxies on average (e.g., see Shapley 2011). In the case of slit-loss corrected SFRs (left panel of Figure 3.3), a centrally peaked Hα SFR radial profile can cause over or underestimated SFRs if the Hα emission does not follow the H_{160} light profile—as is assumed when correcting for light lost outside of the slit (see Section 3.2.2). In the MOSDEF survey, we can only observe a small fraction of the surface area of large galaxies spectroscopically (see Figure 3.2), and it is possible that these large galaxies have higher Hα SFRs in their centers compared to their unobserved outskirts. Similarly, if Balmer decrements are typically higher in the centers of large galaxies compared to their outskirts, then the assumed average reddening based on the slit measurement will overestimate the true globally-averaged reddening.

Overall, a patchy dust distribution and centrally peaked Hα SFRs and/or Balmer decrements in large galaxies could explain all of our observations. A patchy dust distribution in galaxies with high SFRs could cause some sightlines towards recently formed massive stars to be less obscured than those still enshrouded by their birth clouds, which may lead to overestimated reddening estimates and, inevitably, could explain the observed discrepancies between inferred $E(B-V)$ and dust-corrected SFRs. The Hα and UV light profiles may not match at all radii in large galaxies, which could be caused by either patchy dust distributions or centrally peaked Hα SFRs and/or Balmer decrements. Inappropriate assumptions about the shape of the Hα and UV light profiles relative to each other could explain the higher Hα-to-UV SFR ratios that are observed inside the slit compared to global measurements and the correlation between the size of a galaxy and its observed offset from the relationship between Hα-to-UV SFR ratios and Hα SFRs. We will further explore the distribution of dust and its relationship to globally measured properties of the $z \sim 2$ MOSDEF galaxies in a future work (Fetherolf et al. 2020c, in prep.; Chapter 4) by performing an in-depth analysis of the reddening maps created through the procedures described in Fetherolf et al. (2020, Chapter 2).

3.5 Summary

In this study, we used a sample of 312 star-forming galaxies drawn from the MOSDEF survey at spectroscopic redshifts $1.36 < z < 2.66$ to directly compare dust-corrected SFRs measured from Hα emission and the UV continuum light. We used the CANDELS/3D-HST high-resolution, multi-band imaging to measure the stellar population and dust properties both globally and within the MOSFIRE slit region. By combining the slit-measured stellar population and dust properties from the resolved imaging with the MOSDEF Hα and Hβ emission line measurements, we were able to directly obtain measurements of nebular $E(B-V)_{\rm gas}$, stellar continuum $E(B-V)_{\rm stars}$, Hα SFRs, and UV SFRs exclusively inside the MOSFIRE spectroscopic slit area.

In order to directly compare photometric and spectroscopic measurements over the same area, we PSF-smoothed the *HST* imaging to match the spatial resolution (i.e., seeing) of the MOSFIRE spectroscopic observations (Section 3.3.1). By directly comparing SFR measurements within the spectroscopic slit area, we found that *aperture corrections alone cannot explain the observed differences between Hα and UV SFRs* that are most discrepant in galaxies with high Hα SFRs and $E(B-V)_{\rm gas}$ (Figure 3.3). Furthermore, we found that the shift in the normalization of the relationship between Hα-to-UV SFR ratios and Hα SFRs may indicate that Hα-to-UV SFR ratios are higher in the centers of large galaxies (Figure 3.4), and that the offset from the best-fit linear relationship is dependent on the fraction of the galaxy that is observed within the spectroscopic slit area (i.e., physical size; Figure 3.3 and panels a and b in Figure 3.5).

To explain the observations presented in Section 3.4, we reiterate the physical scenario depicted by Reddy et al. (2015) where the dust distribution gets patchier as a function of increasing SFR. In this scenario the optical depth is on average higher in high-SFR galaxies, but the emitted light is dominated by young, massive stellar populations that may be less obscured than what is implied by the average measured reddening—thus leading to the discrepancy between Hα and UV SFRs. Furthermore, large galaxies with higher SFRs may exhibit centrally peaked Hα or Balmer decrement profiles, such that the relative Hα and UV light are not necessarily equivalent at all radii.

Due to the nature of the MOSFIRE spectrograph, we can only draw direct conclusions based on the observations that fall within the slit area. Even with our limited spectroscopic capabilities, we see evidence that the observed discrepancies in $E(B-V)$ and SFRs measured from the nebular emission and the stellar continuum are caused by some physical driver—such as centrally peaked or patchy dust distributions—rather than systematic errors in the aperture corrections. These results can be improved upon with independent confirmation of the slit-loss corrections through IFU observations, high spatial resolution spectroscopy that could be used to compare Hα and UV emission on smaller scales and out to larger radii, and pairing this analysis with a third independent SFR indicator (e.g., measured from the far-IR continuum). In direct follow-up to this work, we will investigate how the distribution of dust influences observed SFRs and other globally measured physical properties of high-redshift galaxies.

Chapter 4

Paper III: Probing Resolved Stellar Populations at $z \sim 2$ Using a New Bayesian-defined Morphology Metric Called Patchiness[1]

Abstract We investigate the inferred distribution of dust in the interstellar medium of 310 star-forming galaxies at spectroscopic redshifts $1.36 < z < 2.66$. Stellar population and robust reddening maps are constructed using high-resolution multi-waveband CANDELS/3D-HST imaging and spectroscopic redshifts from the MOSFIRE Deep Evolution Field (MOS-

[1]This chapter contains a draft of an article that will be submitted for publication by Oxford University Press in the Monthly Notices of the Royal Astronomical Society written by Tara Fetherolf, Naveen A. Reddy, Alice E. Shapley, Mariska Kriek, Brian Siana, Alison L. Coil, Bahram Mobasher, William R. Freeman, Ryan L. Sanders, Sedona H. Price, Irene Shivaei, Mojegan Azadi, Francesca M. Fornasini, Laura de Groot, Gene C.K. Leung, and Tom O. Zick.

DEF) survey. The stellar continuum reddening distribution is quantified using the Gini and M_{20} coefficients alongside a newly defined morphology metric called "patchiness" (P). The patchiness metric is sensitive to deviations from the average of a resolved distribution, does not require the galaxy center to be defined, and can be used on any resolved distribution. We find that the stellar continuum reddening distribution of high-mass and high-metallicity galaxies is patchier and exhibits lower Gini coefficients than low-mass galaxies. While several previous studies have suggested that patchy dust distributions could explain observed differences between nebular and stellar continuum reddening, SFR indicators, and dust attenuation curves, this study presents early evidence for patchy dust distributions in high-redshift galaxies. Our results support a picture where dust is smoothly distributed in low-mass galaxies, suggesting efficient mixing of dust throughout their interstellar medium. On the other hand, the dust distribution is patchier in high-mass galaxies, such that dust is concentrated near regions of active star-formation and dust mixing timescales are expected to be longer.

4.1 Introduction

Galaxy morphology—or the observed structure of galaxies based on the distribution of their stars, gas, and dust—is an important tool for understanding how galaxies assemble across cosmic time. The morphology of a galaxy can most fundamentally be classified based on its visual structure, such as identifying where a galaxy falls on the well-known "Hubble sequence" (Hubble 1926; de Vaucouleurs 1959). While the classification of galaxies has significantly advanced by crowd sourcing volunteers for visual classification (i.e., Galaxy

Zoo; Lintott et al. 2008, 2011) and developing machine learning algorithms to train computers (e.g., Banerji et al. 2010; Dieleman et al. 2015; Domínguez Sánchez et al. 2018), the disk-, bulge-, and bar-like structures used in visual classifications are not typically observed in high-redshift galaxies, which instead appear clumpy and irregular in shape (e.g., Griffiths et al. 1994; Dickinson 2000; van den Bergh 2002; Papovich et al. 2005; Shapley 2011; Conselice 2014). However, studying the morphology of irregularly shaped high-redshift galaxies, especially at $z \sim 2$ when galaxies were rapidly assembling their stellar mass (see Madau & Dickinson 2014), is a critical step in understanding their evolution.

There are also quantitative morphology metrics that are dependent on the distribution of light from the one- or two-color images rather than visually defined structures, such as the Sérsic index (Sérsic 1963), bulge-to-disk light ratio (i.e., GALFIT; Peng et al. 2002, 2010), CAS parameters (i.e., concentration, asymmetry, and clumpiness; Conselice 2003), Gini coefficient (Abraham et al. 2003; Lotz et al. 2004), second-order moment of light (i.e., M_{20}; Lotz et al. 2004, 2008), internal color dispersion (ICD; Papovich et al. 2005), and MID statistics (multimode, intensity, and deviation; Freeman et al. 2013). Quantitative metrics may be more appropriate for defining the morphology of high-redshift galaxies, but several of these metrics still require a well-defined center for the galaxy, which is not easy to define for clumpy, irregularly shaped galaxies. Furthermore, since these metrics are designed to be used on one- or two-color resolved images, they are not necessarily suitable for probing the distribution of resolved physical properties in galaxies that are inferred from their multi-wavelength photometry.

The distribution of stellar mass and sites of recent star formation can be used to investigate the assembly history of galaxies (e.g., Wuyts et al. 2012; Hemmati et al. 2014; Boada et al. 2015), the rate and efficiency with which gas is converted into stars (e.g., Lang et al. 2014; Jung et al. 2017; Tacchella et al. 2018), and a galaxy's merger history (e.g., Conselice 2003; Lotz et al. 2004, 2008; Cibinel et al. 2015). Revealing the intrinsic properties of stellar populations within galaxies requires a correction for the obscuring effects of dust, which depends on the physical properties of the dust grains, the total amount of dust, and its distribution relative to the stars (e.g., Draine & Lee 1984; Fitzpatrick & Massa 1986; Calzetti et al. 1994; Charlot & Fall 2000). Patchy or clumpy dust distributions have been theorized as the cause behind observed variations in different probes reddening (e.g., Calzetti et al. 1994; Wild et al. 2011; Price et al. 2014; Reddy et al. 2015, 2018b, 2020, in prep.) and SFRs (e.g., Boquien et al. 2009, 2015; Hao et al. 2011; Reddy et al. 2015; Katsianis et al. 2017, Fetherolf et al. 2020b, in prep.; Chapter 3), and recently Shivaei et al. (2020) suggested that patchy dust distributions could also explain variations in the slope and shape of the attenuation curve with metallicity.

In this study, we investigate the inferred the distribution of dust in the interstellar medium (ISM) of high-redshift galaxies based on their resolved stellar continuum reddening maps ($E(B-V)_{\rm stars}$). To achieve this goal, we derive a new morphology metric, called "patchiness," that is sensitive to the deviations that are both above and below the average of a resolved distribution and can be used to probe *any* resolved distribution, including one-color imaging, stellar population and reddening maps, or spatially resolved emission line measurements. Resolved stellar population and robust reddening maps are constructed using the high-resolution multi-waveband imaging from the Cosmic Assembly Near-infrared Deep Extragalctic Legacy Survey (CANDELS; Grogin et al. 2011; Koekemoer et al. 2011). We also use spectroscopic redshifts and emission line measurements from the MOSFIRE Deep Evolution Field (MOSDEF; Kriek et al. 2015) survey to mitigate degeneracies in the resolved SED-fitting and derive global nebular reddening ($E(B-V)_{\rm gas}$) and gas-phase metallicities. The MOSDEF survey obtained rest-frame optical spectra for ~1500 star-forming and AGN galaxies that also have been observed through CANDELS and the 3D-HST grism survey (Brammer et al. 2012; Skelton et al. 2014). The legacy of these data is such that we can probe how the distribution of dust in the ISM evolves with globally measured properties for a statistically large sample of 310 galaxies at $1.36 < z < 2.66$.

The data and sample selection are introduced and the methodology for constructing resolved stellar population and robust reddening maps is outlined in Section 4.2. The new morphology metric, deemed "patchiness," is defined in Section 4.3 alongside the Gini and M_{20} coefficients that are additionally used to probe the distribution of resolved stellar continuum reddening. Our results are presented in Section 4.4 with a discussion of how the ISM of high-redshift galaxies evolves with stellar mass. Finally, we summarize our findings in Section 4.5.

A cosmology that assumes $H_0 = 70\,{\rm km\,s^{-1}\,Mpc^{-1}}$, $\Omega_\Lambda = 0.7$, and $\Omega_m = 0.3$ is used throughout this work. The vacuum wavelengths of emission lines are used and magnitudes are presented in the AB system (Oke & Gunn 1983).

4.2 Data, Sample Selection, and Stellar Population and Reddening Maps

In this section, we present the data, sample selection, and methodology for creating resolved stellar population and reddening maps. We introduce the CANDELS resolved imaging and 3D-HST photometric catalogs in Section 4.2.1. An overview of the MOSDEF survey is presented in Section 4.2.2 and the sample selection is defined in Section 4.2.3. In Section 4.2.4, we outline our methods for processing the resolved photometry and finally our SED fitting assumptions are listed in Section 4.2.5.

4.2.1 CANDELS/3D-HST Photometry

We use *HST*/ACS resolved imaging in the F435W, F606W, F775W, F813W, and F850LP filters (B_{435}, V_{606}, i_{775}, I_{814}, and z_{850}) and *HST*/WFC3 resolved imaging in the F125W, F140W, and F160W filters (J_{125}, JH_{140}, and H_{160}) that has been obtained by CANDELS (Grogin et al. 2011; Koekemoer et al. 2011). CANDELS imaging covers $\sim$900 arcmin^2 of five well-studied extragalactic fields (AEGIS, COSMOS, GOODS-N, GOODS-S, and UDS) to a 90% completeness at $\sim$25 mag in the H_{160} filter. We use the reprocessed CANDELS imaging that has been made publicly available[2] by the 3D-HST grism survey team (Brammer et al. 2012; Skelton et al. 2014; Momcheva et al. 2016). The reprocessed *HST* images have been drizzled to a $0''.06$ pixel^{-1} scale and spatially smoothed to the $0''.18$ resolution of the H_{160} images. We also utilize the 3D-HST broadband catalog that includes

[2] https://3dhst.research.yale.edu/

ancillary ground- and space-based photometry at 0.3 to 0.8 μm covering the CANDELS extragalactic fields. The 3D-HST v4.0 catalog galaxy IDs are used throughout this paper.

4.2.2 MOSDEF Spectroscopy

We use spectroscopic redshifts and emission line measurements from the MOSDEF survey (Kriek et al. 2015). The MOSDEF survey obtained rest-frame optical spectra for $\sim$1500 star-forming galaxies and AGN using observations with the MOSFIRE multi-object spectrograph (McLean et al. 2010, 2012) on the 10 m Keck I telescope in the Y, J, H, and K bands ($R = 3400$, 3000, 3650, and 3600 using $0''.7$ slit widths). Targets for the MOSDEF survey were selected from the five CANDELS extragalactic fields to an H_{160}-band limit of 24.0, 24.5, and 25.0 mag to correspond with a with a stellar mass limit of $\sim 10^9\,M_\odot$ in the following three redshift bins: $1.37 < z < 1.70$, $2.09 < z < 2.61$, and $2.95 < z < 3.80$ (hereafter, the $z \sim 1.5$, $z \sim 2.3$, and $z \sim 3$ samples). These redshift ranges were selected such that several strong rest-frame optical emission lines could be observed in the near-IR windows of atmospheric transmission, including: [OII]$\lambda 3727, 3730$, Hβ, [OIII]$\lambda\lambda 4960, 5008$, H$\alpha$, [NII]$\lambda\lambda 6550, 6585$, and [SII]$\lambda 6718, 6733$. At least one slit star is also included on each slit mask to be used for the absolute flux calibration of the spectra and to correct for slit loss. For more information about the observing strategy and data reduction procedures for the MOSDEF survey, see Kriek et al. (2015).

In order to measure line fluxes, a Gaussian function is fit to each emission line with an underlying linear fit to the continuum. Double and triple Gaussians are fit to the [OII]$\lambda\lambda 3727, 2730$ doublet and Hα+[NII]$\lambda\lambda 6550, 6585$ lines, respectively. Hα and Hβ emission line fluxes are corrected for Balmer absorption using the stellar population model that best fits the observed 3D-HST broadband photometry (see Section 4.2.5). To obtain flux errors, the 1D spectra are perturbed 1000 times by their error spectra, line fluxes are remeasured, and the errors are assumed to be the 68th-percentile width of the distribution. The spectroscopic redshift is determined from the observed wavelength of the highest signal-to-noise (S/N) line (typically Hα or [OIII]λ5008). Refer to Reddy et al. (2015) for more details on the emission line flux measurements for the MOSDEF survey.

4.2.3 Sample Selection

Galaxies with robust spectroscopic redshifts and observations from the MOSDEF survey that covered the Hα and Hβ emission lines are included in the sample. Robust spectroscopic measurements are defined as being measured from at least two strong emission features with a S/N ≥ 2. AGNs are identified and removed from the sample using their X-ray luminosities, optical emission line measurements ($\log([\text{NII}/\text{H}\alpha]) > -0.3$), and and/or mid-IR luminosities (Coil et al. 2015; Azadi et al. 2017, 2018; Leung et al. 2019). These requirements produce an initial sample of 735 galaxies at $1.24 < z < 2.66$. Additional S/N and resolution constraints are applied to the photometry using the multi-filter Voronoi binning technique outlined by Fetherolf et al. (2020, Section 4.2.4), resulting in a final sample of 310 star-forming galaxies at $1.36 < z < 2.66$.

Figure 4.1 shows the spectroscopic redshift distribution, SFR–M_*, and size–M_* relations for the galaxies in the initial (white histogram and empty points) and final samples (gray histogram and filled gray points). The solid green line shows the Shivaei et al. (2015b) main sequence relationship derived from the first two years of data from the MOSDEF

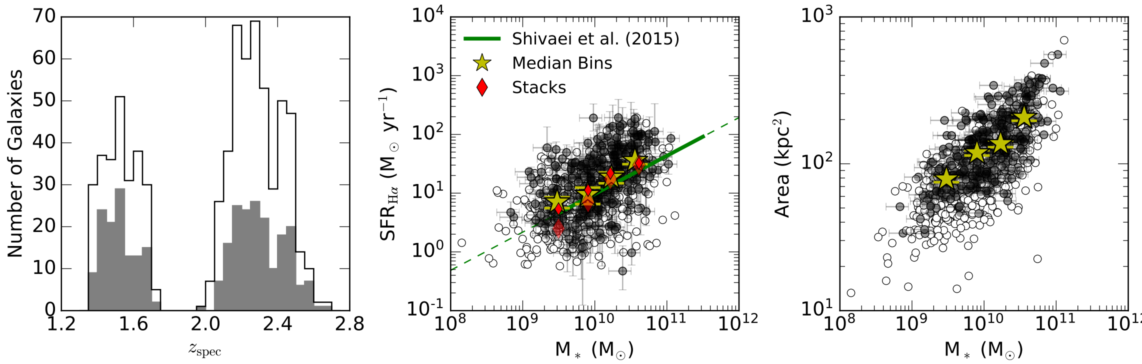

Figure 4.1: *Left:* The spectroscopic redshift distribution of the star-forming galaxies in the sample at $1.24 < z < 1.36$. The white and gray histograms show the initial (735 galaxies) and final (310 galaxies) samples, respectively. *Middle:* The Hα SFR versus stellar mass "main-sequence" relationship. The white empty and gray filled points show the initial and final samples, respectively. Hα emission is corrected for dust using Balmer decrements and assuming the Cardelli et al. (1989) extinction curve, then Hα SFRs are calculated assuming 20% Solar metallicities and a Chabrier (2003) IMF. The Shivaei et al. (2015b) SFR–M_* "main sequence" linear relation that best fit the first two years of MOSDEF data is shown by the green line. Stacks of the spectra in four equal sized bins of stellar mass are shown by the red diamonds, where the stacks from the initial and final samples are shown by the large faded and small solid diamonds, respectively. The yellow stars show the median Hα SFR and M_* of the four bins in stellar mass for the final sample. *Right:* The size versus mass relation for galaxies in the sample, where the area of each galaxy is measured from the detected regions in the 3D-HST segmentation maps. The colors and symbols are the same as in the middle panel, except the yellow stars show the median segmentation map areas in four bins of stellar mass. Compared to the initial sample that represents the broader population of galaxies observed as part of the MOSDEF survey, galaxies in the final sample tend to be marginally biased against low-mass and compact galaxies due to the S/N and resolution requirements enforced in the multi-filter Voronoi binning technique (Fetherolf et al. 2020, Section 2.3.2; also see Section 4.2.4).

survey. The samples are equally divided into four bins of stellar mass and the spectra are stacked using `specline`[3] (Shivaei et al. 2018). The red diamonds show the stacked Hα SFR measurements for the binned initial (large faded diamonds) and final (small solid diamonds) samples and the yellow stars show the median bins of the individual measurements for galaxies in the final sample. The distribution of the outlying empty white points and

[3] https://github.com/IreneShivaei/specline/

the 0.33 dex difference between the stacked points of the lowest mass bin between the two samples suggests that the final sample is marginally biased against low-mass and low-SFR galaxies compared to the galaxies in the initial sample. These galaxies tend to be compact and/or faint such that they do not have sufficient S/N that is necessary for measuring reliable spatially resolved fluxes across several filters, as is required by the multi-filter Voronoi binning technique in Section 4.2.4 (Fetherolf et al. 2020, Section 2.3.2).

4.2.4 Resolved Photometry

The methodology for constructing stellar population and robust reddening maps is briefly outlined here, but we refer the reader to Fetherolf et al. (2020, Chapter 2) for more detail. Individual galaxies in the sample are separated into sub-images that are 80×80 pixels in size, which corresponds to approximately 40×40 kpc at $z \sim 2$. Pixels that are not associated with the central galaxy in each sub-image are masked using the noise equalized $J_{125} + JH_{140} + H_{160}$ Source Extractor (Bertin & Arnouts 1996) segmentation map provided by the 3D-HST survey team (Skelton et al. 2014).

In order to group low S/N pixels and avoid correlated signal between individual pixels, the pixels associated with the galaxy are binned using an adaptive Voronoi binning technique (Cappellari & Copin 2003) that has been modified to incorporate the S/N distribution of multiple resolved filters (Fetherolf et al. 2020, Section 2.3.2). Fetherolf et al. (2020, Section 2.4.3) found that additionally considering the S/N distribution of filters at shorter wavelengths, which are typically lower in S/N compared to the H_{160} filter, resulted in better constrained resolved SEDs compared to using the H_{160} S/N distribution alone. Furthermore, in order to avoid stellar population properties from being biased towards noisier bins with generally low S/N, Voronoi bins are required to satisfy a S/N ≥ 5 in at least 5 resolved filters. Bins that do not satisfy this requirement are deemed as "outskirt" bins and are not included in the analysis.

The counts from the pixels that make up an individual Voronoi bin are summed and converted to an AB magnitude. Magnitude errors are measured similarly, by summing the noise in quadrature from the corresponding RMS maps. A minimum magnitude error of 0.05 mag is adopted to prevent any single photometric point from over-constraining the best-fit resolved SED. The resolved CANDELS photometry is additionally supplemented with unresolved *Spitzer*/IRAC photometry (3.6 μm, 4.5 μm, 5.8 μm, and 8.0 μm; Skelton et al. 2014) that is normalized to the H_{160} flux within each Voronoi bin. Refer to Fetherolf et al. (2020, Appendix C) for an in-depth discussion on how incorporating the *Spitzer*/IRAC photometry in this way affects the derived stellar population properties.

4.2.5 SED Fitting

SED-derived $E(B-V)_{\text{stars}}$, stellar population ages, SFRs, and stellar masses are obtained from both the unresolved 3D-HST broadband photometry and the resolved Voronoi bins for galaxies in the sample. The best-fit Bruzual & Charlot (2003) stellar population synthesis model is determined using a χ^2 minimization technique. A Chabrier (2003) initial mass function (IMF) and constant SFHs are assumed. Stellar ages are permitted to range between 50 Myr and the age of the Universe using the spectroscopic redshift of the galaxy being considered.[4] Sub-solar metallicities (0.2 $Z_\odot$) and an SMC extinction curve (Fitzpatrick

[4] Reddy et al. (2012) found that if stellar ages are restricted to being older than the typical dynamical timescale, then either constant SFHs or exponentially rising SFHs best reproduce the SFRs of $z \sim 2$ galaxies.

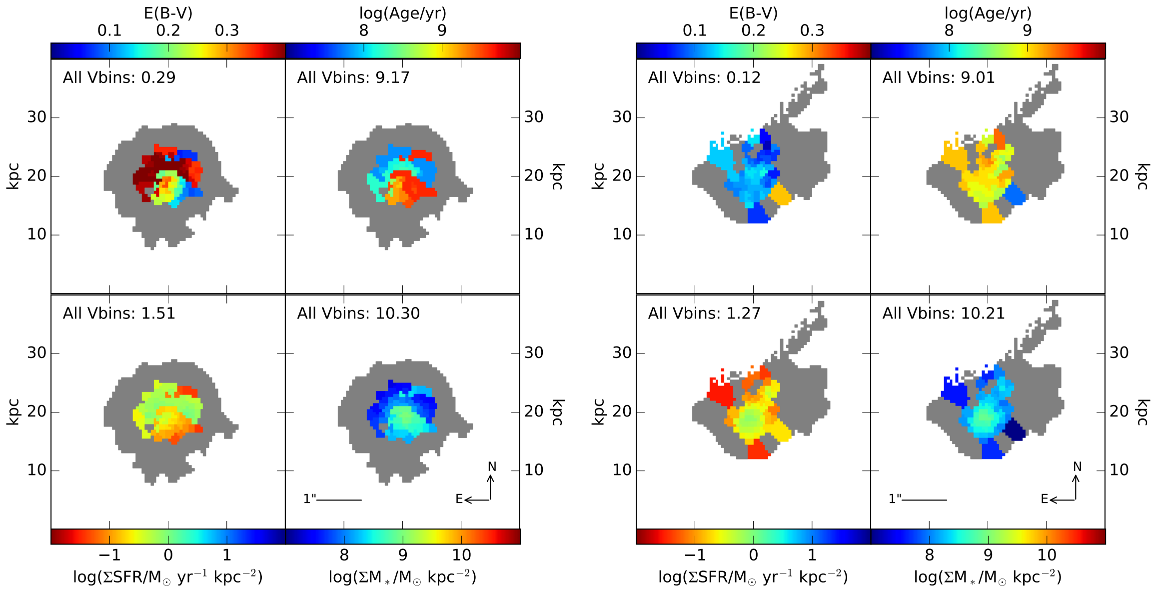

Figure 4.2: Examples of the stellar population and reddening maps for a galaxy in our sample from each redshift bin. The left panels show UDS 25642 ($z = 1.42$) and the right panels show GOODS-N 12345 ($z = 2.27$). The individual panels for a single galaxy show the distribution of $E(B-V)_{\rm stars}$ (*top left*), stellar population age (*top right*), SFR (*bottom left*), and stellar mass (*bottom right*). The average $E(B-V)_{\rm stars}$ and stellar ages weighted by the Voronoi bin areas are shown by the numbers inside the *top row* of panels. The summed SFR and stellar masses from all of the Voronoi bins are shown by the numbers inside the *bottom row* of panels. The gray regions indicate low S/N "outskirt" regions that are not used in the analysis.

& Massa 1990; Gordon et al. 2003) are assumed[5] and reddening is allowed to range between $0.0 \leq E(B-V)_{\rm stars} \leq 0.4$. Examples of the resultant stellar population and reddening maps are shown for UDS 25642 ($z = 1.42$) and GOODS-N 12345 ($z = 2.27$) in Figure 4.2. The number in the top left corner of each panel shows the average $E(B-V)_{\rm stars}$, average stellar population age, summed SFR, and summed stellar mass obtained from the Voronoi

Alternatively assuming exponentially rising SFHs results in stellar population ages that are on average ~30% older than those determined when assuming constant SFHs (Reddy et al. 2012).

[5]While assuming a Calzetti et al. (2000) attenuation curve and solar metallicities may be more appropriate for massive galaxies, only the absolute mass measurements are affected compared to using an SMC extinction curve Fitzpatrick & Massa (1990); Gordon et al. (2003) and sub-solar metallicities (Reddy et al. 2018b). Since the relative order of mass measurements is unaffected, the results presented here would not significantly change if a Calzetti et al. (2000) attenuation curve and solar metallicities were alternatively assumed.

bins. The low S/N "outskirt" components that are not used throughout this analysis are indicated by the gray regions in each panel.

Measuring resolved SED parameter errors is computationally expensive. Therefore, a subset of 50 galaxies that have a range of stellar population parameters that are representative of the larger sample are selected to obtain typical SED parameter errors. The measured unresolved and resolved photometric fluxes are perturbed by their errors and refit 100 times. The 68 models with the lowest χ^2 are used to obtain the 1σ uncertainties in the SED properties derived from the unresolved photometry and individual Voronoi bins. The average SED parameter errors of the Voronoi bins for an individual galaxy are obtained by taking the average of the individual Voronoi bin parameter errors within the galaxy. Finally, the typical resolved SED parameter errors are obtained by taking the average of the parameter errors determined from the 50 galaxies in the subsample. The typical unresolved SED parameter errors are 0.01 in $E(B-V)_{\rm stars}$, 0.20 dex in log stellar population age, 0.05 dex in log SFR, and 0.16 dex in log stellar mass. The typical resolved SED parameter errors based on the individual Voronoi bins are 0.03 in $E(B-V)_{\rm stars}$, 0.21 dex in log stellar population age, 0.16 dex in log SFR, and 0.10 dex in log stellar mass.

4.3 Morphology Metrics

Studying the structure of galaxies at high-redshifts is key towards understanding how galaxies build their stellar mass. Commonly used metrics for quantifying galactic structure include Sérsic surface brightness profiles (Sérsic 1963), light concentration, asymmetry, clumpiness (CAS; Conselice 2003), Gini coefficient, second-order moment of light

(Gini-M_{20}; Abraham et al. 2003; Lotz et al. 2004), and internal color dispersion (ICD; Papovich et al. 2003). All of these measures either require a well-defined centroid, are based on one- to two-color photometry, or focus exclusively on the brightest parts of the light distribution. Alternatively, we aim to quantify structure in a way that is not dependent on a centroid—especially considering that galaxies at progressively higher redshifts have increasingly irregular structure, such that a "center" is not clearly defined (e.g., Griffiths et al. 1994; Dickinson 2000; van den Bergh 2002; Papovich et al. 2005; Shapley 2011; Conselice 2014).

In Section 4.3.1 we introduce "patchiness" (P) as a new morphology metric, which quantifies the dispersion of light (or any resolved property) by being sensitive to both voids and concentrations of light without requiring a defined center. The choice of the Gini (G) and M_{20} coefficients to be used alongside patchiness is explained in Section 4.3.2, alongside their definitions. Finally, the applying the P, G, and M_{20} morphology metrics to the $E(B-V)_{\rm stars}$ distribution is described in Section 4.3.3.

4.3.1 The Patchiness Metric

Patchiness, P, is defined using a Bayesian maximum likelihood technique (for a recent review of Bayes' Theorem, see Sharma 2017) that measures the Gaussian probability that every individual resolved element, X_i, equals the weighted average of the distribution, $\overline{X_{\rm w}}$. We choose to weight the Voronoi bin distribution by the area of individual Voronoi bins,[6] such that the weighted average for a Voronoi bin distribution is defined by

$$\overline{X_{\rm w}} = \frac{\sum_{i=1}^{N_{\rm Vbins}} n_{{\rm pix},i} \; X_i}{\sum_{i=1}^{N_{\rm Vbins}} n_{{\rm pix},i}}, \tag{4.1}$$

where $N_{\rm Vbins}$ is the number of Voroni bins within a single galaxy and $n_{\rm pix}$ is the number of pixels contained within each Voronoi bin. Patchiness is used to quantify the resolved distribution of a single galaxy and is defined by

$$P = -\ln \left\{ \prod_{i=1}^{N_{\rm Vbins}} \frac{1}{\sqrt{2\pi}\sigma_i} \exp\left[-\frac{(X_i - \overline{X_{\rm w}})^2}{2\sigma_i^2} \right] \right\}, \tag{4.2}$$

where X_i is the value of a single resolved element (Voronoi bins, in this case), $\overline{X_{\rm w}}$ is the weighted average of the distribution, and σ_i is the uncertainty of each resolved element. The patchiness metric is defined such that the measured P value will be low when the resolved elements equal the weighted average (high likelihood) and P will be high when there are deviations from the average (low likelihood). For the resolved distributions probed in this study, the range of P spans several orders of magnitude. In order to show $\log P$ in the figures, all calculated P values are shifted such that $P_{\rm min} = 1$.

The patchiness metric is unique from other traditional morphology metrics in that it does not require a defined centroid or radius, it is sensitive to below average outliers in addition to deviations above the mean, and it is insensitive to properties with large dynamic ranges (e.g., stellar mass) or values that approach zero (e.g., $E(B-V)$). Patchiness is most comparable to the ICD (Papovich et al. 2003), which measures the dispersion of light between the resolved imaging obtained in two different filters for a given galaxy. However,

[6] Noisy outskirt bins are not included in this analysis (see Section 4.2.4) and thus do not bias the area-weighted average. Alternatively weighting by either the H_{160} flux or log stellar mass of individual Voronoi bins does not significantly affect our results.

patchiness can be directly applied to any resolved property—including those derived from resolved SED fitting, which incorporates the flux distribution of several photometric bands.

It is important to note that the patchiness metric (and other quantitative metrics) should only be used to compare the relative patchiness of resolved distributions for galaxies that make up a uniformly defined sample. The calculated values of patchiness will vary depending on how the resolved distribution is defined, such as the resolution of the observations and the method for defining which resolved elements are included in the morphology analysis for a single galaxy. An in-depth analysis of the patchiness metric is presented in Appendix C using the resolved SED-derived $E(B-V)_{\rm stars}$, stellar population ages, SFRs, and stellar masses. Our conclusions from Appendix C are summarized briefly as follows. 1) Galaxies that are patchier in one resolved SED-derived property are more likely to be patchier in other resolved SED-derived properties. 2) Patchiness is not biased towards galaxies with more resolved elements by its definition in Equation 4.2, but galaxies with more resolved elements may be intrinsically patchier for some resolved properties (such as stellar mass). 3) The ICD is most significantly correlated with the patchiness of the $E(B-V)_{\rm stars}$ distribution. 4) Measuring the patchiness of a pixel-to-pixel resolved distribution is not recommended due to correlated signal between neighboring pixels and stochastic measurements from pixels with low S/N. 5) The patchiness values of galaxies at different redshifts should be analyzed separately, since patchiness measurements are not conserved after galaxies have been artificially redshifted.

Finally, it is important to emphasize that the morphology of galaxies can be best understood when several morphology metrics are used together. In the present study, we choose to pair patchiness with the Gini and M_{20} coefficients, which are sensitive to the resolved elements with the highest measurements (e.g., brightest or highest mass regions). Morphology metrics that are sensitive to outliers with specific characteristics in a resolved distribution (i.e., high flux or high mass), such as Gini and M_{20}, nicely complement the patchiness metric, which is sensitive to any type of outlier in a resolved distribution.

4.3.2 The Gini Coefficient and the Moment of Light

The Gini coefficient is most well-known from economics, where it is used to measure the distribution of wealth in a population. Abraham et al. (2003) adapted the Gini coefficient to measure the concentration of light within galaxies based on their resolved imaging. After sorting the resolved measurements from lowest to highest flux, the Gini coefficient is calculated by

$$G = \frac{1}{|\overline{X_{\mathrm{w}}}|n(n-1)} \sum_{i=1}^{n} (2i - n - 1)|X_i|, \tag{4.3}$$

where X_i is the flux within an individual resolved element (i.e., Voronoi bin), n is the total number of resolved elements, and $\overline{X_{\mathrm{w}}}$ is the weighted average of the resolved distribution. If all n resolved elements have an equal amount of flux, then $G = 0$. Conversely, if a single resolved element has all of the flux, then $G = 1$. While a high Gini value implies a high concentration of flux, the flux is not necessarily concentrated in a single region since there is no spatial information in the metric.

Lotz et al. (2004) introduced the M_{20} parameter, which is the normalized second-order moment of the 20% brightest regions in a galaxy. The center of the brightest region is defined at $(x_c,\, y_c)$, which is determined by minimizing the total second-order moment.

The total second-order moment, $M_{\rm tot}$ is defined by

$$M_{\rm tot} = \sum_i M_i = \sum_{i=1}^{n} X_i[(x_i - x_c)^2 + (y_i - y_c)^2], \tag{4.4}$$

where (x_i, y_i) is the location of each resolved element and M_i is the flux of each resolved element. The M_i fluxes are then ordered from highest to lowest flux and M_{20} is defined as

$$M_{20} = \log\left(\frac{\sum M_i}{M_{\rm tot}}\right), \text{ while } \sum_i X_i < 0.2 X_{\rm tot}, \tag{4.5}$$

where only the brightest 20% of resolved elements are included. Like the Gini coefficient, M_{20} is also a measure of the concentration of light, but includes spatial information of the brightest regions. Low M_{20} values (typically negative) indicate that the brightest regions are more significantly grouped within a single region of the galaxy. As M_{20} increases (toward zero), the brightest regions tend to be more spatially spread across several clusters of light.

The G and M_{20} coefficients complement each other in that G identifies galaxies where there exists regions of high brightness compared to the average, whereas M_{20} identifies the spatial distribution of the brightest regions. Together, the G and M_{20} coefficients have been used to characterize galaxies within different regions of the G–M_{20} space (Förster Schreiber et al. 2011; Wuyts et al. 2012; Lee et al. 2018), classify galaxies into traditional Hubble types (Lotz et al. 2004, 2008; Boada et al. 2015), and identify merging galaxies (Lotz et al. 2008; Boada et al. 2015). However, a critical assessment of the Gini coefficient by Lisker (2008) found that the Gini coefficient significantly depends on the S/N of resolved elements and the radius used to determine the inclusion of pixels when calculating G, such that G measurements and Gini-defined classification schemes (e.g., Lotz et al. 2008) cannot be directly compared between studies with differing methodologies or sample characteristics. The same can be said for P, which is why we emphasize in Section 4.3.1 that P should only be used to relatively compare the patchiness of resolved distributions for galaxies in uniformly defined samples at similar redshifts (also see Appendix C).

4.3.3 Quantifying the Spatial Distribution of $E(B-V)_{\text{stars}}$

Typically G and M_{20} are used to quantify the concentration of light at a single wavelength (e.g., Lotz et al. 2004, 2008; Förster Schreiber et al. 2011). However, Wuyts et al. (2012) emphasized the importance of studying multi-color morphologies using G and M_{20} by calculating these metrics on the resolved stellar mass distribution for the first time. We further extend the usage of G and M_{20} by quantifying the concentration of reddest Voronoi bins in the resolved reddening maps. In the analysis that follows, we pair the concentration of the reddest regions probed by G and M_{20} with the patchiness, P, of the $E(B-V)_{\text{stars}}$ distribution. The G, M_{20}, and P values are calculated using the equations defined in Section 4.3.1 and Section 4.3.2, where X_i is the $E(B-V)_{\text{stars}}$ of an individual Voronoi bin, $\overline{X_{\text{w}}}$ is the average $E(B-V)_{\text{stars}}$ of the Voronoi bins weighted by their sizes, and σ_i is the uncertainty in the resolved $E(B-V)_{\text{stars}}$ (0.03 mag; see Section 4.2.5). The previously defined "bright" regions are redefined as the reddest regions, or Voronoi bins with the highest $E(B-V)_{\text{stars}}$. Therefore, a high G indicates a concentration of red (high) inferred $E(B-V)_{\text{stars}}$ and a low G suggests a uniform distribution with a constant $E(B-V)_{\text{stars}}$ on average. The spatial continuity of the reddest (highest $E(B-V)_{\text{stars}}$) regions is quantified by M_{20}, where a low M_{20} indicates that the reddest regions tend to be concentrated within a single clump.

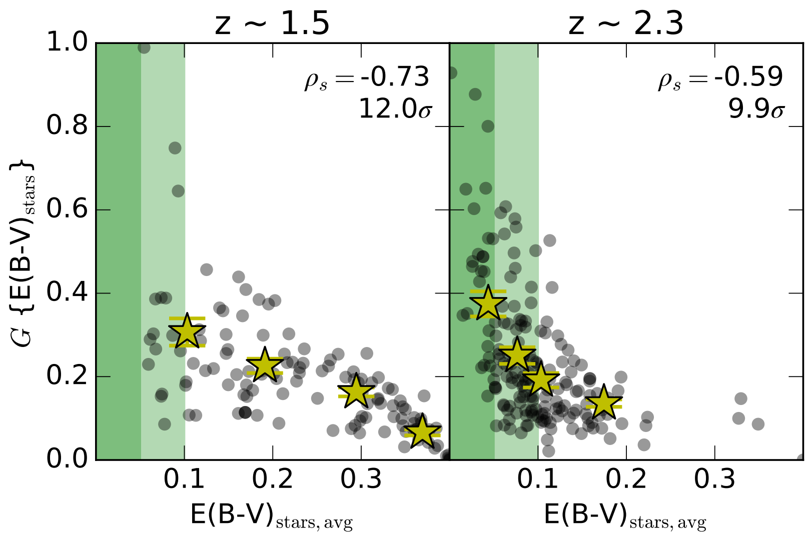

Figure 4.3: Gini of the $E(B-V)_{\rm stars}$ distributions versus average $E(B-V)_{\rm stars}$ for the 126 galaxies in the $z \sim 1.5$ sample (*left*) and 184 galaxies in the $z \sim 2.3$ sample (*right*). The yellow stars show the average G and $E(B-V)_{\rm stars,avg}$ in four bins of $E(B-V)_{\rm stars,avg}$ for the galaxies in each redshift sample. The green shaded regions highlight where the average $E(B-V)_{\rm stars}$ is less than 0.05 and 0.10 mag. The Spearman rank correlation coefficient and its significance is listed in the top right corner of each panel. We observe a wide range of Gini values at low average $E(B-V)_{\rm stars}$, suggesting that the observed correlation is not purely driven by an artificially boosted Gini when the average $E(B-V)_{\rm stars}$ is nearly zero.

A complication when calculating G on the $E(B-V)_{\rm stars}$ distribution is that G may be artificially high or unphysical ($G > 1$) as the average $E(B-V)_{\rm stars}$ approaches zero (consistent with no dust reddening inferred from the best-fit SEDs). Therefore, we raise caution when using G on any resolved distribution where the average could be near zero, such as the $E(B-V)_{\rm stars}$ distribution. The relationship between the average $E(B-V)_{\rm stars}$ ($E(B-V)_{\rm stars,avg}$) and G calculated on the $E(B-V)_{\rm stars}$ distribution for galaxies in the sample is shown in Figure 4.3 and is separated by the two redshift bins. The regions where $E(B-V)_{\rm stars,avg} \leq 0.10$ and $\leq$0.05 mag are shaded in green. While galaxies with low $E(B-V)_{\rm stars,avg}$ tend to have high G, there are also galaxies in the $z \sim 2.3$ sample that have an $E(B-V)_{\rm stars,avg} = 0.02$ mag with $G = 0.35$, such that G is still considered to be representative of the concentration of reddening for galaxies in the sample. On the high $E(B-V)_{\rm stars,avg}$ end, it is important to note that the low G values are caused by the maximum $E(B-V)_{\rm stars}$ of 0.40 mag allowed in the SED models (see Section 4.2.5). Therefore, if the galaxy is very red on average, then the "reddest" regions will not appear as outliers in the resolved distribution. This limitation of G on the resolved $E(B-V)_{\rm stars}$ distribution highlights the importance of pairing G with a morphology metric that is not biased towards extremely high or low values in a resolved distribution—such as the patchiness metric, P.

In the present analysis, we focus on probing the resolved $E(B-V)_{\rm stars}$ distribution using P, G, and M_{20}. However, these morphology metrics can also be applied to the other resolved stellar population properties (i.e., stellar population ages, SFRs, and stellar masses). In Appendix C we briefly highlight using P on the other resolved stellar population maps, but generally defer a broader analysis to future work.

4.4 Dust Reddening Distribution

Our results showing the morphology metrics calculated on $E(B-V)_{\rm stars}$ distribution compared to stellar mass and gas-phase metallicity are shown in Section 4.4.1 and Section 4.4.2, respectively. A physical interpretation for how the dust distribution evolves throughout the ISM of high-redshift galaxies is depicted in in Section 4.4.3. Finally, in Section 4.4.4 our findings are placed into context with other studies.

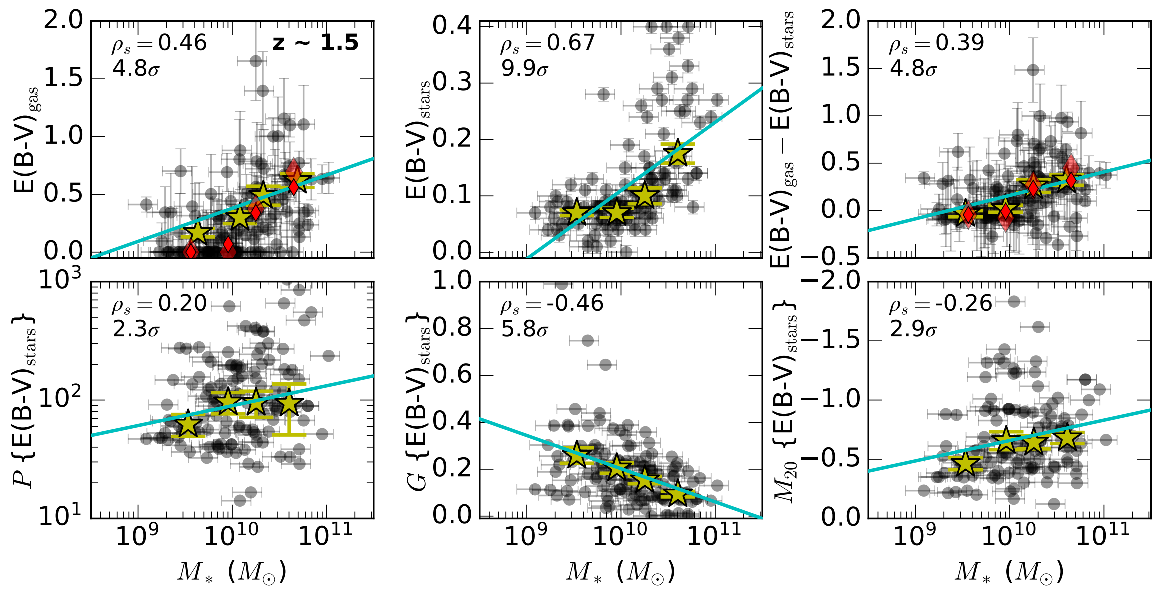

Figure 4.4: Relationships between stellar mass and several probes of dust reddening for the 126 galaxies in the $z \sim 1.5$ sample. *Top row:* Globally averaged $E(B-V)$ derived from the unresolved data. Balmer decrements (Hα/Hβ) measured from the MOSDEF survey are used to calculate $E(B-V)_{\rm gas}$ using Equation 4.6 and assuming a Cardelli et al. (1989) galactic extinction curve. Stacks of the spectra in four equally sized bins of stellar mass are shown by the red diamonds, where the stacks from the initial and final samples are shown by the large faded and small solid diamonds, respectively. The globally averaged $E(B-V)_{\rm stars}$ is inferred from the 3D-HST photometry. The yellow stars show the median y-axis values and median M_* in four equally sized bins of stellar mass. The Spearman rank correlation coefficient and its significance is listed in the top left corner of each panel. The solid light blue lines show the best-fit linear relationships for each panel. *Bottom row:* The P, G, and M_{20} morphology metrics calculated on the $E(B-V)_{\rm stars}$ distribution derived from the resolved SED fitting. Note that the plotted M_{20} values are reversed to be consistent with previous studies (e.g., Lotz et al. 2004, 2008; Boada et al. 2015).

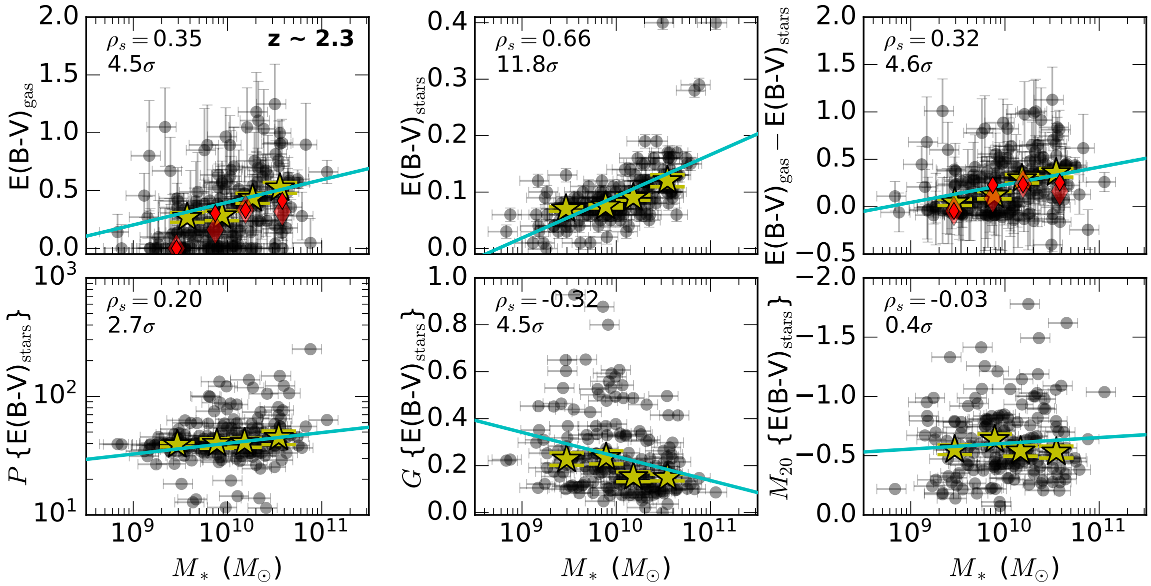

Figure 4.5: Same as Figure 4.4, except showing the relationships between stellar mass and several probes of dust reddening for the 184 galaxies in the $z \sim 2.3$ sample.

4.4.1 $E(B-V)$ vs. Stellar Mass

In addition to using the morphology metrics on the $E(B-V)_{\rm stars}$ distribution, the inferred globally averaged $E(B-V)_{\rm stars}$ and $E(B-V)_{\rm gas}$ are also incorporated into this analysis. The globally averaged $E(B-V)_{\rm stars}$ is derived from the SED that is best-fit to the 3D-HST photometry (see Section 4.2.5). Balmer decrements (Hα/Hβ) measured for each galaxy by the MOSDEF survey are used to calculate the globally averaged $E(B-V)_{\rm gas}$ by

$$E(B-V)_{\rm gas} = \frac{2.5}{k({\rm H}\beta) - k({\rm H}\alpha)} \log_{10}\left(\frac{{\rm H}\alpha/{\rm H}\beta}{2.86}\right), \tag{4.6}$$

where a Cardelli et al. (1989) galactic extinction curve is assumed such that the extinction coefficients are $k({\rm H}\alpha) = 2.53$ and $k({\rm H}\beta) = 3.61$. Typical ISM conditions with Case B recombination are assumed in Equation 4.6 with $T = 10000\,{\rm K}$ and $n_e = 10^2\,{\rm cm}^{-3}$. Zero dust extinction is assumed for galaxies with Hα/H$\beta < 2.86$ (Osterbrock 1989). If Hα or Hβ is not detected with a S/N ≥ 3, then $E(B-V)_{\rm gas}$ is calculated using their 3σ upper limit.

The P, G, and M_{20} morphology metrics calculated on the $E(B-V)_{\rm stars}$ distribution are found to be most significantly correlated with the total stellar masses derived from the 3D-HST photometry. Therefore, Figure 4.4 and Figure 4.5 show all measures of $E(B-V)$ versus stellar mass for the $z \sim 1.5$ and $z \sim 2.3$ samples, respectively. The top panels show the unresolved globally averaged $E(B-V)_{\rm gas}$, $E(B-V)_{\rm stars}$, and difference between $E(B-V)_{\rm gas}$ and $E(B-V)_{\rm stars}$ versus stellar mass. The bottom panels show the P, G, and M_{20} morphology metrics calculated on the $E(B-V)_{\rm stars}$ distribution versus stellar mass. Stacked measurements of $E(B-V)_{\rm gas}$ in four equally sized bins of stellar mass from the initial (large faded diamonds) and final (small solid diamonds) samples are also shown (see Section 4.2.3). Each panel also shows a linear regression fit that is obtained using the `scipy.odr` package, the Spearman rank correlation coefficient (ρ_s), and its significance. For reference, examples of the reddening maps for the lowest and highest mass galaxies in the $z \sim 1.5$ and $z \sim 2.3$ samples are shown in Figure 4.6 with the log stellar mass of each galaxy listed in the bottom right corner of each panel.

In agreement with previous studies, Figure 4.4 and Figure 4.5 show that $E(B-V)_{\rm gas}$, $E(B-V)_{\rm stars}$, and the difference between $E(B-V)_{\rm gas}$ and $E(B-V)_{\rm stars}$ are significantly correlated with stellar mass (e.g., Yoshikawa et al. 2010; Price et al. 2014; Hemmati et al. 2015; Reddy et al. 2015; Nelson et al. 2016; Tacchella et al. 2018). The relationship between P and stellar mass shows that low-mass galaxies tend to have smoother $E(B-V)_{\rm stars}$ distributions, with increasing dispersion in P and generally patchier dust reddening distributions as galaxies increase in stellar mass. The G of the $E(B-V)_{\rm stars}$ distribution is inversely proportional with stellar mass, such that low-mass galaxies have higher concentrations of the reddest regions (see Figure 4.3) compared to high-mass galaxies. Finally, the high-mass galaxies in the $z \sim 1.5$ sample tend to have lower M_{20} values than low-mass $z \sim 1.5$ galaxies, indicating that the reddest regions are generally concentrated within a single region in high-mass galaxies. There is no correlation observed between M_{20} and stellar mass for the $z \sim 2.3$ sample.

4.4.2 $E(B-V)$ vs. Metallicity

In Section 4.4.1, we found that the P, G, and M_{20} morphology metrics calculated from the reddening maps varied most significantly with stellar mass. Since there exists a well-known relationship between stellar mass and metallicity (MZR; e.g., Tremonti et al. 2004; Erb et al. 2006b; Kewley & Ellison 2008; Mannucci et al. 2010; Andrews & Martini 2013; Sanders et al. 2015), it is reasonable to expect that these morphology metrics probing the $E(B-V)_{\rm stars}$ distribution may similarly correlate with metallicity. Furthermore, the gas-phase metallicity is considered a proxy for small dust grains in the ISM (Dwek 1998; Jenkins 2009) and Shivaei et al. (2017) recently showed that dust emission from polycyclic aromatic hydrocarbon (PAH) molecules is significantly correlated with metallicity. Therefore, in this section we show how P, G, and M_{20} calculated on the $E(B-V)_{\rm stars}$ distribution varies as a function of gas-phase metallicity.

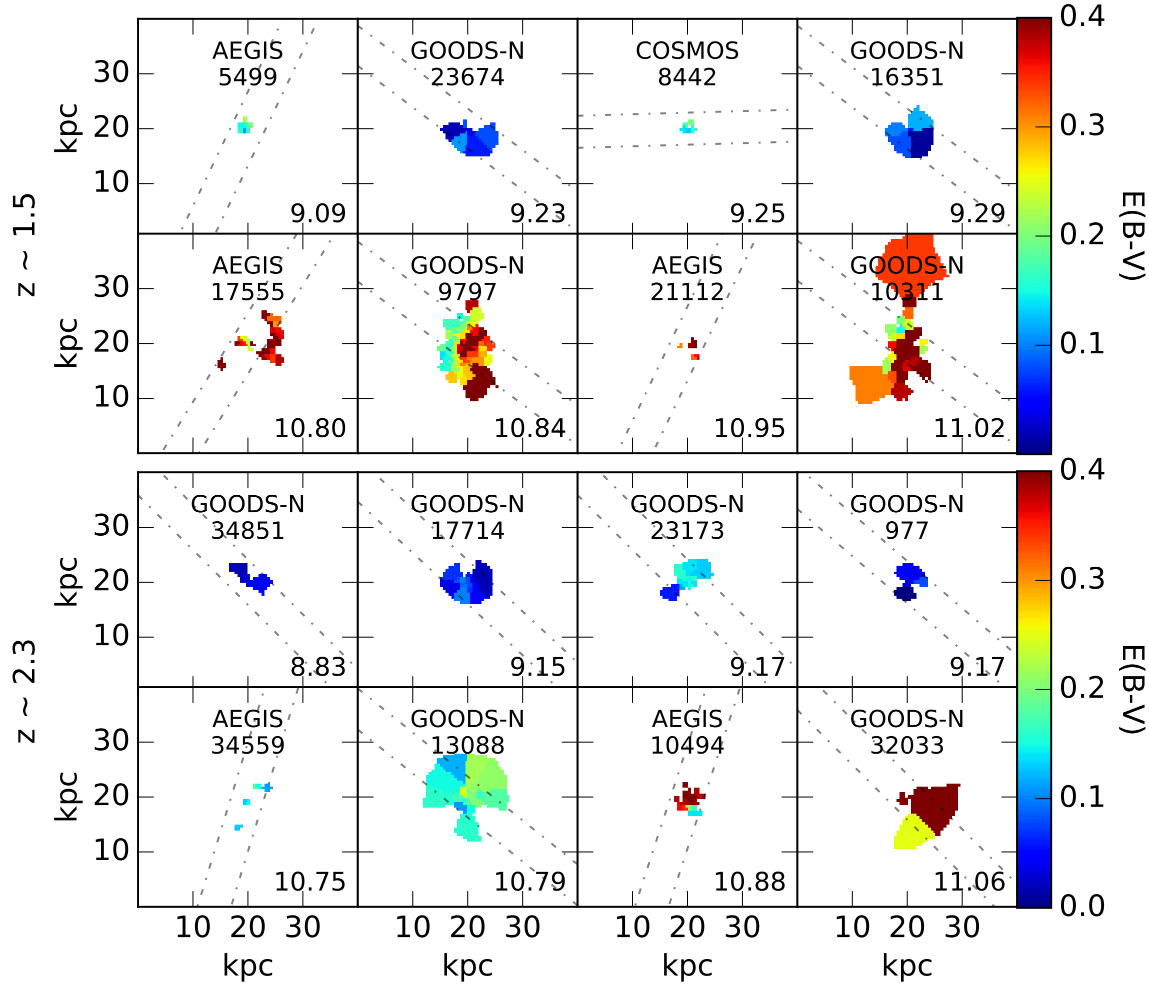

Figure 4.6: Examples of the $E(B-V)_{\rm stars}$ maps for galaxies in the $z \sim 1.5$ (*top*) and $z \sim 2.3$ (*bottom*) samples. The top and bottom rows show the galaxies with the lowest and highest masses in each redshift sample, respectively. The $\log(M_*/M_\odot)$ of each galaxy is shown in the bottom right corner of each panel. The dash-dotted gray lines show the placement of the spectroscopic slit from the MOSDEF observations.

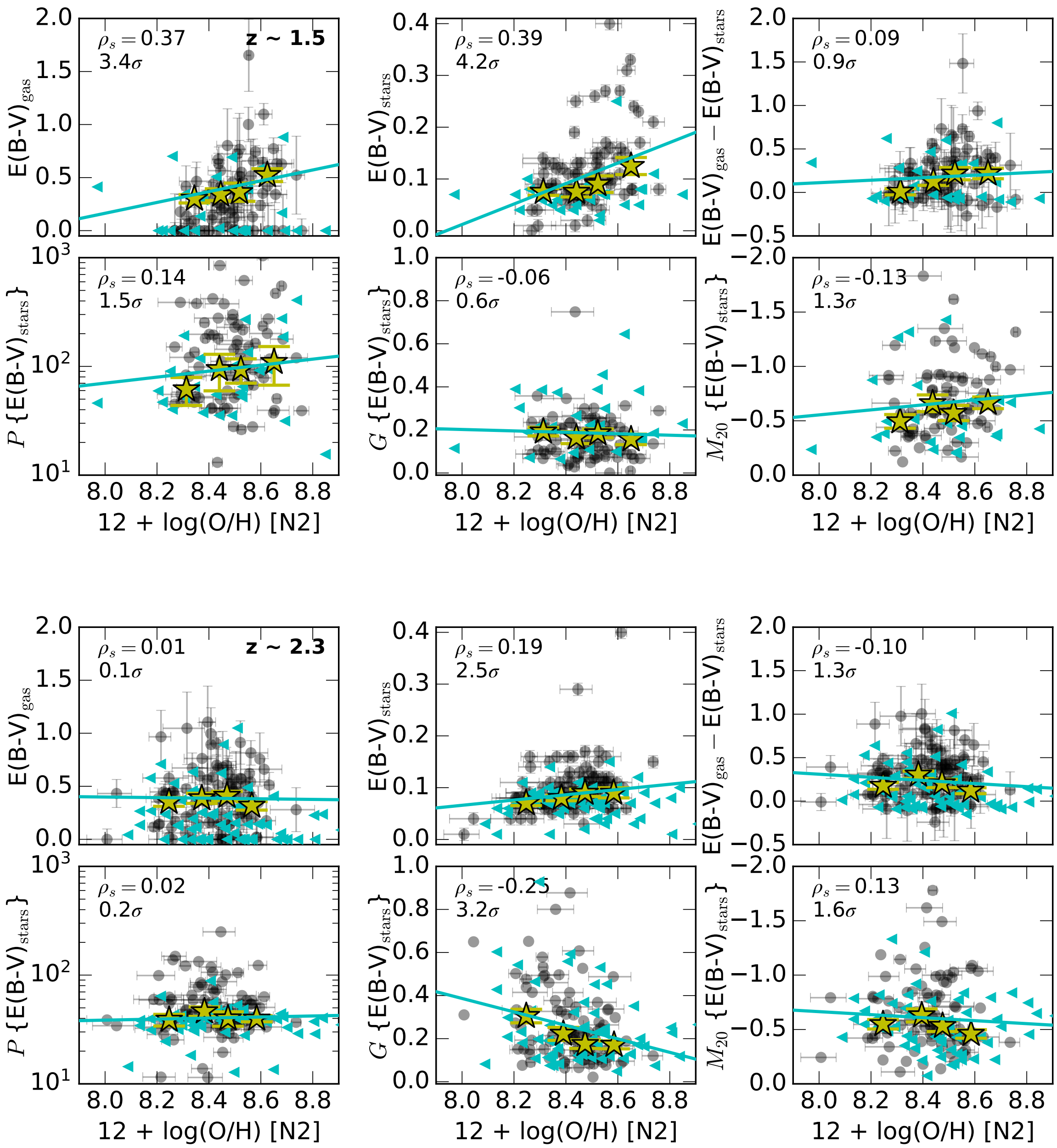

Figure 4.7: Same as Figure 4.4, except showing the relationship between metallicity and various probes of dust reddening for a subset of 104 galaxies from the $z \sim 1.5$ sample (*top*) and 158 galaxies from the $z \sim 2.3$ sample (*bottom*). Gas-phase oxygen abundances are obtained by assuming the Pettini & Pagel (2004) calibrations for the N2 indicator. The left- and right-facing light blue triangles show lower and upper limits on the metallicities, respectively.

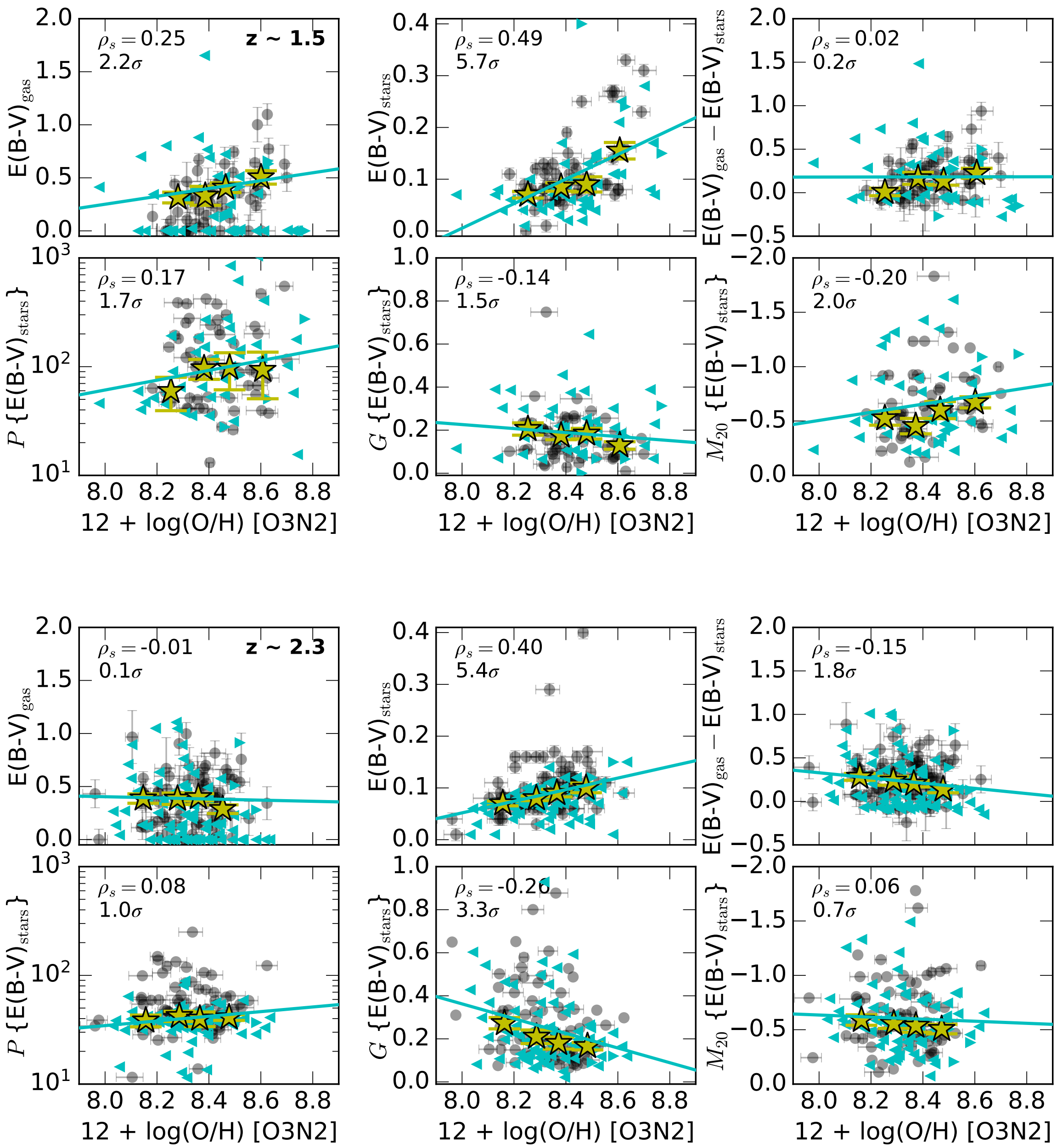

Figure 4.8: Same as Figure 4.7, except using the O3N2 metallicity indicator from Pettini & Pagel (2004).

Gas-phase metallicities are based on the [NII]λ6585, Hα, [OIII]λ5008, and Hβ emission line measurements from the MOSDEF survey (see Section 4.2.2). The empirical calibrations from Pettini & Pagel (2004) are assumed to obtain gas-phase oxygen abundances (12+log(O/H)) based on the [NII]λ6585/Hα (N2) and [OIII]λ5008/Hβ (O3N2) indicators (Sanders et al. 2015). Since these emission line ratios are close in wavelength, the lines are not corrected for the obscuring effects of dust. If [NII]λ6585 and/or Hα is not detected with a S/N > 3, then an upper limit on the metallicity is assumed. If [OIII]λ5008 and/or Hβ is not detected with a S/N > 3, then a lower limit on the metallicity is assumed. Any other combination of lines that are not detected with a S/N > 3 is not useful for obtaining gas-phase metallicities. Based on these restrictions, gas-phase metallicities are obtained for 262 galaxies with 128 of those galaxies having either upper or lower limits on their metallicities.

Figure 4.7 and Figure 4.8 shows all measures of $E(B-V)$ versus metallicity for the N2 and O3N2 indicators, respectively, split by the $z \sim 1.5$ and $z \sim 2.3$ samples. All point symbols and lines are the same as Figure 4.4, except upper and lower limits on the metallicities are additionally shown as left- and right-facing light blue triangles, respectively. Several properties are correlated with both metallicity indicators, but not necessarily in both redshift bins. High-metallicity galaxies in the $z \sim 1.5$ sample exhibit higher globally averaged $E(B-V)_{\rm gas}$, globally averaged $E(B-V)_{\rm stars}$, and P calculated from the $E(B-V)_{\rm stars}$ distribution and lower M_{20} calculated from the $E(B-V)_{\rm stars}$ distribution. The $z \sim 2.3$ sample similarly shows that high-metallicity galaxies have high globally averaged $E(B-V)_{\rm stars}$, but the low-metallicity galaxies tend to have larger differences between

$E(B-V)_{\rm stars}$ and $E(B-V)_{\rm gas}$ and higher G calculated on the $E(B-V)_{\rm stars}$ distribution. Using the O3N2 indicator alone, high-metallicity galaxies in both redshift bins are patchier with lower Gini. Meanwhile, the N2 indicator shows potential evidence for higher M_{20} in high-metallicity galaxies at $z \sim 2.3$, which is opposite of the relationship found in the $z \sim 1.5$ galaxies. Disagreement between the redshift bins may imply that these relationships are fundamentally different for galaxies from these two epochs in cosmic time.

As briefly mentioned in Section 4.4.1, low-mass galaxies tend to exhibit smoother $E(B-V)_{\rm stars}$ distributions, while higher mass galaxies have more variation in their $E(B-V)_{\rm stars}$ distributions and are on average patchier. This trend in the patchiness distribution is similarly observed with metallicity for the $z \sim 1.5$ sample. The increase in variation of the $E(B-V)_{\rm stars}$ distribution is shown in Figure 4.9 by the relationship between the dispersion of P in four equally sized bins of stellar mass and metallicity. The dispersion of P is higher for the $z \sim 1.5$ sample than the $z \sim 2.3$ sample in all cases. The higher dispersion in the $z \sim 1.5$ galaxies is either due to intrinsically higher variation in the $E(B-V)_{\rm stars}$ distribution of the $z \sim 1.5$ galaxies overall, or their generally higher resolution (more Voronoi bins) than galaxies in the $z \sim 2.3$ sample.

4.4.3 ISM Evolution

Here we present a potential physical interpretation that incorporates all of the relationships observed between different probes of $E(B-V)$, stellar mass, and metallicity. Overall, we suggest that the dust distribution in high-redshift galaxies transitions from a smooth to patchier dust distribution as galaxies increase in stellar mass. While we focus on

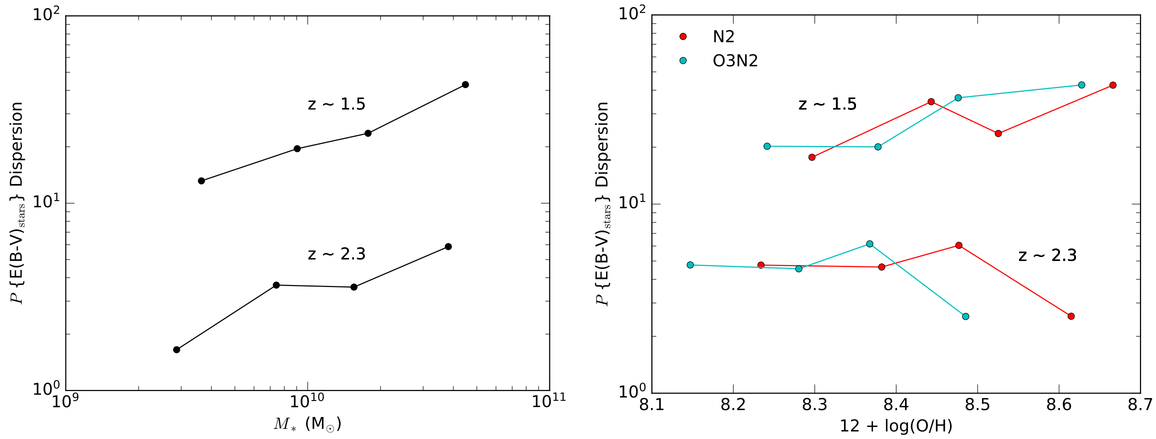

Figure 4.9: Dispersion in the P calculated on the $E(B-V)_{\text{stars}}$ distribution versus stellar mass (*left*) and metallicity (*right*). The points indicate four equally sized bins in stellar mass or metallicity. These binned points are grouped the same as the yellow stars from Figure 4.4 and Figure 4.5 (black points in left panel), Figure 4.7 (red points in right panel), and Figure 4.8 (light blue points in right panel). The red points are based on the N2 metallicity indicator and the light blue points are based on the O3N2 metallicity indicator. The offset in P dispersion between the $z \sim 1.5$ and $z \sim 2.3$ samples is due to either increased variation in the $E(B-V)_{\text{stars}}$ distribution of $z \sim 1.5$ galaxies or their higher resolution (more Voronoi bins) compared to galaxies in the $z \sim 2.3$ sample.

the dust distribution with stellar mass, the observed trends are also similar with gas-phase metallicity. In the discussion that follows, we describe this interpretation in-depth using Figure 4.10 by first discussing the characteristics of the low- and high-mass galaxies (see Figure 4.6), then concluding with a transition mechanism as galaxies increase in stellar mass. For galaxies in the sample presented in this study, this low- and high-mass split occurs at $\sim 10^{10}\,M_\odot$.

An illustration of low-mass galaxies is shown on the left side of Figure 4.10. Low-mass galaxies (that are also low in metallicity) are observed to exhibit average $E(B-V)_{\text{gas}}$ and $E(B-V)_{\text{stars}}$ that are low and approximately equal, which indicates that low-mass galaxies have generally low dust content. Low-mass galaxies also consistently have low measures of P in their $E(B-V)_{\text{stars}}$ distribution, which implies that the distribution of dust is very smooth (large yellow circle).[7] The higher G in low-mass galaxies suggests that regions with higher $E(B-V)_{\rm stars}$ exist (also see Figure 4.3), but the higher M_{20} values indicate that the high $E(B-V)_{\rm stars}$ regions are not concentrated in a single area (small orange circles). The expectation is that the regions with higher $E(B-V)_{\rm stars}$ likely correspond to sites of star formation and sources of dust production through stellar evolutionary processes (supernovae, AGB stars, etc.; see Gall et al. 2011 for a recent review), although confirmation would require resolved nebular emission line maps, which is beyond the scope of this study.

The right side of Figure 4.10 shows an illustration of high-mass galaxies, which are also high in metallicity. While $E(B-V)_{\rm gas}$ is observed to be higher than $E(B-V)_{\rm stars}$ in high-mass galaxies, both $E(B-V)_{\rm gas}$ and $E(B-V)_{\rm stars}$ are high when compared to the $E(B-V)$ of low-mass galaxies (e.g., Reddy et al. 2015). These trends suggest that while high-mass galaxies are overall dustier than low-mass galaxies (medium-sized orange circles), the amount of dust towards star-forming regions is more enhanced than the dust throughout the entire ISM (small dark orange circles). High-mass and high-metallicity galaxies are observed to be more likely to exhibit patchy $E(B-V)_{\rm stars}$ distributions, which indicates that there are several regions with either higher or lower $E(B-V)_{\rm stars}$ compared to the average $E(B-V)_{\rm stars}$ of the galaxy. High-mass galaxies also exhibit low G calculated on their $E(B-V)_{\rm stars}$ distributions, but the average $E(B-V)_{\rm stars}$ is higher in high-mass galaxies such that there are no high $E(B-V)_{\rm stars}$ outliers to drive G up (see Figure 4.3). Therefore, a high P and low G indicates that there are several low $E(B-V)_{\rm stars}$ outliers that are driving P to higher values (yellow regions near edges). Our interpretation is that

[7] Low P is not caused by having fewer Voronoi bins (see Appendix C) or a bias towards low S/N components, since they are not included (see Section 4.2.4).

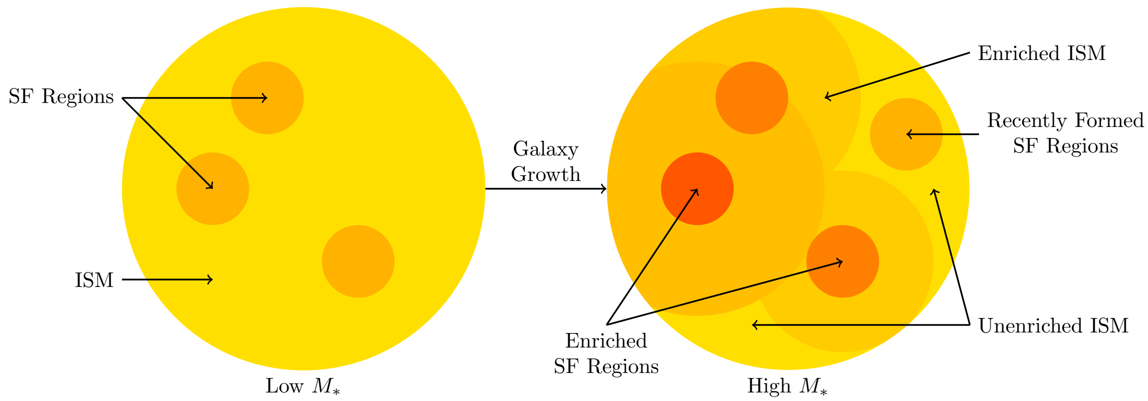

Figure 4.10: Illustration demonstrating dust production within star-forming regions that spreads radially outwards from each star-forming region and enriches the ISM as galaxies increase in stellar mass. Yellow regions represent the unenriched ISM, small orange circles designate star-forming regions that become redder as dust is produced through stellar evolutionary processes (AGB stars, supernovae, etc.), and large orange circles show the enriched ISM caused by dust radially spreading from star-forming regions to the nearby ISM. The radially expanding dust (large orange circles) may overlap such that the dust would appear concentrated within a single continuous clump. Dust mixing timescales may be faster in low-mass galaxies due to their physically smaller sizes compared to high-mass galaxies, but the size–M_* relation is not explicitly shown in this illustration.

while the total amount of dust is increasing throughout the ISM in high-mass galaxies, some regions that are not yet enriched exist. Lastly, the $E(B-V)_{\rm stars}$ distributions are observed to have lower M_{20} values in the $z\sim1.5$ sample, suggesting that the dustiest regions are generally concentrated in a single clump (overlapping orange regions). The lack of clustered dust reddening in the $z\sim2.3$ sample could be explained by galaxies at higher redshifts being at an earlier stage in their evolution where the dust from their star-forming regions has not yet merged or due to $z\sim2.3$ galaxies being less resolved than the $z\sim1.5$ galaxies.

We interpret these results as potentially tracing a physical transition between a smooth to clumpy dust distribution in the ISM with increasing stellar mass. The distribution of dust has traditionally been approximated by either a uniform dust screen or a two-component dust model (e.g., Calzetti et al. 1994; Charlot & Fall 2000) with higher optical depths towards star-forming regions causing $E(B-V)_{\rm gas}$ to be ∼2.27 times higher than $E(B-V)_{\rm stars}$ (Calzetti et al. 2000). These results may suggest that low-mass galaxies begin with a diffuse, mostly uniform dust distribution spread throughout their ISM. Several studies using simulations have suggested that dust mixes nearly instantaneously between the cold and warm ISM (e.g., McKee 1989; Tielens 1998; Peters et al. 2017). These observations are in agreement with instantaneous mixing of dust throughout the entire ISM in specifically low-mass galaxies, which is likely due to their physically smaller sizes. As galaxies increase in stellar mass through in-situ star formation, they will produce significantly more dust through stellar evolutionary processes (supernovae, AGB stars, etc.; see Gall et al. 2011 for a recent review) and have physically larger sizes than their low-mass counter parts. We suggest that regions closest to sites of dust production (star-forming regions) within high-mass galaxies will become enriched first, while the remainder of the ISM becomes enriched on longer timescales. If star-forming regions are closely spaced or sufficient time has passed, then the dust that is enriching the ISM radially outwards from star-forming regions will aggregate to form a single concentration of dust that may also be centrally concentrated in the galaxy ($z \sim 1.5$ sample). Alternatively, new star-forming regions may arise or the star-forming regions may be sufficiently spaced, thus maintaining several concentrations of dust throughout the ISM of high-mass and high-metallicity galaxies ($z \sim 2.3$ sample).

In short, we suggest that the evolution of the dust distribution in the ISM is correlated with stellar mass. Low-mass galaxies are observed to exhibit consistently smooth dust distributions, possibly caused by instantaneous mixing of dust throughout their ISM. Meanwhile, high-mass galaxies show more complex dust distributions on average compared to low-mass galaxies, perhaps attributed to the dust needing to travel larger distances through their more expansive ISM. We do not speculate specific dust mixing timescales, as the mixing rates depend on several factors (e.g., IMF, supernovae rate, gas density distribution, etc.) that are beyond the scope of this work.

4.4.4 Discussion

While applying the Gini and M_{20} morphology metrics to the $E(B-V)_{\rm stars}$ distribution is novel to this work, the shape of the radial profiles in the $E(B-V)_{\rm stars}$ distribution can be inferred from our results. It is expected that centrally peaked radial profiles would exhibit lower M_{20}. High Gini could indicate steeper radial gradients, but the high concentration detected by the Gini coefficient does not necessarily need to be grouped in the a single region (e.g., the center). Several studies have observed $E(B-V)_{\rm stars}$ and $E(B-V)_{\rm gas}$ to be centrally peaked in the centers of $z \sim 2$ galaxies, with some evidence for steeper radial gradients as galaxies increase in stellar mass (e.g. Nelson et al. 2013, 2016; Hemmati et al. 2015; Tacchella et al. 2018). These observations are in agreement with our findings of lower M_{20} in the $z \sim 1.5$ high-mass galaxies. We suspect that Gini is low in high-mass galaxies primarily due to higher mass galaxies being overall dustier, such that the reddest regions do not stand out compared to the average (see Figure 4.3). Tacchella et al. (2018) also found that several galaxies in their sample of 10 star-forming galaxies at $z \sim 2$ ($M_* \sim 10^{10}$–

$10^{11.4}\,M_\odot$) exhibited secondary local maxima in their radial attenuation profiles, while the combined profile showed a mostly smooth gradient. Secondary non-central peaks in the $E(B-V)_{\rm stars}$ distribution of high-mass galaxies could also explain why Gini is low in high-mass galaxies. If these secondary peaks are within the 20% reddest regions, then M_{20} would also be higher, which could explain why M_{20} is higher for galaxies in the $z \sim 2.3$ sample that are high in mass and metallicity. Resolved metallicity radial profiles, on the other hand, have been observed to be generally flat in most galaxies at $z \sim 2$ (e.g., Jones et al. 2015; Leethochawalit et al. 2016; Wuyts et al. 2016; Wang et al. 2019). These observations may suggest that the gas-phase metallicity mixes throughout the ISM of galaxies at all masses nearly instantaneously and does not necessarily follow the dust that is probed by the $E(B-V)_{\rm stars}$ distribution, which we suggest has longer dust-mixing timescales in high-mass galaxies.

While patchiness is a newly derived morphology metric, we found in Appendix C that P calculated on the $E(B-V)_{\rm stars}$ distribution is significantly correlated with ICD (Papovich et al. 2003). Boada et al. (2015) found that higher mass galaxies (up to $M_* = 10^{11}\,M_\odot$) at $z \sim 2$ tend to have higher ICD, which is comparable with our findings that the $E(B-V)_{\rm stars}$ distribution tends to be patchier in higher mass galaxies. Several studies have suggested that patchy dust distributions could explain observed differences between inferred reddening (e.g., Calzetti et al. 1994; Wild et al. 2011; Price et al. 2014; Reddy et al. 2015, 2018b, 2020, in press) and SFR indicators (e.g., Boquien et al. 2009, 2015; Hao et al. 2011; Reddy et al. 2015; Katsianis et al. 2017, Fetherolf et al. 2020b, in prep.; Chapter 3). Recently, Shivaei et al. (2020) also found that the dust attenuation curve of high-metallicity galaxies at $z \sim 2$ exhibit steeper UV slopes compared to low-metallicity galaxies, possibly due to patchier dust distributions in high-metallicity galaxies. In Section 4.4.2, we showed that metal-rich galaxies tend to exhibit patchier $E(B-V)_{\rm stars}$ distributions, which is inferred to represent the distribution of dust. Furthermore, Shivaei et al. (2017) found that dust emission by PAH molecules is stronger in high-metallicity galaxies and is stronger for the O3N2 indicator compared to the N2 metallicity indicator, which corresponds with our findings that the trend between P and gas-phase metallicity is stronger with the O3N2 metallicity indicator than the N2 indicator. In contention with our conclusions, Shivaei et al. (2020) also suggests that the higher difference between $E(B-V)_{\rm stars}$ and $E(B-V)_{\rm gas}$ observed in low-metallicity galaxies may be attributed to patchier dust distributions in these galaxies. We similarly observe this trend in the $z \sim 2.3$ sample, but alternatively suggest that this could be explained similarly to the high Gini observed in low-mass and low-metallicity galaxies (see Figure 4.3), in that both $E(B-V)_{\rm stars}$ and $E(B-V)_{\rm gas}$ are nearly zero in these galaxies and minor differences could be artificially amplified. Overall, pairing the inferred patchier dust distributions from this study with the observed differences in attenuation curve shape with metallicity by Shivaei et al. (2020) suggests that assuming a single attenuation curve shape may not necessarily be appropriate for all high-redshift galaxies. Since the highest mass and metallicity galaxies seem to exhibit patchier dust distributions, their starlight may more appropriately be corrected for dust obscuration by assuming a Calzetti et al. (2000) dust attenuation curve with a shallower UV slope, opposed to an SMC dust extinction curve (Fitzpatrick & Massa 1990; Gordon et al. 2003) that is more appropriate for low-mass galaxies with smoother dust distributions.

4.5 Summary

We investigated the inferred distribution of dust for a sample of 310 star-forming galaxies from the MOSDEF survey at spectroscopic redshifts $1.36 < z < 2.66$ using a new morphology metric called patchiness (P), the Gini coefficient (G), and second-order moment of light (M_{20}). The morphology metrics were used to quantify the robust dust reddening maps that were constructed from CANDELS/3D-HST high-resolution imaging. We found that the morphology metrics calculated on the $E(B-V)_{\rm stars}$ distribution vary most significantly with stellar mass. The morphology metrics were also shown to vary with gas-phase metallicity, as is expected from the well-known relationship between mass and metallicity. Globally averaged $E(B-V)_{\rm gas}$ and $E(B-V)_{\rm stars}$ are also included in this analysis to help build a physical interpretation for the evolution of the distribution of dust throughout the ISM of high-redshift galaxies. An illustration of this physical interpretation is shown in Figure 4.10 and our main conclusions are summarized as follows.

- In low-mass galaxies, $E(B-V)_{\rm gas}$ and $E(B-V)_{\rm stars}$ are low and approximately equal. As galaxies increase in stellar mass, both $E(B-V)_{\rm gas}$ and $E(B-V)_{\rm stars}$ individually increase along with the difference between them. We suspect that low-mass galaxies efficiently mix the dust formed through stellar evolutionary processes (e.g., supernovae, AGB stars, etc.) throughout their ISM compared to high-mass galaxies that have longer dust mixing timescales due to their physically larger sizes. High-mass galaxies also produce significantly more dust than low-mass galaxies, such that only the regions closest to the sites of dust production (star-forming regions) become enriched on short timescales. This effect is shown in Figure 4.10 by the small orange circles becoming darker as the star-forming regions get dustier.

- The patchiness metric, P, that we define in Equation 4.2 is sensitive to both the high and low outliers of a distribution. Low-mass and low-metallicity galaxies exhibit consistently low patchiness in their $E(B-V)_{\rm stars}$ distributions, indicating that the dust is uniformly distributed throughout their ISM. Meanwhile, high-mass and high-metallicity galaxies are more likely to exhibit patchy $E(B-V)_{\rm stars}$ distributions due to the presence of both extremely dusty star-forming regions and regions that are sufficiently far from any sites star formation that are not yet enriched. The effect of patchiness is shown in Figure 4.10 by low-mass galaxies being mostly a single yellow color while high-mass galaxies appear much more complex with both dark orange and light yellow regions.

- The resolved $E(B-V)_{\rm stars}$ distribution exhibits high G in low-mass galaxies possibly due to sites of star formation that enhance the dust opacity enough in isolated regions relative to the generally unenriched ISM to drive G up (Section 4.3.3 and Figure 4.3) but not P. Since the Gini coefficient is only sensitive to above average values, G on the $E(B-V)_{\rm stars}$ distribution becomes less sensitive as galaxies become dustier at higher stellar masses and metallicities.

- Higher M_{20} on the $E(B-V)_{\rm stars}$ distribution of low-mass galaxies indicates that the dustiest regions exist in several isolated clumps. We propose that stellar feedback pushes dust radially outwards from star-forming regions over time. Therefore, high-mass and high-metallicity galaxies may either exhibit lower M_{20} from the expanding dust bubbles overlapping and blending into a single group ($z \sim 1.5$ sample), or M_{20} may remain high if new star-forming regions arise ($z \sim 2.3$ sample). The expanding dust in the ISM is shown by medium-sized orange circles that overlap in Figure 4.10.

Our derived patchiness parameter demonstrates that void-like regions within galaxies should not be ignored, as they can reveal valuable information about galactic structure. Furthermore, using patchiness, Gini, M_{20}, and other morphology metrics together is critical towards painting a complete picture of the resolved structures within galaxies. In general, measurements of galaxy morphologies must improve upon radial and visual dependencies as sample sizes increase with the advent of statistically large resolved imaging surveys. Deeper resolved observations that probe even higher redshifts will reveal structures of galaxies that are increasingly irregular, which brings into question how the center of these galaxies should be defined. Future observations with the *James Webb Space Telescope* will build upon the results presented in this paper by obtaining high-resolution imaging with NIRCam and resolved spectroscopy with NIRSpec of galaxies out to $z \sim 6$. These observations will enable construction of high-resolution stellar population, reddening, and emission line maps that will further reveal how galaxies assemble and evolve across cosmic time.

Chapter 5

Conclusions

In order to study the distribution of stars and dust in $z \sim 2$ galaxies, this work has taken advantage of the legacy of the data coverage of the CANDELS extragalactic fields. High-resolution CANDELS/3D-HST imaging (Grogin et al. 2011; Koekemoer et al. 2011; Skelton et al. 2014) was combined with spectroscopic redshifts and emission line measurements from the MOSDEF survey (Kriek et al. 2015) to construct stellar population and robust reddening maps for ~300 star-forming galaxies at $1.25 < z < 2.66$. An improved method for constructing stellar population and reddening maps was described in Chapter 2, Hα and UV measurements were directly compared within the spectroscopic slit area in Chapter 3 to avoid aperture biases, and a new morphology metric called "patchiness" was introduced in Chapter 4 to quantify the resolved stellar continuum reddening distribution.

5.1 Big Picture

The questions that were presented in Section 1.2 are addressed as follows in order to place the conclusions of this dissertation into context with the bigger picture of galaxy evolution across cosmic time.

1. How does the geometry of stars and dust affect globally measured physical properties of galaxies?

The analyses presented in Chapter 2 showed that understanding how resolved stellar properties affect globally measured properties requires careful treatment of the photometry. It is important to ensure that the best-fit resolved SEDs are well-constrained, especially covering key features of the SED such as the UV slope (1250–2500 Å) and Balmer/4000 Å breaks. Poorly constrained UV slopes, in particular, can cause the reddening derived from the resolved SEDs to be systematically higher than those that result from resolved SEDs that are well-constrained by the photometry (see Figure 2.9). To best constrain the resolved photometry, it is recommended that at least 2 filters cover critical SED features, information from multiple filters are incorporated into the binning technique such that several resolved filters are measured with high confidence, and poorly constrained resolved components are not included in resolved analyses when possible (see Section 2.3.2). When applying the improved binning technique that incorporates information from multiple filters (see Figure 2.2) to the $z \sim 2.3$ sample, it was found that the integrated stellar population properties seem to be well-approximated by the unresolved photometry (see Figure 2.7).

In Chapter 3, different probes of dust reddening and SFR were measured directly within the MOSFIRE spectroscopic slit area to avoid potential aperture biases from the slit-loss corrections (see Figure 3.2). The stellar continuum dust reddening on the scale of the slit width (~23 kpc) was found to be approximately the same as the globally averaged stellar continuum reddening for star-forming galaxies at $z \sim 2$. While Hα-to-UV SFR ratios were found to be higher inside the slit region than when globally averaged, this observation is considered physical in nature and not attributed to the effects of slit-loss (see left panel of Figure 3.3). The recent results from Shivaei et al. (2020) found that the attenuation curve of high-metallicity galaxies exhibits a shallower UV slope than low metallicity galaxies and it was shown in Chapter 4 that high-mass galaxies that are metal-rich tend to have patchier dust distributions (see Section 4.4.4). These combined results suggest that assuming a dust attenuation curve with a flatter UV slope (e.g., Calzetti et al. 2000) may be a more appropriate choice in order to account for the patchier dust distributions that are observed in massive (see Figure 4.4 and Figure 4.5) and metal-rich galaxies (see Figure 4.7 and Figure 4.8) at $z \sim 2$.

2. What causes nebular dust attenuation to be higher than that of the stellar continuum and how does this relate to potential differences between Hα and UV SFR indicators?

Since there is still an observed difference between nebular and stellar continuum reddening when obtained directly within the slit in Chapter 3, these differences are not caused by aperture effects (see Figure 3.6). Furthermore, Hα SFRs were found to be higher than UV SFRs in galaxies with very high SFRs (see Figure 3.3). When comparing globally averaged and slit-measured Hα-to-UV SFR ratios, it was found that Hα-to-UV SFRs were even higher in the centers of large galaxies (see Figure 3.4). Dust reddening does not change significantly when derived over the slit or across the entire galaxy, such that the differences between the SFR indicators are not caused by differences in the attenuated light. However, these observations could be explained by Hα and UV light profiles that do not match at all radii or if Balmer decrement profiles are peaked in the centers of galaxies (e.g., Nelson et al. 2013, 2016; Hemmati et al. 2015; Tacchella et al. 2018). Patchy dust distributions could cause the UV light to be scattered to larger radii than the Hα light and, thus, could explain the differences in their radial profiles.

Chapter 4 includes a possible explanation for the observed trend between differences in reddening indicators and stellar mass (see Figure 4.10). Dust attenuation from the stellar continuum is approximately equal to the dust from sites of recent star formation in low mass galaxies (see Figure 4.4 and Figure 4.5). As galaxies increase in mass, dust is produced through stellar evolutionary processes (e.g., supernovae, AGB stars, etc.; see Gall et al. 2011 for a recent review) such that there are higher dust opacities towards the most massive stars that have recently formed, thus causing the difference between stellar continuum and nebular reddening. These regions are preferentially dustier in high-mass galaxies as the recently produced dust has not had sufficient time to mix throughout the ISM.

3. How does the geometry of stars and dust change as galaxies evolve?

It is proposed in Chapter 4 that the distribution of dust transitions from smooth to patchy as galaxies increase in stellar mass (see Figure 4.10). Low-mass galaxies have low amounts of dust overall, such that the dust distribution is relatively smooth (see Figure 4.3). As galaxies increase in stellar mass, they are overall dustier, but even more so towards the most massive stars that have recently formed. Since massive galaxies are physically larger in size than low-mass galaxies (e.g., Toft et al. 2007; Trujillo et al. 2007; van der Wel et al. 2014; Scott et al. 2017; van de Sande et al. 2018), dust mixing timescales may be sufficiently long such that there also remains relatively unenriched regions that are not near any sites of dust production from recent star formation. Since there is both extremely dusty regions near sites of star formation and regions with very little dust overall, the dust distribution is overall patchier in high-mass galaxies.

4. How efficiently does dust mix throughout the ISM?

The dust reddening distribution was found to be relatively smooth for low-mass galaxies and more complex in high-redshift galaxes in Chapter 4 (see Figure 4.6). Since low-mass galaxies are physically small in size, dust may mix throughout their ISM nearly instantaneously (McKee 1989; Tielens 1998; Peters et al. 2017). On the other hand, high-mass galaxies exhibit patchy dust distributions and are physically larger in size such that they may experience longer dust-mixing timescales than low-mass galaxies. Longer dust-mixing timescales results in high-mass galaxies having both extremely dust reddened regions and areas that are sufficiently far from any recently star formation that remain relatively unenriched.

5.2 Future Work

The work presented in this dissertation can be built upon by additionally incorporating other legacy data for these same galaxies or applying the tools that were developed to different types of galaxies across a broad range of redshifts. For example, the 3D-HST survey includes resolved emission line maps of the same galaxies in the CANDELS extragalactic fields that were used in this study (Brammer et al. 2012; Momcheva et al. 2016). The Hα and Hβ emission line maps could be directly compared on the same resolved Voronoi bin scale as the resolved imaging using the methodology from Chapter 2. While the emission line maps are spatially resolved, they are not spectrally resolved such that Hα emission is blended with [NII]$\lambda\lambda 6550, 6585$. However, these lines have been spectrally resolved by MOSDEF observations for the same galaxies observed by the 3D-HST survey, such that the Hα emission line maps can be globally corrected with minimal assumptions. These spatially paired measurements could expand upon the results of Chapter 3 by comparing Hα and UV probes of reddening and SFR on scales that are smaller than the spectroscopic slit.

The patchiness metric that was developed in Chapter 4 could be used to further investigate how galaxies assemble on resolved scales by quantifying the resolved distributions of other galaxy properties (e.g., see Appendix C). Patchiness and other morphology metrics could also be used to quantify the resolved properties of cluster and field galaxies to investigate how the structure of galaxies may differ by their environments. Galaxy clusters are particularly valuable resources for studying galaxy evolution in that there are often background galaxies that are lensed by the mass of the cluster. Due to the increased surface brightness and spatial resolution of lensed galaxies, they can be used to probe resolved galaxy properties out to higher redshifts. Furthermore, since the patchiness morphology metric is not sensitive to the spatial orientation of the resolved elements, the patchiness of a lensed galaxy can be directly calculated without needing to reconstruct the galaxy image based on the lens model of the cluster. Finally, while pushing morphology to higher redshifts is difficult without increasingly higher resolution telescopes (e.g., NIRcam on the

James Webb Space Telescope), the patchiness metric can easily be applied to galaxies at lower redshifts. Studying the structure of galaxies across redshift space using the same morphology metrics will build upon our understanding of how galaxies evolve on resolved scales across cosmic time.

Bibliography

Abraham, R. G., van den Bergh, S., & Nair, P. 2003, ApJ, 588, 218, doi: 10.1086/373919

Andrews, B. H., & Martini, P. 2013, ApJ, 765, 140, doi: 10.1088/0004-637X/765/2/140

Astropy Collaboration, Robitaille, T. P., Tollerud, E. J., et al. 2013, A&A, 558, A33, doi: 10.1051/0004-6361/201322068

Astropy Collaboration, Price-Whelan, A. M., Sipőcz, B. M., et al. 2018, AJ, 156, 123, doi: 10.3847/1538-3881/aabc4f

Azadi, M., Coil, A. L., Aird, J., et al. 2017, ApJ, 835, 27, doi: 10.3847/1538-4357/835/1/27

Azadi, M., Coil, A., Aird, J., et al. 2018, ApJ, 866, 63, doi: 10.3847/1538-4357/aad3c8

Banerji, M., Lahav, O., Lintott, C. J., et al. 2010, MNRAS, 406, 342, doi: 10.1111/j.1365-2966.2010.16713.x

Barden, M., Jahnke, K., & Häußler, B. 2008, ApJS, 175, 105, doi: 10.1086/524039

Bertin, E., & Arnouts, S. 1996, A&AS, 117, 393, doi: 10.1051/aas:1996164

Boada, S., Tilvi, V., Papovich, C., et al. 2015, ApJ, 803, 104, doi: 10.1088/0004-637X/803/2/104

Boquien, M., Calzetti, D., Kennicutt, R., et al. 2009, ApJ, 706, 553, doi: 10.1088/0004-637X/706/1/553

Boquien, M., Calzetti, D., Aalto, S., et al. 2015, A&A, 578, A8, doi: 10.1051/0004-6361/201423518

Brammer, G. B., van Dokkum, P. G., Franx, M., et al. 2012, ApJS, 200, 13, doi: 10.1088/0067-0049/200/2/13

Bruzual, G., & Charlot, S. 2003, MNRAS, 344, 1000, doi: 10.1046/j.1365-8711.2003.06897.x

Calzetti, D. 2013, Secular Evolution of Galaxies, 419. http://adsabs.harvard.edu/abs/2013seg..book..419C

Calzetti, D., Armus, L., Bohlin, R. C., et al. 2000, ApJ, 533, 682, doi: 10.1086/308692

Calzetti, D., Kinney, A. L., & Storchi-Bergmann, T. 1994, ApJ, 429, 582, doi: 10.1086/174346

Cappellari, M., & Copin, Y. 2003, MNRAS, 342, 345, doi: 10.1046/j.1365-8711.2003.06541.x

Cardelli, J. A., Clayton, G. C., & Mathis, J. S. 1989, ApJ, 345, 245, doi: 10.1086/167900

Chabrier, G. 2003, PASP, 115, 763, doi: 10.1086/376392

Chan, J. C. C., Beifiori, A., Mendel, J. T., et al. 2016, MNRAS, 458, 3181, doi: 10.1093/mnras/stw502

Charlot, S., & Fall, S. M. 2000, ApJ, 539, 718, doi: 10.1086/309250

Cibinel, A., Le Floc'h, E., Perret, V., et al. 2015, ApJ, 805, 181, doi: 10.1088/0004-637X/805/2/181

Coil, A. L., Aird, J., Reddy, N., et al. 2015, ApJ, 801, 35, doi: 10.1088/0004-637X/801/1/35

Conroy, C. 2013, ARA&A, 51, 393, doi: 10.1146/annurev-astro-082812-141017

Conselice, C. J. 2003, ApJS, 147, 1, doi: 10.1086/375001

—. 2014, ARA&A, 52, 291, doi: 10.1146/annurev-astro-081913-040037

de Vaucouleurs, G. 1959, Handbuch der Physik, 53, 275, doi: 10.1007/978-3-642-45932-0_7

Dickinson, M. 2000, Philosophical Transactions of the Royal Society A: Mathematical, Physical and Engineering Sciences, 358, 2001, doi: 10.1098/rsta.2000.0626

Dieleman, S., Willett, K. W., & Dambre, J. 2015, MNRAS, 450, 1441, doi: 10.1093/mnras/stv632

Domínguez Sánchez, H., Huertas-Company, M., Bernardi, M., Tuccillo, D., & Fischer, J. L. 2018, MNRAS, 476, 3661, doi: 10.1093/mnras/sty338

Draine, B. T., & Lee, H. M. 1984, ApJ, 285, 89, doi: 10.1086/162480

Dwek, E. 1998, ApJ, 501, 643, doi: 10.1086/305829

Erb, D. K., Steidel, C. C., Shapley, A. E., et al. 2006a, ApJ, 647, 128. http://iopscience.iop.org/0004-637X/647/1/128

—. 2006b, ApJ, 646, 107, doi: 10.1086/504891

Faisst, A. L., Capak, P. L., Yan, L., et al. 2017, ApJ, 847, 21, doi: 10.3847/1538-4357/aa886c

Fetherolf, T., Reddy, N., Shapley, A., et al. 2020, ArXiv e-prints. http://arxiv.org/abs/2009.03926

Fitzpatrick, E. L., & Massa, D. 1986, ApJ, 307, 286, doi: 10.1086/164415

—. 1990, ApJS, 72, 163, doi: 10.1086/191413

Förster Schreiber, N. M., Shapley, A. E., Erb, D. K., et al. 2011, ApJ, 731, 65, doi: 10.1088/0004-637X/731/1/65

Freeman, P. E., Izbicki, R., Lee, A. B., et al. 2013, MNRAS, 434, 282, doi: 10.1093/mnras/stt1016

Gall, C., Hjorth, J., & Andersen, A. C. 2011, A&A Rev., 19, 43, doi: 10.1007/s00159-011-0043-7

Genzel, R., Tacconi, L. J., Kurk, J., et al. 2013, ApJ, 773, 68, doi: 10.1088/0004-637X/773/1/68

Gordon, K. D., Clayton, G. C., Misselt, K. A., Landolt, A. U., & Wolff, M. J. 2003, ApJ, 594, 279, doi: 10.1086/376774

Green, A. W., Glazebrook, K., Gilbank, D. G., et al. 2017, MNRAS, 470, 639, doi: 10.1093/mnras/stx1119

Griffiths, R. E., Casertano, S., Ratnatunga, K. U., et al. 1994, ApJ, 435, L19, doi: 10.1086/187584

Grogin, N. A., Kocevski, D. D., Faber, S. M., et al. 2011, ApJS, 197, 35, doi: 10.1088/0067-0049/197/2/35

Guo, Y., Giavalisco, M., Ferguson, H. C., Cassata, P., & Koekemoer, A. M. 2012, ApJ, 757, 120, doi: 10.1088/0004-637X/757/2/120

Guo, Y., Ferguson, H. C., Bell, E. F., et al. 2015, ApJ, 800, 39, doi: 10.1088/0004-637X/800/1/39

Guo, Y., Rafelski, M., Bell, E. F., et al. 2018, ApJ, 853, 108, doi: 10.3847/1538-4357/aaa018

Hao, C.-N., Kennicutt, R. C., Johnson, B. D., et al. 2011, ApJ, 741, 124, doi: 10.1088/0004-637X/741/2/124

Hemmati, S., Mobasher, B., Darvish, B., et al. 2015, ApJ, 814, 46, doi: 10.1088/0004-637X/814/1/46

Hemmati, S., Miller, S. H., Mobasher, B., et al. 2014, ApJ, 797, 108, doi: 10.1088/0004-637X/797/2/108

Hubble, E. P. 1926, ApJ, 64, doi: 10.1086/143018

Hunter, J. D. 2007, Computing in Science & Engineering, 9, 90, doi: 10.1109/MCSE.2007.55

Jenkins, E. B. 2009, ApJ, 700, 1299, doi: 10.1088/0004-637X/700/2/1299

Jones, T., Wang, X., Schmidt, K. B., et al. 2015, AJ, 149, 107, doi: 10.1088/0004-6256/149/3/107

Jung, I., Finkelstein, S. L., Song, M., et al. 2017, ApJ, 834, 81, doi: 10.3847/1538-4357/834/1/81

Kashino, D., Silverman, J. D., Rodighiero, G., et al. 2013, ApJ, 777, L8, doi: 10.1088/2041-8205/777/1/L8

Katsianis, A., Blanc, G., Lagos, C. P., et al. 2017, MNRAS, 472, 919, doi: 10.1093/mnras/stx2020

Kennicutt, R. C., & Evans, N. J. 2012, ARA&A, 50, 531, doi: 10.1146/annurev-astro-081811-125610

Kennicutt, Jr., R. C. 1998, ApJ, 498, 541, doi: 10.1086/305588

Kewley, L. J., & Ellison, S. L. 2008, ApJ, 681, 1183, doi: 10.1086/587500

Kewley, L. J., Jansen, R. A., & Geller, M. J. 2005, PASP, 117, 227, doi: 10.1086/428303

Koekemoer, A. M., Faber, S. M., Ferguson, H. C., et al. 2011, ApJS, 197, 36, doi: 10.1088/0067-0049/197/2/36

Kreckel, K., Groves, B., Schinnerer, E., et al. 2013, ApJ, 771, 62, doi: 10.1088/0004-637X/771/1/62

Kriek, M., Shapley, A. E., Reddy, N. A., et al. 2015, ApJS, 218, 15, doi: 10.1088/0067-0049/218/2/15

Lang, P., Wuyts, S., Somerville, R. S., et al. 2014, ApJ, 788, 11, doi: 10.1088/0004-637X/788/1/11

Lee, B., Giavalisco, M., Whitaker, K., et al. 2018, ApJ, 853, 131, doi: 10.3847/1538-4357/aaa40f

Leethochawalit, N., Jones, T. A., Ellis, R. S., et al. 2016, ApJ, 820, 84, doi: 10.3847/0004-637X/820/2/84

Leung, G. C. K., Coil, A. L., Aird, J., et al. 2019, ApJ, 886, 11, doi: 10.3847/1538-4357/ab4a7c

Lintott, C., Schawinski, K., Bamford, S., et al. 2011, MNRAS, 410, 166, doi: 10.1111/j.1365-2966.2010.17432.x

Lintott, C. J., Schawinski, K., Slosar, A., et al. 2008, MNRAS, 389, 1179, doi: 10.1111/j.1365-2966.2008.13689.x

Lisker, T. 2008, ApJS, 179, 319, doi: 10.1086/591795

Lotz, J. M., Primack, J., & Madau, P. 2004, AJ, 128, 163, doi: 10.1086/421849

Lotz, J. M., Davis, M., Faber, S. M., et al. 2008, ApJ, 672, 177, doi: 10.1086/523659

Madau, P., & Dickinson, M. 2014, ARA&A, 52, 415, doi: 10.1146/annurev-astro-081811-125615

Mannucci, F., Cresci, G., Maiolino, R., Marconi, A., & Gnerucci, A. 2010, MNRAS, 408, 2115, doi: 10.1111/j.1365-2966.2010.17291.x

McKee, C. 1989, in Proc. IAU Symp. 135, Interstellar Dust, ed. L. J. Allamandola & A. G. G. M. Tielens (Dordrecht: Kluwer Academic Publishers), 431. http://adsabs.harvard.edu/abs/1989IAUS..135..431M

McLean, I. S., Steidel, C. C., Epps, H., et al. 2010, in Ground-based and Airborne Instrumentation for Astronomy III, Vol. 7735 (Proceedings of the SPIE), 77351E, doi: 10.1117/12.856715

McLean, I. S., Steidel, C. C., Epps, H. W., et al. 2012, in Ground-based and Airborne Instrumentation for Astronomy IV, Vol. 8446, 84460J, doi: 10.1117/12.924794

Meurer, G. R., Heckman, T. M., & Calzetti, D. 1999, ApJ, 521, 64, doi: 10.1086/307523

Momcheva, I. G., Brammer, G. B., van Dokkum, P. G., et al. 2016, ApJS, 225, 27, doi: 10.3847/0067-0049/225/2/27

Narayanan, D., Davé, R., Johnson, B. D., et al. 2018, MNRAS, 474, 1718, doi: 10.1093/mnras/stx2860

Nelson, E. J., van Dokkum, P. G., Momcheva, I., et al. 2013, ApJ, 763, L16, doi: 10.1088/2041-8205/763/1/L16

Nelson, E. J., van Dokkum, P. G., Momcheva, I. G., et al. 2016, ApJ, 817, L9, doi: 10.3847/2041-8205/817/1/L9

Oke, J. B., & Gunn, J. E. 1983, ApJ, 266, 713, doi: 10.1086/160817

Oliphant, T. E. 2007, Computing in Science & Engineering, 9, 10, doi: 10.1109/MCSE.2007.58

Osterbrock, D. E. 1989, Astrophysics of gaseous nebulae and active galactic nuclei (John Simon Guggenheim Memorial Foundation, University of Minnesota, et al. Mill Valley, CA, University Science Books)

Papovich, C., Dickinson, M., Giavalisco, M., Conselice, C. J., & Ferguson, H. C. 2005, ApJ, 631, 101, doi: 10.1086/429120

Papovich, C., Giavalisco, M., Dickinson, M., Conselice, C. J., & Ferguson, H. C. 2003, ApJ, 598, 827, doi: 10.1086/378976

Peng, C. Y., Ho, L. C., Impey, C. D., & Rix, H.-W. 2002, AJ, 124, 266, doi: 10.1086/340952

—. 2010, AJ, 139, 2097, doi: 10.1088/0004-6256/139/6/2097

Peters, T., Zhukovska, S., Naab, T., et al. 2017, MNRAS, 467, 4322, doi: 10.1093/mnras/stx341

Pettini, M., & Pagel, B. E. J. 2004, MNRAS, 348, L59, doi: 10.1111/j.1365-2966.2004.07591.x

Price, S. H., Kriek, M., Brammer, G. B., et al. 2014, ApJ, 788, 86, doi: 10.1088/0004-637X/788/1/86

Reddy, N. A., Erb, D. K., Pettini, M., Steidel, C. C., & Shapley, A. E. 2010, ApJ, 712, 1070, doi: 10.1088/0004-637X/712/2/1070

Reddy, N. A., Pettini, M., Steidel, C. C., et al. 2012, ApJ, 754, 25, doi: 10.1088/0004-637X/754/1/25

Reddy, N. A., Kriek, M., Shapley, A. E., et al. 2015, ApJ, 806, 259, doi: 10.1088/0004-637X/806/2/259

Reddy, N. A., Oesch, P. A., Bouwens, R. J., et al. 2018a, ApJ, 853, 56, doi: 10.3847/1538-4357/aaa3e7

Reddy, N. A., Shapley, A. E., Sanders, R. L., et al. 2018b, ApJ, 869, 92, doi: 10.3847/1538-4357/aaed1e

Richards, S. N., Bryant, J. J., Croom, S. M., et al. 2016, MNRAS, 455, 2826, doi: 10.1093/mnras/stv2453

Sanders, R. L., Shapley, A. E., Kriek, M., et al. 2015, ApJ, 799, 138, doi: 10.1088/0004-637X/799/2/138

—. 2018, ApJ, 858, 99, doi: 10.3847/1538-4357/aabcbd

Scott, N., Brough, S., Croom, S. M., et al. 2017, MNRAS, 472, 2833, doi: 10.1093/mnras/stx2166

Sérsic, J. 1963, BAAA, 6, 41

Shapley, A. E. 2011, ARA&A, 49, 525, doi: 10.1146/annurev-astro-081710-102542

Shapley, A. E., Steidel, C. C., Adelberger, K. L., et al. 2001, ApJ, 562, 95, doi: 10.1086/323432

Sharma, S. 2017, ARA&A, 55, 213, doi: 10.1146/annurev-astro-082214-122339

Shivaei, I., Reddy, N. A., Steidel, C. C., & Shapley, A. E. 2015a, ApJ, 804, 149, doi: 10.1088/0004-637X/804/2/149

Shivaei, I., Reddy, N. A., Shapley, A. E., et al. 2015b, ApJ, 815, 98, doi: 10.1088/0004-637X/815/2/98

—. 2017, ApJ, 837, 157, doi: 10.3847/1538-4357/aa619c

Shivaei, I., Reddy, N. A., Siana, B., et al. 2018, ApJ, 855, 42, doi: 10.3847/1538-4357/aaad62

Shivaei, I., Reddy, N., Rieke, G., et al. 2020, ApJ, 899, 117, doi: 10.3847/1538-4357/aba35e

Skelton, R. E., Whitaker, K. E., Momcheva, I. G., et al. 2014, ApJS, 214, 24, doi: 10.1088/0067-0049/214/2/24

Steidel, C. C., Rudie, G. C., Strom, A. L., et al. 2014, ApJ, 795, 165, doi: 10.1088/0004-637X/795/2/165

Tacchella, S., Carollo, C. M., Förster Schreiber, N. M., et al. 2018, ApJ, 859, 56, doi: 10.3847/1538-4357/aabf8b

Tadaki, K.-i., Kodama, T., Tanaka, I., et al. 2014, ApJ, 780, 77, doi: 10.1088/0004-637X/780/1/77

Theios, R. L., Steidel, C. C., Strom, A. L., et al. 2019, ApJ, 871, 128, doi: 10.3847/1538-4357/aaf386

Tielens, A. G. G. M. 1998, ApJ, 499, 267, doi: 10.1086/305640

Toft, S., van Dokkum, P., Franx, M., et al. 2007, ApJ, 671, 285, doi: 10.1086/521810

Torrey, P., Snyder, G. F., Vogelsberger, M., et al. 2015, MNRAS, 447, 2753, doi: 10.1093/mnras/stu2592

Tremonti, C. A., Heckman, T. M., Kauffmann, G., et al. 2004, ApJ, 613, 898, doi: 10.1086/423264

Trujillo, I., Conselice, C. J., Bundy, K., et al. 2007, MNRAS, 382, 109, doi: 10.1111/j.1365-2966.2007.12388.x

van de Sande, J., Scott, N., Bland-Hawthorn, J., et al. 2018, Nature Astronomy, 2, 483, doi: 10.1038/s41550-018-0436-x

van den Bergh, S. 2002, PASP, 114, 797, doi: 10.1086/341708

van der Wel, A., Franx, M., van Dokkum, P. G., et al. 2014, ApJ, 788, 28, doi: 10.1088/0004-637X/788/1/28

Wang, X., Jones, T. A., Treu, T., et al. 2019, ApJ, 882, 94, doi: 10.3847/1538-4357/ab3861

Wild, V., Charlot, S., Brinchmann, J., et al. 2011, MNRAS, 417, 1760, doi: 10.1111/j.1365-2966.2011.19367.x

Worthey, G. 1994, ApJS, 95, 107, doi: 10.1086/192096

Wuyts, E., Rigby, J. R., Gladders, M. D., & Sharon, K. 2014, ApJ, 781, 61, doi: 10.1088/0004-637X/781/2/61

Wuyts, E., Wisnioski, E., Fossati, M., et al. 2016, ApJ, 827, 74, doi: 10.3847/0004-637X/827/1/74

Wuyts, S., Förster Schreiber, N. M., Genzel, R., et al. 2012, ApJ, 753, 114, doi: 10.1088/0004-637X/753/2/114

Wuyts, S., Förster Schreiber, N. M., Nelson, E. J., et al. 2013, ApJ, 779, 135, doi: 10.1088/0004-637X/779/2/135

Yoshikawa, T., Akiyama, M., Kajisawa, M., et al. 2010, ApJ, 718, 112, doi: 10.1088/0004-637X/718/1/112

Appendix A

The Wuyts et al. (2012) Method

In order to best constrain stellar mass estimates determined from the resolved SED fitting and constrain the shape of the resolved SEDs in the near-IR, we elect to include the unresolved *Spitzer*/IRAC photometry with the resolved photometry. Wuyts et al. (2012) presented a method for incorporating unresolved photometry into the results of resolved SED fitting by modifying the best-fit resolved SEDs such that their sum produces an SED that is optimally fit to the integrated photometry. We alternatively use a simple normalization based on the H_{160} flux to directly use the IRAC photometry in the resolved SED fitting (see Section 2.3.3 and Equation 2.3). In this appendix we compare the best-fit SEDs and SED-derived properties that result from the simple normalization we assumed versus the Wuyts et al. methodology. For this investigation we select GOODS-N 21507 ($z = 1.57$), AEGIS 8907 ($z = 1.59$), COSMOS 6750 ($z = 2.13$), and GOODS-N 17714 ($z = 2.23$), thus including two galaxies from our $z \sim 1.5$ and $z \sim 2.3$ redshift bins.

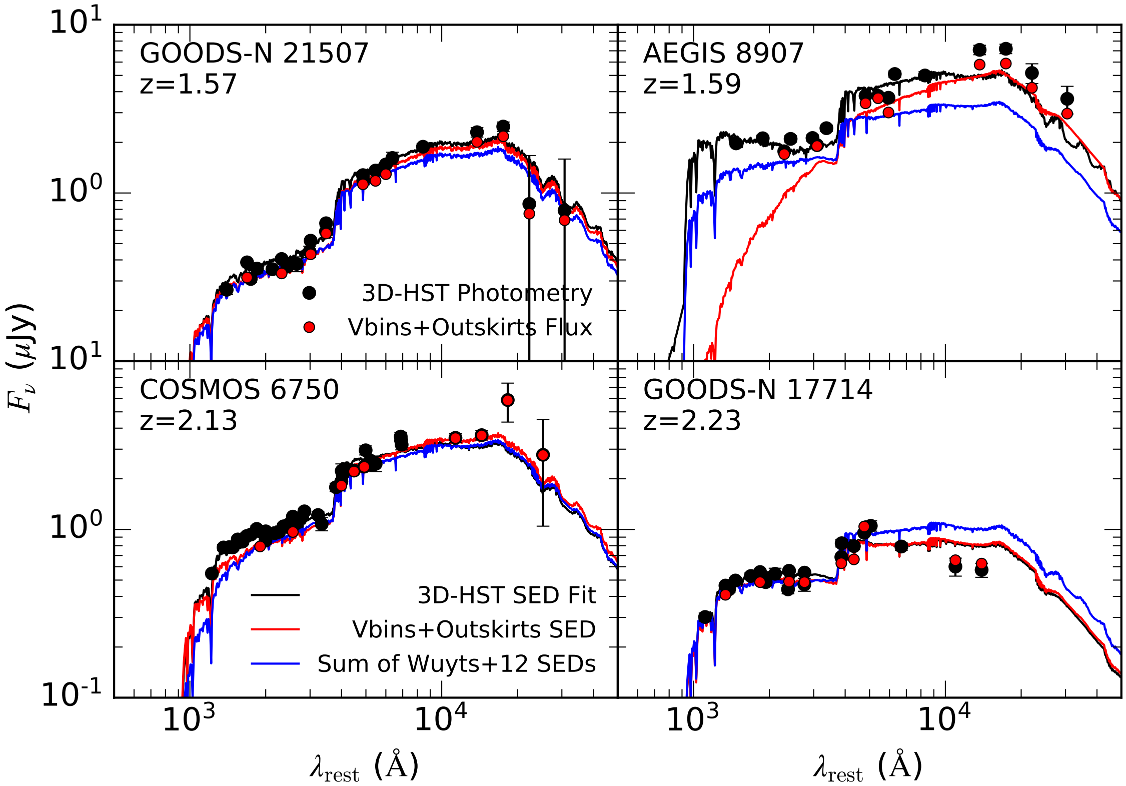

Figure A.1: Best-fit integrated SEDs from three different SED fitting methods for four example galaxies. The colors of the points and curves are the same as Figure 2.6. The black points and curves shows the fluxes from the 3D-HST photometry and the respective best-fit SED. The red points and curves indicate the total flux from all Voronoi bins (including outskirts) and the sum of their best-fit resolved SEDs for the IRAC data that has been normalized to the H_{160} flux (see Section 2.3.3 and Equation 2.3). The dark blue curves show the sum of the resolved SEDs that have alternatively been modified to include the IRAC photometry using the method described by Wuyts et al. (2012). The errors are typically smaller than the size of the points. Note that not all galaxies have outskirt components, such as GOODS-N 21507.

Here we briefly describe the method, but refer the reader to Wuyts et al. (2012) for a detailed description. First an initial fit is obtained for all resolved components using data from the resolved *HST* imaging by finding the model where the resolved chi-squared, $\chi_{\rm res}$, is minimized (see Section 2.3.4). The sum of the resolved SEDs is then compared to the integrated photometry—including the desired unresolved filters—by considering the integrated chi-squared defined by

$$\chi^2_{\rm res+int} = \chi^2_{\rm res} + \sum_{j=1}^{N_{\rm filt}} \frac{(F_j - \Sigma_{i=1}^{N_{\rm Vbin}} M_{i,j})^2}{\sigma_j^2}, \tag{A.1}$$

where F_j and σ_j are the integrated flux and flux errors in each j unresolved filter, respectively, and $M_{i,j}$ is the flux of the corresponding stellar population model in each i Voronoi bin and j unresolved filter for the $N_{\rm filt}$ unresolved filters to be included (in this case the *Spitzer*/IRAC photometry; see Equation 2 from Wuyts et al. 2012). The integrated chi-squared is iteratively improved by considering the next-best stellar population model in all resolved bins (worse resolved chi-squared) and selecting the bin that results in the largest change in the integrated chi-squared. This process is repeated up to 500 times or until there is no further improvement to be made in the integrated chi-squared.

In Figure A.1, we show the sum of the resolved SEDs from both our method (red curves) and the Wuyts et al. method (dark blue curves) compared to the SED that is fit to the unresolved 3D-HST photometry (black curves and points). The contribution from outskirt bins are included to best compare the summed SEDs with the SED that is fit to the unresolved 3D-HST photometry, but we note that a small normalization offset remains in some cases due to minor differences in the apertures (see the beginning of Section 2.4).[1]

[1]To correct for this offset, Wuyts et al. (2012) additionally normalized the integrated SED to the 3D-HST H_{160} flux. We do not include this additional normalization here since the purpose of this appendix is to

With the exception of AEGIS 8907, the integrated SEDs are consistent with each other. As discussed in Section 2.4.2, the UV slope of AEGIS 8907 is not well constrained due to there only being one resolved filter available at 1250–2500 Å. Therefore, our SED fitting procedure prioritizes fitting the data in the near-IR that is covered by the IRAC photometry, whereas the Wuyts et al. method emphasizes the shape of the optical photometry initially and later adjusts to best-match the integrated 3D-HST SED.

The resolved SEDs that are fit to the flux contained within each Voronoi bin are compared between our method and the Wuyts et al. method for AEGIS 8907 and GOODS-N 17714 in Figure A.2 and Figure A.3, respectively. We remind the reader that the SEDs from the Wuyts et al. method (dark blue curves) show the SEDs that have been adjusted to produce a better match to the integrated photometry, such that the stellar population model has changed and the individual resolved SEDs may not necessarily match the resolved UV and optical photometry. Figure A.2 and Figure A.3 shows that the resolved SEDs are most discrepant in outskirt bins (panels with red points and curves), whereas the resolved SEDs generally agree between the two methods for the well-constrained Voronoi bins (S/N $\geq$ 5 in at least 5 filters; panels with light blue points and curves). It is important to note that because the resolved stellar population models have changed in the Wuyts et al. method, the distribution of resolved properties may not be well-preserved—particularly in outskirt bins where the resolved SEDs are less constrained. However, in cases such as AEGIS 8907, the Wuyts et al. method better reproduces the overall shape of the integrated 3D-HST

compare our methodology with Wuyts et al. rather than reproduce the 3D-HST photometry. The change in normalization causes an insignificant change in the total SFR and stellar mass and does not affect the results presented here.

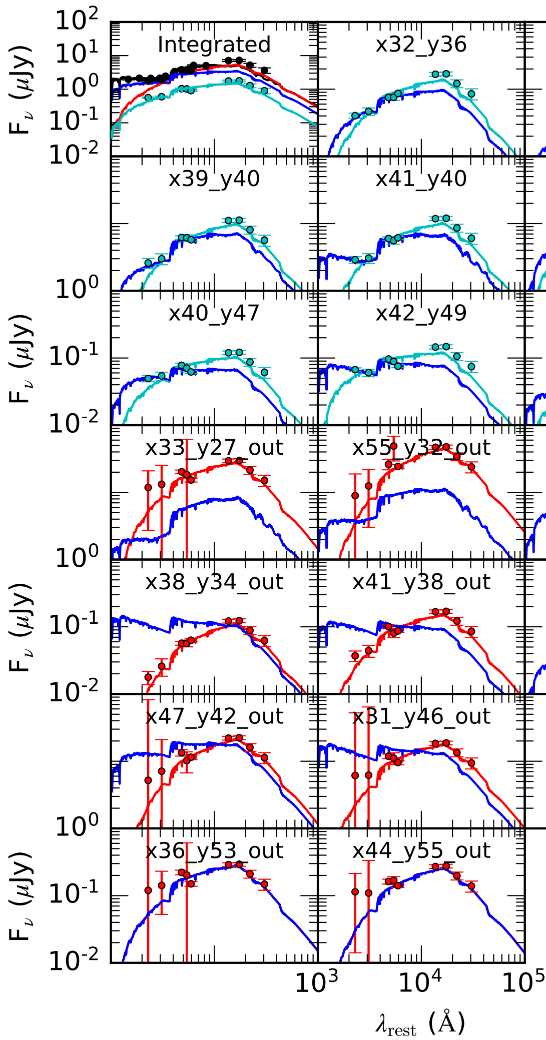

Figure A.2: The resolved SEDs for every Voronoi and outskirt bin comparing the two methods that incorporate the unresolved IRAC photometry for AEGIS 8907. The colors of the points and curves are the same as Figure 2.6 and Figure A.1. The first panel is the same as Figure 2.6, but also includes the light blue points and curves that show the sum of the flux and SEDs from the well-constrained Voronoi bins (S/N $\geq$ 5 in at least 5 filters). The panels with light blue points and curves show resolved SEDs fit to Voronoi bins and the panels with red points and curves show resolved SEDs fit to outskirt bins. The light blue and red SED curves directly include the IRAC photometry in the resolved SED fitting by normalizing the IRAC flux by the H_{160} resolved flux (see Equation 2.3). The dark blue curves show the resolved SEDs that have been modified to include the contribution of the IRAC photometry using the method described by Wuyts et al. (2012). Note that in some cases, particularly in the outskirt bins, there is no change between the original SED and the SED modified by the Wuyts et al. method, such that the SED curves overlap in the figure. The labels in each panel indicate the central pixel coordinate of each bin.

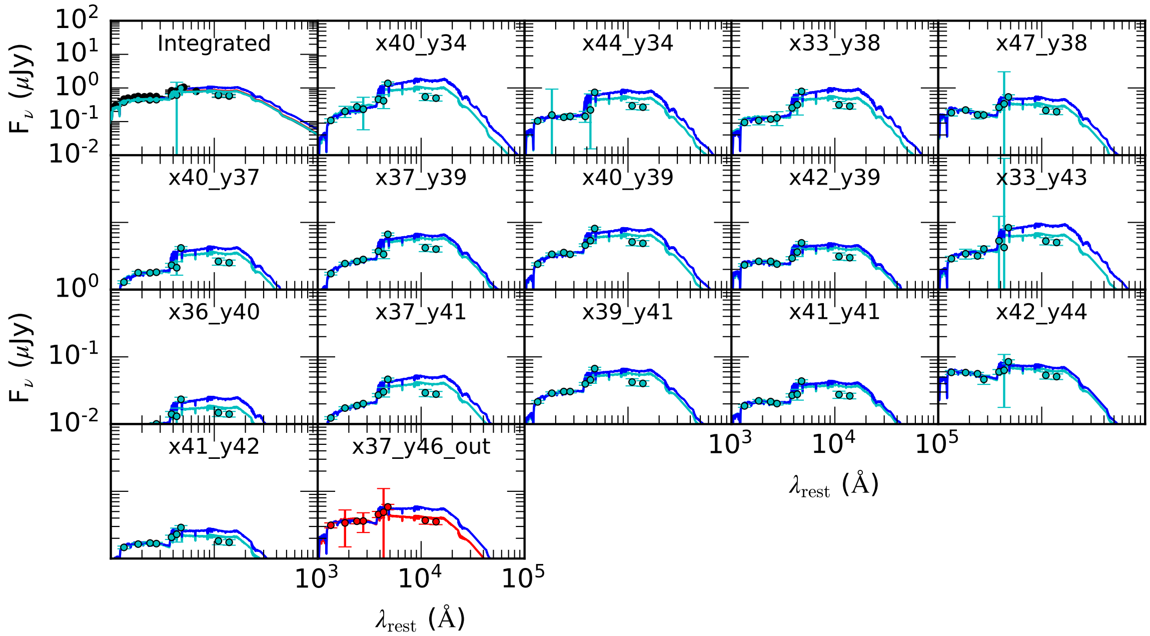

Figure A.3: The same as Figure A.2, except showing the resolved SEDs for every Voronoi and outskirt bin for GOODS-N 17714.

photometry since the UV slope is unconstrained by the resolved photometry for low-redshift objects using our methodology (see Section 2.4.2). In most cases though, the sum of all the resolved SEDs from both methods represent good fits to the unresolved photometry. Finally, the resolved stellar population and dust maps (including outskirts) are shown in Figure A.4 for AEGIS 8907 (top panels) and GOODS-N 17714 (bottom panels) from our method (left panels) and the Wuyts et al. method (right panels). We find that most cases are similar to GOODS-N 17714, where the resolved SED properties are comparable between the two methods. For cases like AEGIS 8907, the SFR and stellar mass distributions are also consistent between the two methods, with the greatest deviation being in the $E(B-V)_{\rm stars}$ distribution. As stated previously, the UV slope of AEGIS 8907 is not well-constrained by the resolved photometry alone, such that the discrepancy in the resolved $E(B-V)_{\rm stars}$ distribution is unsurprising.

In this work, we are interested in best preserving the distribution of the resolved stellar populations. Therefore, we elect to directly include the IRAC photometry in the resolved SED fitting by normalizing the IRAC photometry by the H_{160} flux contained in each resolved element (see Equation 2.3). In this appendix, we have shown that the results obtained through the Wuyts et al. method are comparable to those obtained through our methodology. However, the Wuyts et al. method may be more appropriate in situations where key SED features (e.g., UV slope, Balmer/4000 Å breaks) cannot be constrained by the resolved photometry, but at the cost of the specific distribution of stellar population properties being more uncertain. Throughout our analysis, we retain separation between our $z \sim 1.5$ and $z \sim 2.3$ samples due to the discrepancies in the inferred $E(B-V)_{\rm stars}$ caused by the UV slope being unconstrained by the resolved photometry.

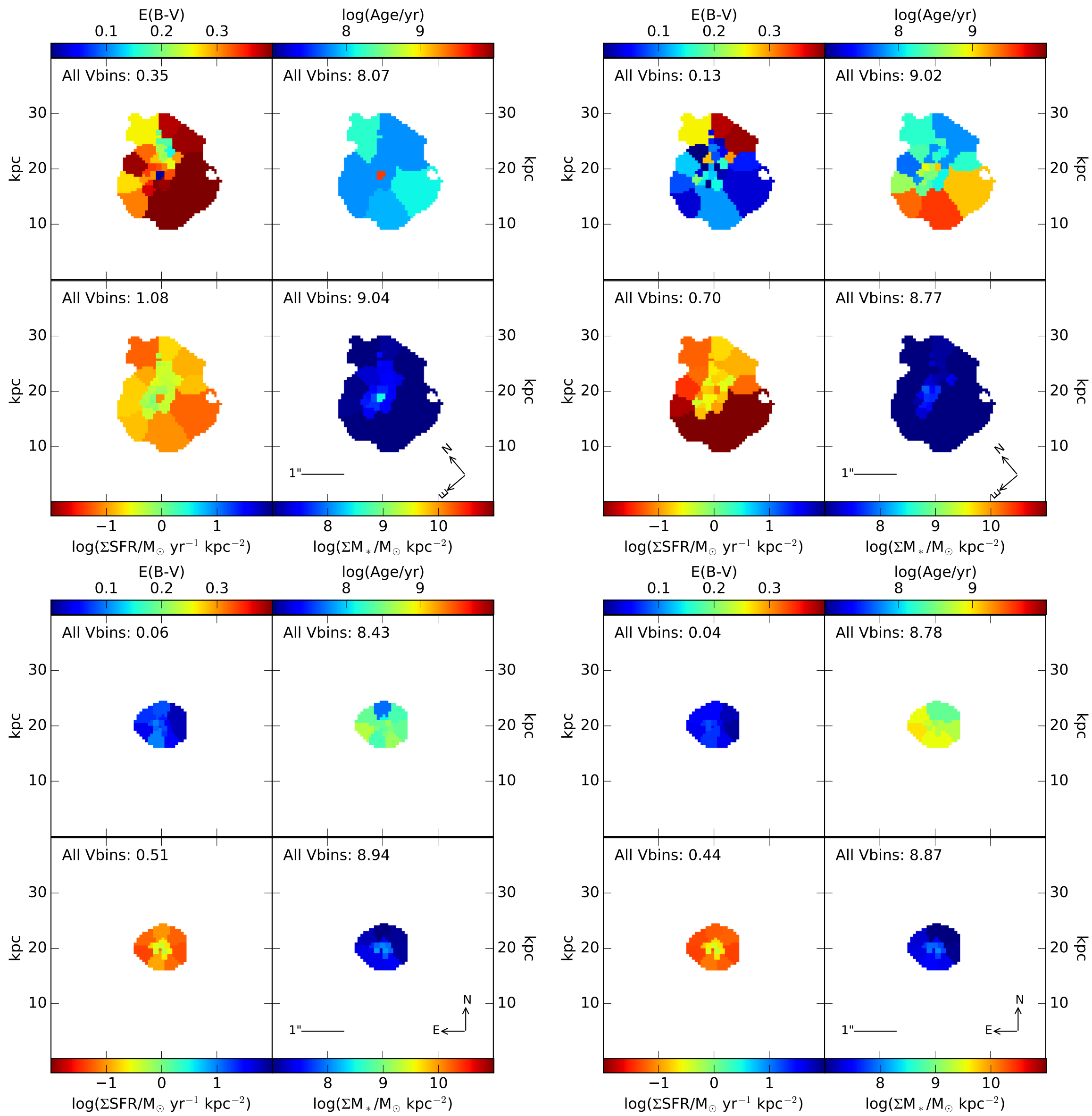

Figure A.4: Stellar population and reddening maps from the resolved SED fitting (including outskirt components) that incorporates IRAC photometry using a normalization based on the H_{160} flux (*left panels*) and the method described by Wuyts et al. (2012) (*right panels*). The distribution of $E(B-V)_{\rm stars}$ (*top left*), stellar population age (*top right*), SFR (*bottom left*), and stellar mass (*bottom right*) are shown for AEGIS 8907 ($z = 1.59$, *top panels*) and GOODS-N 17714 ($z = 2.23$, *bottom panels*). The listed number in each panel shows the average $E(B-V)_{\rm stars}$ or stellar population age weighted by the Voronoi bin areas or the summed SFR or stellar mass from all of the Voronoi bins.

Appendix B

H_{160}–IRAC Color Perturbations

In Section 2.3.3, we normalized the unresolved *Spitzer*/IRAC photometry by the H_{160} flux in each resolved element to accommodate for different area coverage. However, this unrealistically assumes that the IRAC flux directly traces the H_{160}-band flux. Most critically, this impacts galaxies at redshifts $z \gtrsim 2.5$, where the Balmer/4000 Å breaks shift into the H_{160} filter and the break strength becomes constrained exclusively by the IRAC photometry. As a probe of stellar population age, the strength of the Balmer/4000 Å breaks is crucial towards breaking the age-extinction degeneracy (e.g., Worthey 1994; Shapley et al. 2001), where the shape of the SED in the rest-frame UV to near-IR of a young, dusty stellar population looks similar to an old, dust-free population. In this appendix the H_{160}–IRAC colors are perturbed to simulate spatially resolved variations in the IRAC photometry to assess how constraining the H_{160}–IRAC colors influences the integrated and resolved stellar population properties, with special care towards the stellar population ages and reddening. For this investigation we select GOODS-S 36093, GOODS-N 20924, COSMOS 6750, and

UDS 22341, thus including two galaxies with redshifts above (2.62 and 2.55) and below (2.20 and 1.38) $z = 2.5$.

The H_{160}–IRAC colors are perturbed in all Voronoi bins simultaneously while maintaining a constant total flux. The H_{160}–IRAC color shift is calculated for each resolved element based on a normal distribution centered on the average of the four H_{160}–IRAC colors (where the IRAC flux is calculated by Equation 2.3) and a width of 1.0 mag. The proposed perturbations are restricted to be physically plausible values by requiring the H_{160}–IRAC perturbations to fall within the range of the H_{160}–IRAC colors in the Bruzual & Charlot (2003) stellar population synthesis model templates (constant SFH at the known redshift). The H_{160}–IRAC colors are perturbed for all but one Voronoi bin in the galaxy. If the sum of the perturbed IRAC fluxes is less than the original total IRAC flux, then the remaining Voronoi bin is attributed the leftover IRAC flux. Otherwise, if the sum of the perturbed IRAC fluxes add up to be greater than the original total IRAC flux, then all of the perturbations are repeated. The "leftover" bin often appears as an outlier in our results, but it does not alter the conclusions made here. An individual galaxy is perturbed n times, where n is the number of Voronoi bins in the galaxy, such that for each iteration a different Voronoi bin receives the leftover IRAC flux. In summary, for a given galaxy with n Voronoi bins, the entire resolved distribution is perturbed n times with every iteration having the same total flux. Finally, we use the perturbed IRAC fluxes to repeat the integrated and resolved SED modeling.

In Figure B.1, the SED-derived properties are compared between the original results with constant H_{160}–IRAC colors and the perturbed solutions. Regardless of redshift,

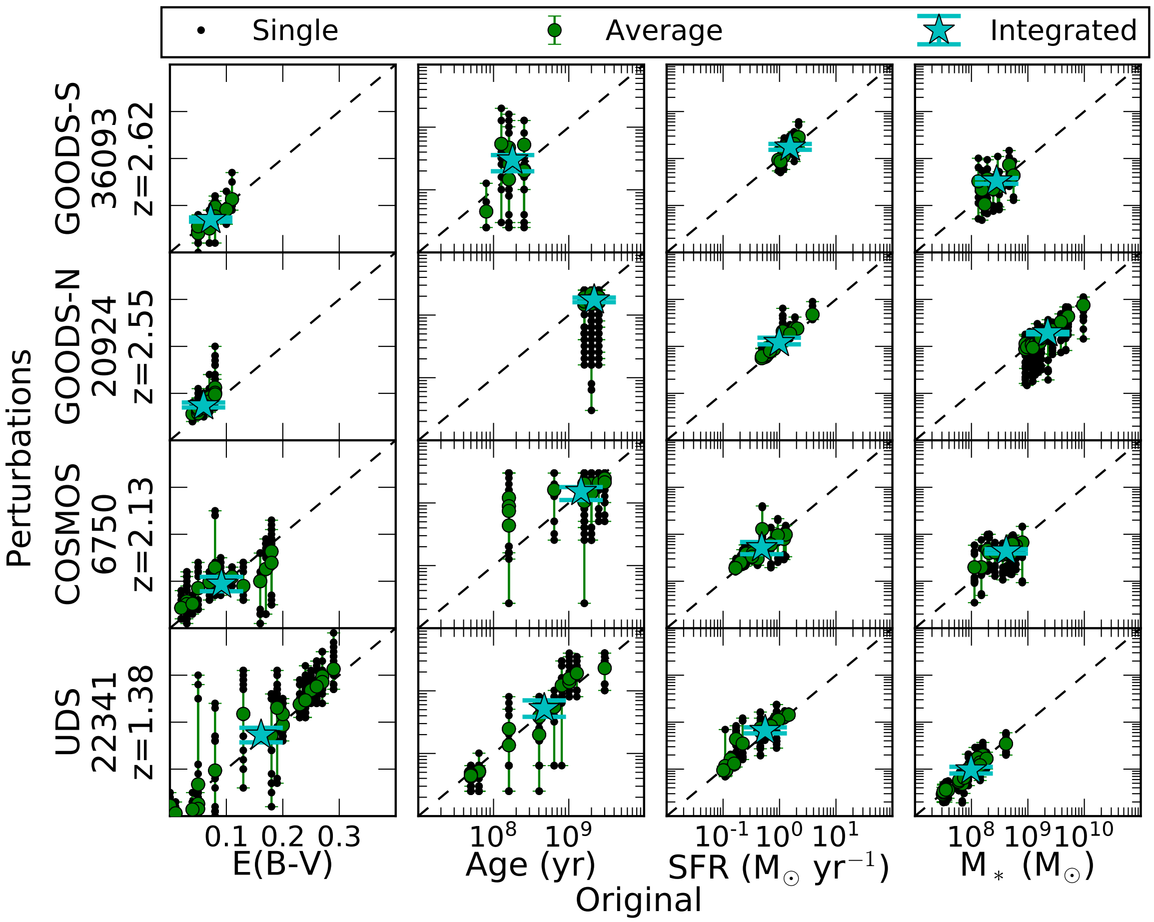

Figure B.1: The SED-derived $E(B-V)_{\rm stars}$, stellar population ages, SFRs, and stellar masses for each Voronoi bin as the H_{160}–IRAC colors are perturbed. Each row represents a single galaxy from our sample for a spread of redshifts. Each vertically connected green line represents a single Voronoi bin that has been perturbed n times, where n is the number of Voronoi bins in the galaxy. The black points along a single vertical line show how the SED-derived properties change as that single Voronoi bin is perturbed, compared to the original values. Each green circle is the average of the perturbed results within a single Voronoi bin, compared to the original value. The light blue stars compare the average of the Voronoi bins over n perturbations with the average of the original distribution (see Figure B.2). The errors of the blue stars show the spread in the averaged Voronoi bins over all n perturbations. The dashed black lines indicate where the perturbed properties equal the original properties.

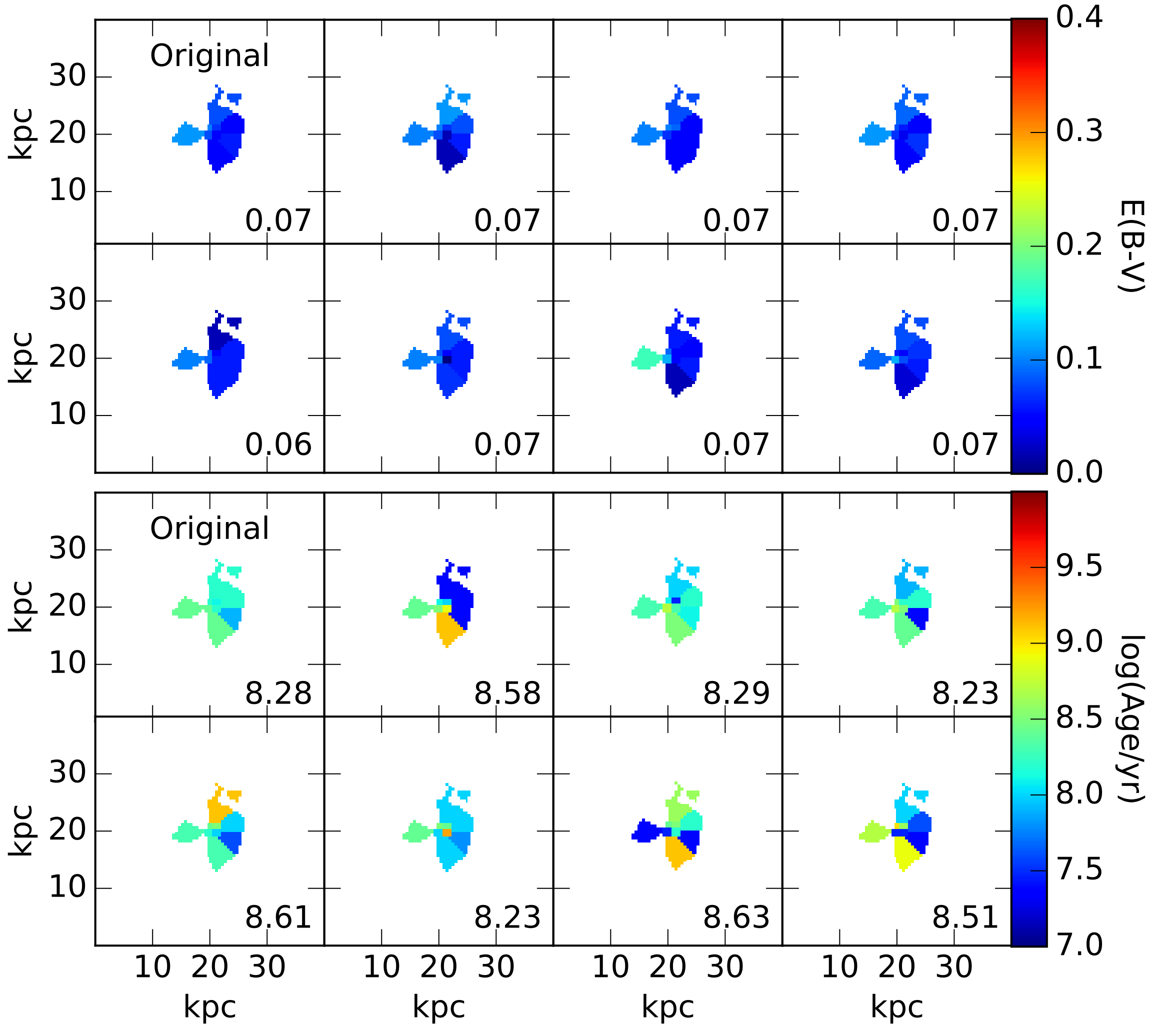

Figure B.2: $E(B-V)_{\rm stars}$ (*top*) and stellar population age (*bottom*) maps for GOODS-S 36093 ($z = 2.62$). The top left panels show the original $E(B-V)_{\rm stars}$ and stellar population age distribution from SED fitting, where the H_{160}–IRAC colors are constant across all Voronoi bins (see Equation 2.3). All other panels are show the $E(B-V)_{\rm stars}$ and stellar population age distributions when SED fitting was performed on the H_{160}–IRAC color perturbations. The value in the bottom right of each panel is the average $E(B-V)_{\rm stars}$ or log stellar population age (in dex) derived from the entire galaxy area.

we find that a perturbed Voronoi bin (black points) on average (green circles) has the same properties as the case of constant H_{160}–IRAC colors (x-axis values), and by extension maintains its intrinsic color. Figure B.2 shows an example (GOODS-S 36093, $z = 2.62$) of how the resolved reddening and stellar population ages changes with each perturbation of the H_{160}–IRAC colors, further demonstrating that the colors do not vary significantly from bin-to-bin. While the Voronoi bin that received the leftover IRAC flux is occasionally seen as an outlier, the average $E(B-V)_{\rm stars}$ or stellar population age (values in the bottom right corner of each panel in Figure B.2) remains consistent. In general, the average of the resolved distribution for all SED-derived properties is comparable with the average of the original distribution (light blue stars in Figure B.1). Therefore, we conclude that we are not unduly constraining the resolved stellar ages or reddening by simplifying the IRAC flux distribution through our use of Equation 2.3.

Appendix C

Analysis of the Patchiness Metric

In Section 4.3.1, we derived a morphology measure that is sensitive to both faint and bright regions within galaxies using Equation 4.2. In this appendix, an in-depth analysis of the patchiness metric is presented using the patchiness, P, calculated from the resolved $E(B-V)_{\mathrm{stars}}$, stellar population age, SFR, and stellar mass maps. This analysis of the patchiness metric includes: observed correlations between the calculated P of all resolved SED-derived properties, the potential dependence of P on the number of resolved elements, a comparison between P and the ICD (Papovich et al. 2003), P calculated from the pixel-to-pixel distribution, and the behavior of P when galaxies are artificially redshifted.

First, the calculated P on the resolved SED-derived $E(B-V)_{\mathrm{stars}}$, stellar population ages, SFRs, and stellar masses are directly compared in Figure C.1. If a given galaxy exhibits a patchy distribution in any SED-derived property, it is likely to exhibit a patchy distribution in the other resolved stellar population properties. Most significantly, galaxies with patchier SFRs tend to have patchier stellar masses and galaxies with patchier

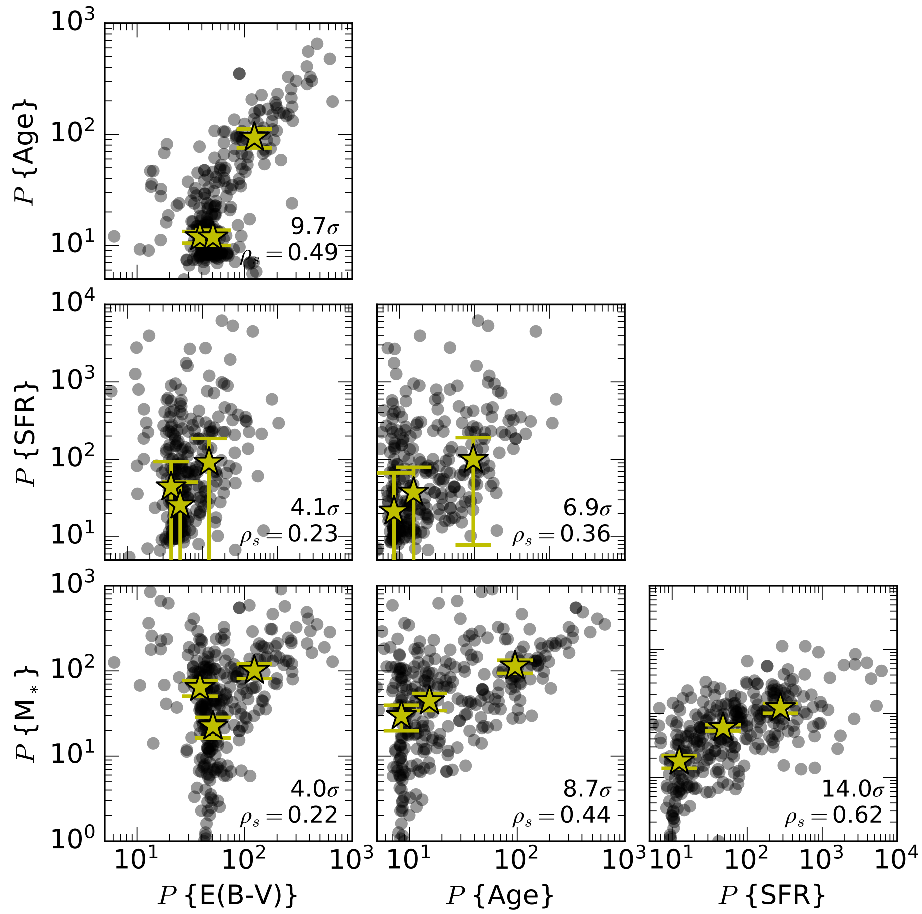

Figure C.1: Relationships between P calculated from the resolved SED-derived $E(B-V)_{\rm stars}$, stellar population ages, SFRs, and stellar masses. The yellow stars show the median P values in three equally sized bins that are based on the P measurement of the x-axis. The Spearman rank correlation coefficient and its significance is listed in the bottom right corner of each panel.

$E(B-V)_{\rm stars}$ distributions tend to have patchier stellar ages. While the relationship between the P of the resolved SFRs are stellar masses could provide clues as to how galaxies build their stellar mass in the context of the resolved SFR–M_* relationship, the significance of this relationship could alternatively be degenerate in that the resolved SFRs and stellar masses are both being derived from the normalization of the resolved SEDs. Similarly, the relationship between patchy reddening and stellar ages could be related to the age–extinction degeneracy (e.g., Worthey 1994; Shapley et al. 2001), where the SED of an old, dust-free stellar population has a similar shape compared to the SED of a young, dusty stellar population.

The relationship between P and the number of Voronoi bins in the galaxy is shown in the left panels of Figure C.2 to investigate a possible bias between how P is calculated in Equation 4.2 and the resolution of individual galaxies. The number of Voronoi bins ranges from 5–81 for all 310 galaxies in the sample, but a majority of galaxies have 7–30 Voronoi bins (206 galaxies, highlighted by the green shaded regions). While galaxies with more Voronoi bins tend to have higher P measured from the resolved stellar ages, SFRs, and stellar masses, galaxies with many or few Voronoi bins can exhibit either high or low P measurements for all resolved stellar population properties. Therefore, we suggest that the relationship between the number of resolved elements and calculated P is physically driven, especially considering that Voronoi bins are defined by grouping regions of similar brightness (Cappellari & Copin 2003). Furthermore, low S/N components that could bias the P calculation are not included in the analysis (see Section 4.2.4).

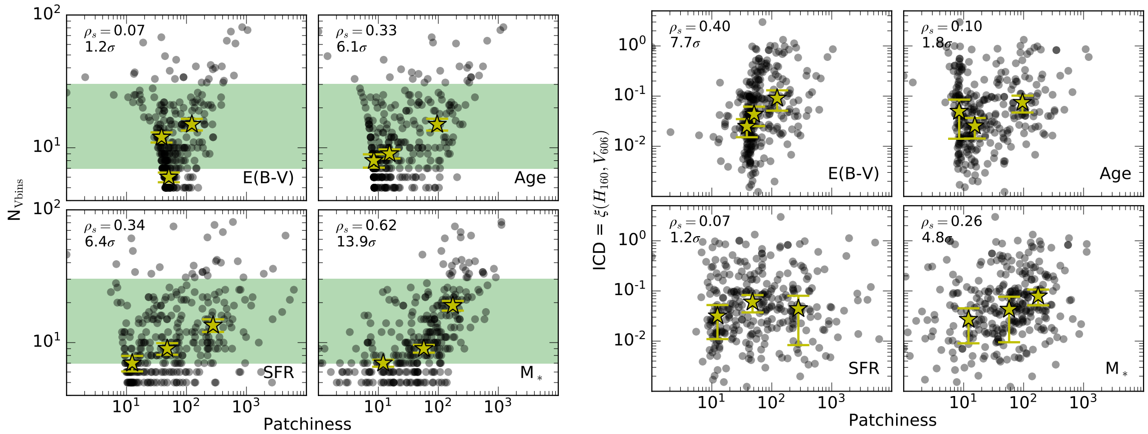

Figure C.2: *Left:* The number of Voronoi bins versus the P measured from the resolved $E(B-V)_{\rm stars}$, stellar population ages, SFRs, and stellar masses. The shaded regions highlight galaxies with 7–30 Voronoi bins, which includes a majority of the sample (206 galaxies). The yellow stars show the median number of Voronoi bins and P values in three equally sized bins that are based on the P measurement of the x-axis. The Spearman rank correlation coefficient and its significance is listed in the top left corner of each panel. *Right:* The ICD (Papovich et al. 2003) measured from the H_{160} and V_{606} resolved imaging versus the P measured from the resolved stellar population and reddening maps. The yellow stars show the median ICD and P values in three equally sized bins that are based on the P measurement of the x-axis.

Of the pre-existing morphology metrics, patchiness is most closely related to the ICD (Papovich et al. 2003). The ICD measures the dispersion of light between two filters of the resolved imaging and, thus, is sensitive to general deviations in the flux rather than the brightest regions alone. The primary advantage of patchiness compared to the ICD is that is can be generally applied to any resolved property, whereas the ICD is limited to the flux distribution of two resolved images. Therefore, P calculated on the resolved stellar population and reddening maps incorporates the information from at least 5 resolved filters (see Section 4.2.4). The ICD measured from the H_{160} and V_{606} imaging is compared to the P calculated from the resolved stellar population properties in the right panels of Figure C.2. The ICD is most significantly correlated with the P of the $E(B-V)_{\rm stars}$ distribution, which is not entirely surprising given that the dispersion between the rest-frame optical (H_{160}) and UV (V_{606}) light is an equivalent interpretation of the P measured from the $E(B-V)_{\rm stars}$ distribution.

To examine the behavior of the patchiness metric on other resolved scales, patchiness is calculated on the pixel-to-pixel scale for a subset of 50 galaxies that have stellar population parameters that are representative of the larger sample. In the pixel-to-pixel patchiness calculation, all pixels identified by the 3D-HST segmentation map are included. The left panels of Figure C.3 show how P measured on the pixel-to-pixel distribution compares to P measured on the Voronoi bin distribution. The relative P calculated on the $E(B-V)_{\rm stars}$ distribution is generally preserved between a pixel and Voronoi bin scale and marginally preserved for P calculated on the stellar mass distribution. However, measuring P on a pixel-to-pixel scale is not recommended due to correlated signal between neighboring pixels and low S/N pixels that cause unphysical outliers in the resolved distribution that would artificially drive P to higher values. Therefore, we strongly discourage the use of the patchiness parameter on pixel-to-pixel scales, recommend a minimum bin size that is at least the width of the instrument PSF, and that low S/N components that can cause unreliable resolved measurements are removed from the analysis (also see Fetherolf et al. 2020a, in press; Chapter 2).

Finally, the effect of redshift on the patchiness metric is explored by artificially redshifting all galaxies in the $z \sim 1.5$ sample (126 galaxies) to a redshift that is randomly selected from a Gaussian distribution with the mean and standard deviation of the $z \sim 2.3$ sample ($z = 2.30 \pm 0.14$). For simplicity, the change in pixel scale between these redshifts

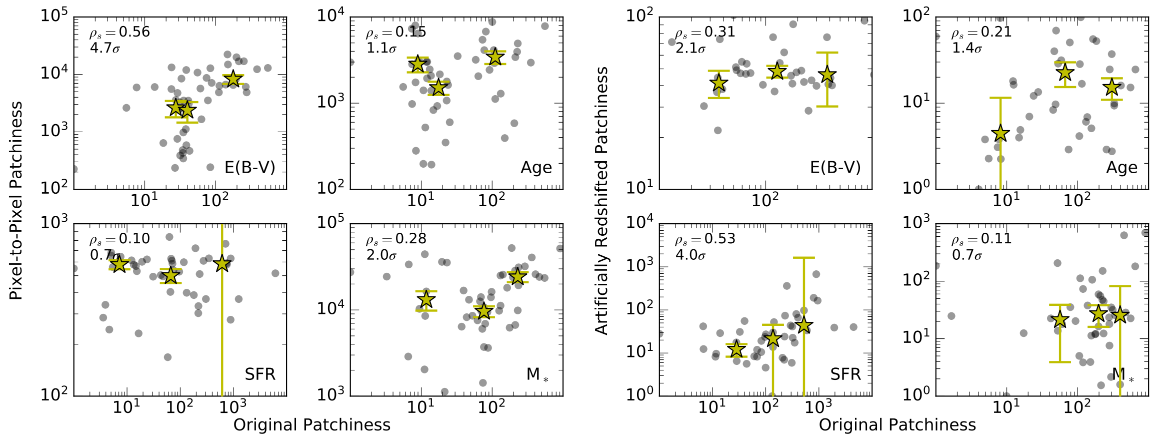

Figure C.3: *Left:* The P calculated from the pixel-to-pixel $E(B-V)_{\rm stars}$, stellar population age, SFR, and stellar mass distributions compared to the P calculated from the Voronoi bin stellar population properties for a subset of 50 galaxies in the sample. The yellow stars show the median P values in three equally sized bins that are based on the P measurement of the x-axis. The Spearman rank correlation coefficient and its significance is listed in the top left corner of each panel. *Right:* The P calculated from stellar population and reddening maps for a subset of 43 galaxies that have been artificially redshifted from $z \sim 1.5$ to $z \sim 2.3$ compared to their original P values.

is considered negligible and no correction is applied for the shift in the bandpass due to the large widths of the *HST* resolved filters. Cosmological dimming is applied by multiplying the observed flux in each filter by the square of the ratio of luminosity distances at the two redshifts (Barden et al. 2008), then the Voronoi binning and resolved SED fitting procedures are repeated using the new flux distributions. The artificially redshifted sample is restricted to galaxies with at least 5 Voronoi bins that have a S/N $\geq$ 5 in at least 5 filters (see Section 4.2.4), resulting in a subsample of 43 galaxies that have been artificially redshifted to $z \sim 2.3$. The P measured from the artificially redshifted stellar population and reddening maps is compared to the original P measurements in the right panels of Figure C.3. Except in the case of the resolved SFRs, P is generally not consistent when the effects of cosmological redshift are considered. Furthermore, this does not include the intrinsic differences in the physical properties of galaxies between redshifts $z \sim 1.5$ and $z \sim 2.3$ (e.g., see recent reviews by Shapley 2011; Madau & Dickinson 2014). Therefore, we recommend separately analyzing the morphologies of galaxies at different redshifts. This assessment is also in agreement with our recommendation in Section 4.3.1 to use uniformly defined samples to relatively compare the P of resolved distributions.

The most important conclusions from this in-depth analysis on the patchiness metric are summarized as follows: P is not biased towards the number of resolved elements for a given galaxy, calculating P on the pixel-to-pixel distribution is not recommended due to potential bias by low S/N outliers, and the P (and other morphology metrics) of galaxies at different redshifts should be analyzed separately. These conclusions align with our recommendation to relatively compare the P of resolved distributions for galaxies within uniformly defined samples. The resolved distributions for the sample of galaxies used throughout this paper are uniformly defined by separating the $z \sim 1.5$ and $z \sim 2.3$ samples and applying a strict criteria for including resolved elements in the analysis (see Section 4.2.4). The findings in this appendix also briefly highlight how the patchiness metric can be used on other resolved stellar population properties (besides $E(B-V)_{\rm stars}$, which is highlighted in this work) to further investigate how galaxies build their stellar mass, such as through the resolved SFR–M_* relationship, which we defer to future work.